DOT/FAA/AR-10/23,P1

Air Traffic Organization
NextGen & Operations Planning
Office of Research and
Technology Development
Washington, DC 20591

Explicit Finite Element Modeling of Multilayer Composite Fabric for Gas Turbine Engine Containment Systems, Phase III

Part 1: Arizona State University Material Model and Numerical Simulations

January 2011

Final Report

This document is available to the U.S. public through the National Technical Information Services (NTIS), Springfield, Virginia 22161.

This document is also available from the Federal Aviation Administration William J. Hughes Technical Center at actlibrary.tc.faa.gov.

U.S. Department of Transportation
Federal Aviation Administration

NOTICE

Technical Report Documentation Page

1. Report No.	2. Government Accession No.	3. Recipient's Catalog No.
DOT/FAA/AR-10/23,P1		

4. Title and Subtitle	5. Report Date
EXPLICIT FINITE ELEMENT MODELING OF MULTILAYER COMPOSITE FABRIC FOR GAS TURBINE ENGINE CONTAINMENT SYSTEMS, PHASE III, PART 1: ARIZONA STATE UNIVERSITY MATERIAL MODEL AND NUMERICAL SIMULATIONS	January 2011
	6. Performing Organization Code

7. Author(s)	8. Performing Organization Report No.
S. D. Rajan, B. Mobasher, Z. Stahlecker, S. Bansal, D. Zhu, M. Morea, and K. Dhandapani	

9. Performing Organization Name and Address	10. Work Unit No. (TRAIS)
Department of Civil & Environmental Engineering Arizona State University Tempe, AZ 85287-5306	11. Contract or Grant No.

12. Sponsoring Agency Name and Address	13. Type of Report and Period Covered
U.S. Department of Transportation Federal Aviation Administration Air Traffic Organization NextGen & Operations Planning Office of Research and Technology Development Washington, DC 20591	Final Report
	14. Sponsoring Agency Code ANE-110

15. Supplementary Notes

The Federal Aviation Administration Airport and Aircraft Safety R&D Division Technical Monitor was Donald Altobelli.

16. Abstract

Under a Federal Aviation Administration Grant, sponsored by the Aircraft Catastrophic Failure Prevention Program, a research team consisting of members from Arizona State University (ASU), National Aeronautics and Space Administration Glenn Research Center (NASA-GRC), and SRI International collaborated to continue the development of test procedures and computational models for designing and evaluating fabric turbine engine containment structures. This report contains the details of the development and improvements made to the ASU constitutive model for Kevlar® and validation of the material model with numerical simulation of NASA-GRC ballistic impact tests. The developed constitutive model is verified in a number of different ways—single-element tests, quality assurance tests, sensitivity analysis, and comparison against ballistic tests. Both single- and multilayer finite element models for the ballistic tests are discussed. Finally, a micromechanical model was developed to study the behavior of Kevlar fabric swaths modeled using the actual swath geometry involving fill and warp yarn.

17. Key Words	18. Distribution Statement
Kevlar, Simulation, Engine containment, LS-DYNA, Impact, Fabric	This document is available to the U.S. public through the National Technical Information Service (NTIS), Springfield, Virginia 22161. This document is also available from the Federal Aviation Administration William J. Hughes Technical Center at actlibrary.tc.faa.gov.

19. Security Classif. (of this report)	20. Security Classif. (of this page)	21. No. of Pages	22. Price
Unclassified	Unclassified	117	

ACKNOWLEDGEMENTS

The authors wish to thank Mr. William Emmerling, Mr. Donald Altobelli, and Mr. Chip Queitzsch of the Federal Aviation Administration for their technical and financial support. To meet the objectives of this project, the authors have relied on technical collaborations with several other organizations that include Honeywell Engines & Systems (Phoenix), SRI International, and National Aeronautics and Space Administration Glenn Research Center (NASA-GRC). Some of the individuals who contributed to this project include Dr. Jeff Simons of SRI International and Dr. J. M. Pereira of NASA-GRC. Their support and cooperation in meeting the research objectives is greatly appreciated.

TABLE OF CONTENTS

LIST OF FIGURES

LIST OF TABLES

LIST OF ACRONYMS

2D	Two-dimensional
3D	Three-dimensional
ASU	Arizona State University
CLT	Classical lamination theory
D	Denier
FAA	Federal Aviation Administration
FBO	Fan blade-out
FD	Coefficient of dynamic friction
FE	Finite element
FS	Coefficient of static friction
G.L.	Gage length
MOC	Method of cells
NASA-GRC	National Aeronautics and Space Administration Glenn Research Center
QA	Quality assurance
RVE	Representative volume element
SEM	Scanning-electron microscopy
SHB	Split Hopkinson bar
SRI	SRI International
UMAT	User-defined material definition

EXECUTIVE SUMMARY

A team consisting of Arizona State University (ASU), National Aeronautics and Space Administration Glenn Research Center (NASA-GRC), and SRI International (SRI) collaborated to continue development of computational models and verification tests for designing and evaluating turbine engine fan blade fabric containment structures. This phase of the research (Phase III) was conducted under a Federal Aviation Administration (FAA) Grant and was sponsored by the Aircraft Catastrophic Failure Prevention Program. The research was directed toward improving the modeling of a turbine engine fabric containment structure for an engine blade-out containment demonstration test required for certification of aircraft engines.

The first two phases of research yielded both modeling and experimental data that characterized the behavior of fabric materials for engine containment systems. The current study (Phase III) captures the details of the analytical and testing work done in the third phase of the on-going FAA-sponsored research. Parts 1 and 2 of this report document research conducted through 2009. When Parts 3 and 4 are published, they will supplement Parts 1 and 2 with the results of ongoing work. The following tasks and objectives correspond to this four-part report:

- Part 1—ASU Material Model and Numerical Simulations. Part 1 uses the knowledge and experimental data from the previous two phases and recent additional tests to develop a new constitutive model suitable for implementing in an explicit finite element (FE) analysis. This includes relating the changes in stress to the changes in strain, and identifying and quantifying the modes of failure.

- Part 2—Fabric Material Tests. An improved macro model can result from a better understanding of the fabric behavior. The Part 2 studies include understanding the geometry and behavior of individual yarns both under quasi-static and high strain rate effects, and the yarn-on-yarn interaction.

- Part 3—Improvements in ASU Material Model and Numerical Simulations. Part 3 will include improvements to the ASU material model based on additional testing and analysis.

- Part 4—Additional Fabric Material Tests. Part 4 will documents additional material tests conducted at ASU that were used to improve the ASU material model.

This report documents Part 1 of 4, the development and evolution of an ASU material model for Kevlar® fabric. The developed constitutive model is verified in a number of different ways—single-element tests, quality assurance tests, sensitivity analysis, and comparison against ballistic tests. Both single- and multilayer FE models for the ballistic tests are discussed. Finally, a micromechanical model was developed to study the behavior of Kevlar fabric swaths modeled using the actual swath geometry involving fill and warp yarns.

1. INTRODUCTION.

1.1 PURPOSE.

This research study captures the details of the analytical work done in the third phase of the on-going Federal Aviation Administration (FAA)-sponsored research on building a more sophisticated engine containment system model. The purpose of this research was to develop a robust finite element (FE) analysis modeling methodology for a turbine engine fabric containment system that benefits the design and certification for commercial aircraft engines.

In this report, the development and evolution of the Arizona State University (ASU) material models for Kevlar® fabric are discussed. The developed constitutive model is verified in a number of different ways—single-element tests, quality assurance tests, sensitivity analysis, and comparison against ballistic tests. Both single- and multilayer FE models for the ballistic tests are discussed. Finally, a micromechanical model was developed to study the behavior of Kevlar fabric swaths modeled using the actual swath geometry involving fill and warp yarns.

1.2 BACKGROUND.

Fiber fabric wraps are widely used in the containment systems of aircraft gas turbine engines. Such systems are found to be especially cost-effective and light weight for mitigating engine debris during a fan blade-out event. This is mostly because fabrics have a high strength per unit weight. Moreover, it is inexpensive to manufacture such a containment system compared to traditional metallic systems. To properly utilize this advantage, it is necessary to have a robust FE analysis modeling methodology for daily design tasks. Modeling a multilayer fabric for engine containment systems during a fan blade-out event has been a difficult task. Under Grants from the FAA Aircraft Catastrophic Prevention Program, ASU has been conducting research in this area for several years. The first two phases of this research have yielded both experimental and modeling techniques, and data characterizing the behavior of fabric materials for engine containment systems.

In the first phase of this research work (September 2001-August 2003) progress was made in addressing engine containment modeling issues. The combined efforts of Honeywell Engines & Systems, SRI International (SRI), National Aeronautics and Space Administration Glenn Research Center (NASA-GRC), and ASU resulted in the following major accomplishments:

- Experimental Characterization of Fabrics: A fabric material model originally developed by SRI through FAA sponsorship for Kevlar and Zylon® fabrics was improved during this phase. Independent laboratory tests conducted at ASU and SRI form the basis of this model. These material models are general enough to be used as the constitutive model for both static and dynamic/explicit FE analyses.

- Static Ring Tests: Static tests of containment wraps subjected to loads through a blunt nose impactor were performed at ASU. Ballistic tests of containment wraps subjected to a high-velocity projectile were performed at NASA-GRC. These tests provided test cases (benchmark results) to validate the developed FE methodology.

- FE Material Model Development: The material models were used by the research team in the FE simulation of static and ballistic tests. The static test results have been validated by ASU using the ABAQUS FE program. The ballistic test results were validated by Honeywell and SRI using the LS-DYNA FE program.

- Engine Fan Blade-Out (FBO) Simulation: The knowledge gained from previous tasks was used by Honeywell for the numerical simulation of engine FBO events involving existing production engine models and compared against test results (employing Kevlar containment).

- Kevlar-Zylon Comparison: An understanding was reached of the relative comparison between Kevlar and Zylon materials in turbine engine FBO containment systems.

The second phase of research (September 2003-July 2006) brought a new level of capability to design and develop fan containment systems for turbine engines, thereby leading to more economical and safer containment system designs as follows.

- Robust FE Model Development: Improvements were made to the SRI material models for 1420 Denier (D) Kevlar 49 (17x17 weave) and 500 D Zylon AS (35x35 weave), thereby increasing confidence that these models and methodologies could accurately predict design conditions.

- Improved FE Modeling Capability for Multiple Layers of Fabric: In Phase I, most of the LS-DYNA models used a single element through the thickness to model the multiple-layer fabric, which ranged from 1 to 24 layers. Although this technique is simple, it does not provide the predictive capability of computing the number of fabric layers that will be penetrated during a containment event. Therefore, the containment margin in terms of the number of unpenetrated layers versus total number of layers cannot be accurately predicted. Multilayer models (multiple layers of modeled fabric using multiple layers of shell elements) were developed to give a better understanding of fabrics used in containment systems. In most of this work, a single-shell element represented four layers of fabric, which made the model size, fabric layer resolution, and interaction between layers reasonable while being reliable to run.

- 1500 D Zylon Material Characterization: In the previous phases, limited ballistic and static tests of 1500 D Zylon (17x17 weave) indicated that 1500 D Zylon has the potential to offer a 60% weight advantage over Kevlar for the same fragment energy. 1500 D Zylon, it would seem, enables either a dramatic increase in the fan containment safety margin, or a decrease in engine weight, or a combination of both. The objective of this task was to conduct further tests to develop and validate a material model for 1500 D Zylon. It should be noted that during this research, it was discovered that Zylon was found to have excessive deterioration due to heat and humidity. As a result, it was decided that the remainder of this research would focus only on Kevlar fabrics.

- Engine Simulations: As in the Phase I research, FE simulations were performed to validate improvements to the material models and methods developed under this program

as they relate to propulsion engine fan blade containment. Fabric material models and modeling methods and improvements to the material models and methods were validated using fan containment test data.

In this Phase III, Part 1 report, the details of the development of the ASU constitutive model are presented in section 2.2. The material model is referred to as ASU User-Defined Material Version 1.0 (ASUumatV1.0). In section 2.4, the improvements to the constitutive model are presented. This improved model is referred to as ASU User-Defined Material Version 1.1 (ASUumatV1.1).

2. THE ASU MATERIAL MODEL DEVELOPMENT.

2.1 OVERVIEW.

Fiber fabrics are widely used in the containment systems of aircraft gas turbine engines. Such systems are found to be especially cost-effective for mitigating engine debris during an FBO event. This is mostly because fabrics have a high strength-per-unit weight. Moreover, it is inexpensive to manufacture such a containment system compared with the traditional metallic systems.

Much research has been done with regard to developing predictive material models for the behavior of woven fabrics when subjected to structural loads. Most of this work, however, has focused around the behavior of woven fabrics when combined with some form of epoxy matrix. Less research has been conducted for woven fabrics when acting as the main structural component, such as in fan containment systems. Section 2.2 presents the development of a material model that can be applied to woven fabric noncomposites such as Kevlar.

2.2 CONSTITUTIVE MODELING.

2.2.1 Literature Review of Current Fabric Modeling Procedures.

Creating FE models of dry fabrics that include yarn geometry details at a mesoscale level for use in the analysis of ballistic events is not practical—the FE model would be too large and detailed. A more useful approach is to create an equivalent continuum model at a macroscale level. Extensive work has already been done with the interest of determining the effective material properties of fabric composites and fabrics. Some of the effective material properties include material constants, such as modulus of elasticity and shear modulus. The main techniques that have been successfully employed are analytical methods, including the method of cells (MOC) [1], classical lamination theory (CLT) [2], and numerical methods using FE modeling with virtual testing [3]. There has been recent success in the development of nonlinear material models for simulating simple structural events, such as uniaxial tension tests, and for simulating complex structural events, such as those involving ballistic impacts [4]. For both cases, the majority of the material models were developed for use with FE solutions. However, some models were developed for use with finite difference solutions as well [5]. Research has also been done in the area of strain rate effects on fabric composites and fabrics [6 and 7]. Since most of these materials are used in areas where ballistic events occur, an accurate prediction of strain rate effects is considered necessary.

2.2.1.1 Techniques for Determining Effective Material Properties.

Creating FE models of dry fabrics that include yarn geometry details (mesoscale) for use in the analysis of ballistic events is believed to be very computationally expensive. A more practical approach is to create an equivalent continuum model (macroscale). Determining the effective or macromechanical properties of a woven fabric can be a challenging task. Experimental tests can be conducted to ascertain some or all of the effective material properties. However, this approach is expensive since new tests must be conducted if the effective properties are needed for different weaves and weave geometries. Small changes in the fabric architecture alter the fabric's behavior, and a model that can simulate the effect of these changes is a valuable tool. The difficulty in developing a model to simulate the effective properties lies in (1) accurately determining the yarn geometry in the fabric and (2) simulating the yarn-yarn interaction and the yarn-matrix interaction (for composites). More recently, very accurate descriptions of the yarn geometry have been made through the use of photomicrographs or scanning electron microscopy (SEM) images [8]. In the absence of these high-resolution images, researchers have made reasonable assumptions for the fabric geometry. Currently, there are several approaches being used to compute the effective properties—the MOC, variations of the MOC, FE modeling with virtual testing, and CLT. With each method, only a representative unit of material is considered due to the repetitive pattern in the as-built material structure. The terms "representative unit cell," "unit cell," or "representative volume element (RVE)" will be used interchangeably in this report. An example of a repetitive unit cell for a plain weave fabric [1] is shown in figure 1. Symmetric conditions are used to improve the computational efficiency—one-quarter of the unit cell model is shown in figure 1(c).

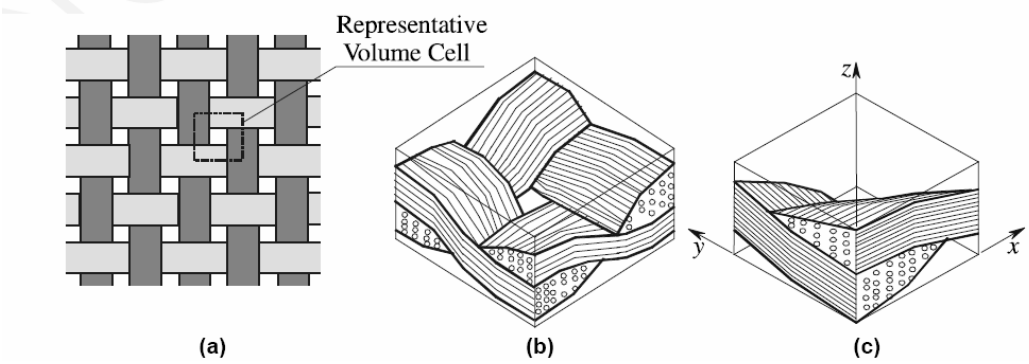

Figure 1. Weave Architecture Showing (a) the Representative Volume Cell, (b) the RVE, and (c) Quarter of the RVE Section

Analytical methods, including CLT and MOC, have been successful in determining effective material properties. Some of the earliest CLT models that have been used to determine the elastic modulus of woven fabric composites include those by Ishikawa and Chou [9-12]. One of the more recent CLT models, referred to as Mesotex [2], is general enough to capture the three-dimensional (3D) elastic properties and the ultimate failure strengths of several types of fabric composites and is very computationally efficient. Models using the MOC that have shown good correlation with experimental results are discussed in references 13 and 14. One of the approaches used is referred to as a four-cell model where the quarter cell RVE is divided into four subcells, as shown in figure 2 [1].

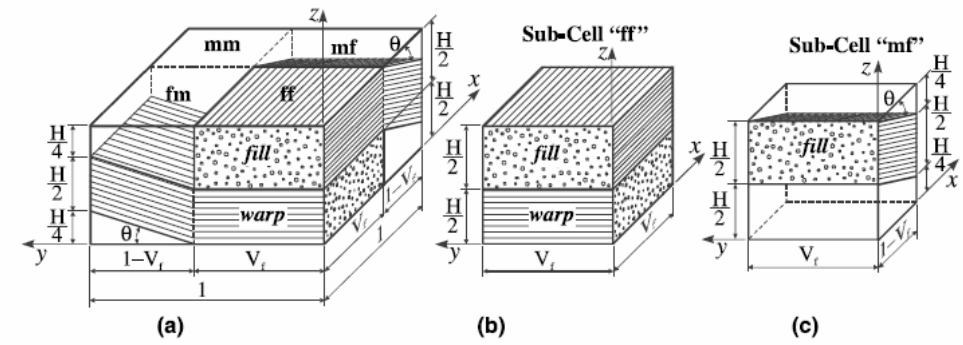

Figure 2. Division of Quarter RVE Into Subcells Using the Four-Cell Method

Using four subcells allows the model to be computationally efficient compared to its similar counterparts. In these MOC models, isostrain and isostress conditions are assumed and the constitutive equations are averaged through the thickness of the RVE. The unit cell is then divided into many subcells and an averaging procedure is performed again by assuming uniform state of stress in the subcells. The stress-strain relations of each subcell can then be obtained and related to the effective stress-strain behavior of the unit cell. Tabiei and Yi [1] developed a simplified MOC model and compared it to previously developed MOC models, the four-cell model, and FE solutions. They concluded that their simplified method could be used as a fast tool for predicting the material properties of fabric composites, but they recommended the four-cell model for most structural analysis problems. Another model using the MOC technique was developed by Naik and Ganesh [15 and 16] and showed good correlation with experimental results. Vandeurzen, et al. [17 and 18], developed what is referred to as a combicell model where the complementary variational principle was used to obtain the stiffness matrix of the unit cell.

Another method for determining the effective material properties of the unit cell is through numerical or FE solutions. Typically, this procedure involves modeling the actual yarn and matrix geometry of the unit cell with many elements. Then virtual tests are conducted by varying the loading and boundary conditions on the unit cell and the results are used to establish the effective material properties. An example of an FE mesh of a woven fabric unit cell is shown in figure 3.

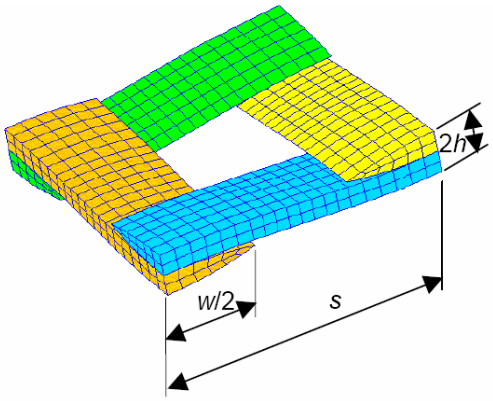

Figure 3. Example of FE Mesh of a Plain Woven Fabric Unit Cell [3]

Using FE models is more computationally expensive compared to using closed-form methods. However, FE models provide detailed stress-strain distributions. The most challenging aspect of this technique is obtaining the appropriate weave architecture of the fabric. Using high-resolution images, such as photomicrograph or SEM images, provides a microscopic view of the yarn geometry. Researchers have been able to fit mathematical functions to these images to accurately model the weave pattern in three dimensions. An example of a photomicrograph image of a fabric similar to Kevlar is shown in figure 4 [8 and 19].

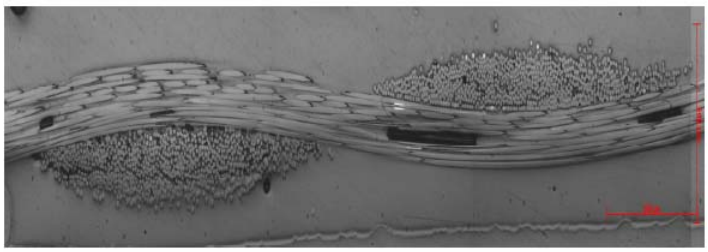

Figure 4. Photomicrograph Image of a Fabric Similar to Kevlar in Cross-Section

Barbero, et al. [19], created a two-dimensional (2D) model of the RVE geometry by fitting a sinusoidal curve to the image. To create a 3D model, the researchers used the 2D fit along with the capabilities of an advanced commercial modeling program. The yarns were modeled with transversely isotropic solid elements and the effective elastic material constants were obtained by varying the boundary conditions and loading on the unit cell. The researchers reported good correlation with experimental values and with values predicted from analytical methods. Peng and Chao [3] used a similar approach by conducting virtual tests on an FE model of the unit cell. However, they went one step further by taking into account the nonlinearity of the material and fitting the results to a shell element equal in size to the unit cell. They developed equations for the elastic modulus, shear modulus, and Poisson ratio as a function of strain. Srirengan, et al. [20], proposed a global/local method that required two stages. First, a macroscopic FE model using a small number of elements and homogenized material properties was created. The results from the global analysis were then used in a more detailed local analysis in which an FE model was used that takes into account the weave geometry.

2.2.1.2 Nonlinear Material Models.

In section 2.2.1.1, various techniques were examined to determine the effective elastic properties of fabric and fabric composites. These properties are generally useful for modeling structural systems that are designed for elastic regime with simple failure criteria. Simulating the performance of the fabric during much more complicated loading, such as in impact events, is necessary when the material is used under these loading conditions. In these situations, a nonlinear material model is needed not only to capture the nonlinear material behavior but also to capture damage growth and failure. Researchers have had varying success using analytical solutions, finite difference solutions, and FE solutions to model impact events.

Several researchers have developed material models to predict the damage evolution and failure strengths of fabrics and fabric composites. Kollegal and Sridharan [21] first developed a 3D FE model to compute the effective elastic properties of a fabric composite. The researchers then

added nonlinearity to the model by including damage and failure of the matrix material and yarns (once failure is reached, the stiffness is reduced to a very small value). The ultimate strength of the composite was approximated and showed good comparison with experimental results. Kollegal, et al. [22], conducted a failure analysis of plain weave fabrics by first obtaining the effective elastic material properties using CLT. In their model, they assumed that damage was a function of the dissipated energy density that yields a power law-type stress-strain relation beyond the elastic limit. Tensile behavior and in-plane shear behavior using this material model compared well with experimental results. Barbero, et al. [23], added to the research discussed in section 2.2.1.1 by adding damage considerations into the material model. In the nonlinear model, damage occurred when the thermodynamic force tensor reached the damage surface in the yarn material. The matrix was assumed to be elastic. Their method required the use of many damage factors that are a function of the yarn material properties. A system of equations is solved to determine these factors. Xue developed a model that accounts for the non-orthogonality of the principal material directions [24]. In Xue's model, shell elements are used to represent the fabric, and unlike many of the aforementioned models the elements are not limited to the unit cell size. The non-orthogonality of the fabric is based on a material matrix that needs to be obtained from matching load versus displacement results from either tensile or biaxial and pure shear experimental tests. The researchers used a picture frame test for the pure shear test and found good correlation with numerical results.

Analytical solutions have been developed for idealized forms of impact with fabrics and fabric composites. By assuming that the fabric deforms as a tetrahedron, Gu [25] developed a method for computing the decrease in a projectile's kinetic energy after penetration. His model is able to account for multiple fabric layers and changes in the mechanical material properties due to strain rate. The model showed good agreement with experimental results. However, it is not robust enough to handle various boundary conditions and projectile geometries.

Several researchers have used finite difference solution techniques to predict fabric behavior during impact events. Roylance, et al. [5], used finite difference techniques and modeled the fabric as a series of pin-jointed, massless fiber elements. The nodes were assigned a mass value so that the model density was equivalent to the actual fabric density. Velocity boundary conditions were applied at the point of impact and at the end of each time increment; the projectile velocity was computed based on the tension exerted on the projectile by the fibers. However, the model was not verified using experimental results. A similar technique was used by Shim, et al. [26]. They also modeled the fabric using pin-jointed, massless fiber elements. However, they accounted for the strain rate effects by using a three-element viscoelastic model. The authors conducted experimental ballistic tests using a spherical steel projectile on Twaron® fabric and compared their results with numerical simulations. They reported good correlation between the two for both the projectile residual velocity and absorbed energy of the fabric. The researchers noted that the accuracy of the model is significantly dependent on the rate sensitivity.

Simons, et al. [27 and 28], used the approach of modeling the response of ballistic fabric by combining a mechanistic constitutive law for the fibers in the yarns in each direction with a damage law that governs fiber breakage. The developed material model, incorporated in LS-DYNA as a user-supplied material model, is used to model ballistic tests and engine containment systems [29 and 30]. They concluded that the choice of analysis parameters and

solution algorithms (particularly the choice of slideline parameters) had a significant effect on energy absorbed calculated in ballistic tests. The sensitivity is said to be related to the high-amplitude, high-frequency stresses caused by the numerical algorithms used to treat interfaces.

Although the use of finite difference techniques has proven to produce accurate results for simulating impact events, the use of FEs can provide solutions to much wider classes of problems. Lim [31] conducted a similar analysis to Shim, et al., by simulating the ballistic impact of a spherical steel projectile with Twaron fabric. However, instead of using one-dimensional, massless elements to model the fabric, the authors used membrane elements and the explicit FE software DYNA3D for the solution technique. They used the predefined Material Type 19 in DYNA3D that is a strain-dependent, isotropic, elastic-plastic model. The model offers strain rate dependence of the elastic modulus, failure stress, yield stress, and tangent modulus by specifying user-defined load curves. The load curves were based on observed results from experimental strain rate tests that had previously been conducted on Twaron fabric. The researchers reported good correlation between experimental and numerical results. However, they noted that improvements and corrections to the model could be made with respect to yarn frictional effects and strain rate effects. Innucci and Willows [32] used LS-DYNA and a damage growth model to simulate the behavior of woven carbon composites when subjected to impact loads. They used plane stress shell elements to represent the composite and considered damage of the fabric fibers and matrix by reducing the effective stiffness values with damage growth until failure. Johnson and Simon [33] conducted a similar analysis using damage mechanics model with shell elements and the explicit FE software PAM-CRASH. They also used a predefined material behavior listed as Material Type 131 that is a partial elastic damage model. Tabiei and Ivanov [4] developed a model for woven fabrics that used a MOC approach to homogenize the unit cell and considered yarn re-orientation or non-orthogonality of the material directions. They implemented the model into LS-DYNA through a user-defined material definition and simulated the impact of a cylindrical projectile with one layer of Kevlar 129 fabric using membrane shell elements to represent the fabric. Damage and failure of the fabric were not considered in the model. Only the deformation of the fabric and projectile displacement versus time could be compared between the simulation and experiment. A good correlation was observed.

A detailed study that compares the MOC and finite element-based virtual testing for multiphysics linear and nonlinear problems is discussed by Krishnan [34].

2.2.1.3 Strain Rate Effects.

The challenges of including load rate effects in a fabric material model are twofold. First, there is difficulty in obtaining accurate experimental results especially at very high strain rates. Second, there is difficulty in choosing a strain rate model. One of the more successful techniques for conducting experimental strain rate tests is the Split Hopkinson bar (SHB) test. Xia and Wang [6 and 7] conducted strain rate tests on Kevlar 49 yarns using the SHB test up to a strain rate of 1350 s^{-1} and found that the fabric had both temperature and rate dependence. The yarn's elastic modulus, peak stress, strain to peak stress, and failure strain each increased with an increase in strain rate. The same properties were shown to decrease with an increase in temperature as well. After conducting strain rate tests on Kevlar KM2 yarns using the SHB, Cheng, et al. [35], concluded that the yarns were not rate-dependent up to a strain rate of

approximately 2450 s^{-1}. Rodriquez, et al. [36], conducted strain rate tests using the SHB on aramid and polyethylene fabrics up to a strain rate of about 1000 s^{-1}. They observed that both types of fabrics were rate sensitive with an increase in peak stress and a decrease in failure strain as the strain rate increased. Shim, et al. [37], conducted strain rate tests using the SHB on Twaron fabric up to a strain rate of approximately 500 s^{-1}. The authors observed that Twaron fabric was very sensitive to loading rate with significant increases in the elastic modulus and peak stress values and a large decrease in the failure strain with an increase in strain rate. It should be noted that the test results are one of the few published where fabric samples, not yarns, were used in the test. The samples were 5 mm wide with a 30-mm gage length. The authors noted that Twaron fabric is very similar to Kevlar 29 in both microstructure and mechanical properties.

As mentioned, there was difficulty choosing an accurate model that captured rate effects. One model, which has previously been noted, is the three-element linear viscoelastic model or three-spring model. A representation of this model is shown in figure 5.

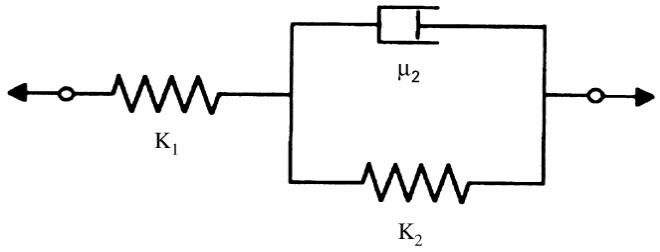

Figure 5. Three-Element Linear Viscoelastic Model

The primary and secondary bond of the material are represented by stiffness K_1 and K_2, respectively. Viscous effects caused by polymer chains slipping and sliding relative to each other are accounted for in the viscosity constant μ_2. The stress-strain relationship associated with the three-element model is described by

$$\left(1+\frac{K_2}{K_1}\right)\sigma+\left(\frac{\mu_2}{K_1}\right)\dot{\sigma}=K_2\varepsilon+\mu_2\dot{\varepsilon} \tag{1}$$

The three-element linear viscoelastic model showed good correlation with the dynamic experimental results for Twaron fabric. Other popular strain rate models include the Cowper-Symonds model that accounts for rate effects on the yield stress $(\bar{\sigma})$ as

$$\bar{\sigma}=\bar{\sigma}_0\left[1+\left(\frac{\dot{\varepsilon}}{C}\right)^{\frac{1}{P}}\right] \tag{2}$$

where $\bar{\sigma}_0$ is the yield stress at zero strain rate and C and P are determined from experiments. Yet another model is a variation of the Johnson-Cook model expressed as

$$\bar{\sigma} = \bar{\sigma}_0 \left[1 + C \ln \left(\frac{\dot{\varepsilon}_P}{\dot{\varepsilon}_0} \right) \right] \tag{3}$$

where C and $\dot{\varepsilon}_0$ are determined from experiments. Söderberg and Sellgren [38] conducted a study on the influence of using various forms of the Johnson-Cook and the Cowper-Symonds equations in FE simulations of high-speed crash events with metals. They concluded that the choice of strain rate model did have an influence on the simulation results. They noted that for the metals tested, the Cowper-Symonds model fit the experimental results well at both high and low strain rates.

2.2.2 Fabric Modeling Methodology.

As previously discussed, there are several techniques for modeling the fabric using FEs. A micromechanical approach captures the actual fabric geometry by modeling each individual yarn and its weave pattern with solid FEs. Figure 6 shows an example of a micromechanical FE model of a woven fabric using Kevlar 49 material as an example [39].

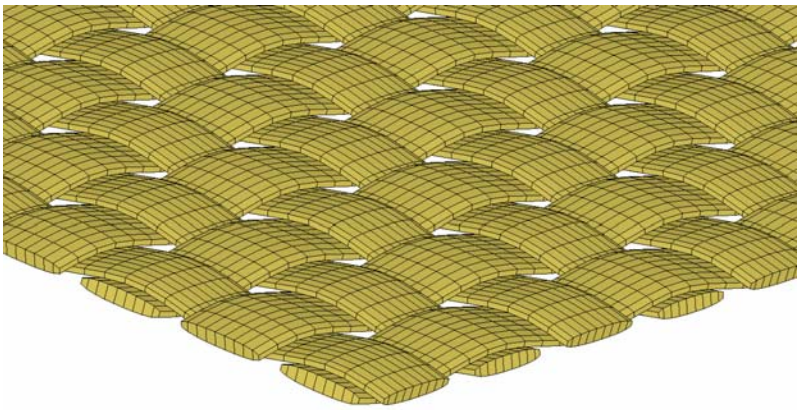

Figure 6. Micromechanical FE Model of Kevlar 49

This approach is very computationally expensive due to the large number of FEs required to construct even a simple model, let alone one for use in propulsion engine containment systems. Another approach is the unit cell technique where the behavior of a repetitive unit of geometry is determined and related to a continuum element such as a shell, membrane, or solid element. An example of a unit cell for Kevlar 49 is shown in figure 7. It should be noted that this approach was not used in the ASU model.

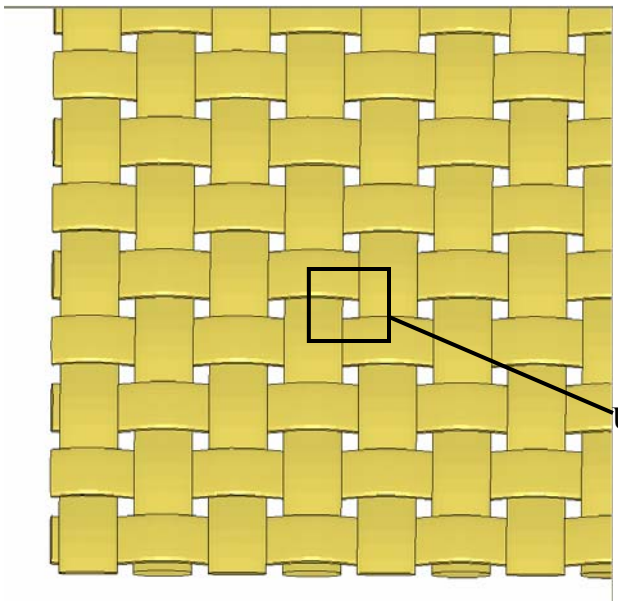

Figure 7. Example of a Unit Cell for Kevlar 49

While this approach has potential advantages, especially for computing equivalent material properties of composites, it is relatively expensive both in terms of building the FE models as well as the time it takes for these simulations to run to completion. In this part of the research, the fabric is assumed to behave as a continuum material, as shown in figure 8.

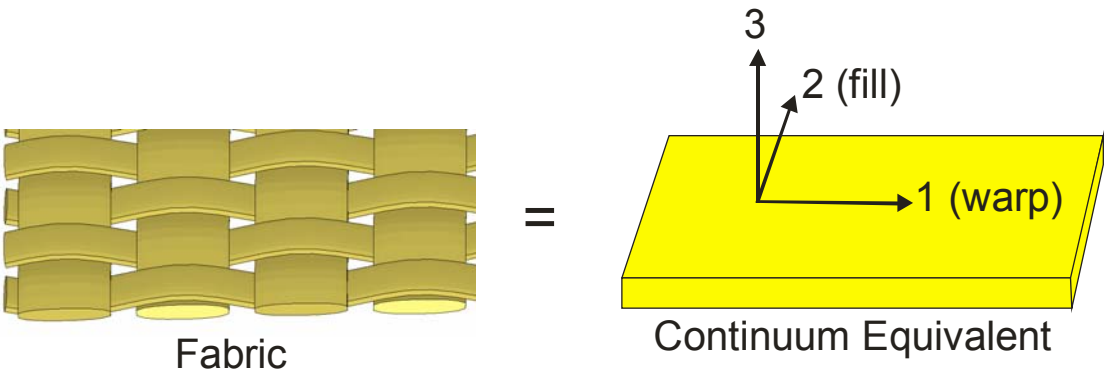

Figure 8. Modeling the Fabric as a Continuum

The material properties (or constitutive model) of the fabric are determined through experimental testing of fabric samples and related to shell, membrane, or solid elements through the material model. While the approach used in the literature research is expensive, the other approaches discussed also require some amount of testing to drive the methodology. In the following sections, the development details of ASUumatV1.0 are presented.

2.2.3 Fabric Constitutive Behavior.

The constitutive behavior can be complex for composite materials exhibiting orthotropic material behavior. In this research, simplifying assumptions were made to fully capture the complexities

of the stress-strain behavior in the principal material directions. The fabric has negligible stiffness perpendicular to both fabric material directions and hence, those properties were assumed to be zero. No coupling effect between the material directions was assumed—the Poisson's ratios were assumed to be zero. Although the Poisson's ratios were measured during uniaxial tension tests, this assumption was required to model the nonlinearity in the principal material directions. Future versions of the model should investigate the effects of this assumption. The constitutive behavior used in the material model in compliance incremental form and in stiffness incremental form is shown in equations 4 and 5, respectively. Material direction 11 is the main longitudinal direction of the fabric (warp direction), direction 22 is the direction along the width of the fabric (fill direction), and direction is the direction perpendicular to both warp and fill directions (see figure 8).

$$\begin{bmatrix} \Delta\varepsilon_{11} \\ \Delta\varepsilon_{22} \\ \Delta\varepsilon_{33} \\ \Delta\varepsilon_{12} \\ \Delta\varepsilon_{31} \\ \Delta\varepsilon_{23} \end{bmatrix} = \begin{bmatrix} \frac{1}{E_{11}} & 0 & 0 & 0 & 0 & 0 \\ 0 & \frac{1}{E_{22}} & 0 & 0 & 0 & 0 \\ 0 & 0 & 0 & 0 & 0 & 0 \\ 0 & 0 & 0 & \frac{1}{2G_{12}} & 0 & 0 \\ 0 & 0 & 0 & 0 & \frac{1}{2G_{31}} & 0 \\ 0 & 0 & 0 & 0 & 0 & \frac{1}{2G_{23}} \end{bmatrix} \begin{bmatrix} \Delta\sigma_{11} \\ \Delta\sigma_{22} \\ \Delta\sigma_{33} \\ \Delta\sigma_{12} \\ \Delta\sigma_{31} \\ \Delta\sigma_{23} \end{bmatrix} \tag{4}$$

$$\begin{bmatrix} \Delta\sigma_{11} \\ \Delta\sigma_{22} \\ \Delta\sigma_{33} \\ \Delta\sigma_{12} \\ \Delta\sigma_{31} \\ \Delta\sigma_{23} \end{bmatrix} = \begin{bmatrix} E_{11} & 0 & 0 & 0 & 0 & 0 \\ 0 & E_{22} & 0 & 0 & 0 & 0 \\ 0 & 0 & 0 & 0 & 0 & 0 \\ 0 & 0 & 0 & 2G_{12} & 0 & 0 \\ 0 & 0 & 0 & 0 & 2G_{31} & 0 \\ 0 & 0 & 0 & 0 & 0 & 2G_{23} \end{bmatrix} \begin{bmatrix} \Delta\varepsilon_{11} \\ \Delta\varepsilon_{22} \\ \Delta\varepsilon_{33} \\ \Delta\varepsilon_{12} \\ \Delta\varepsilon_{31} \\ \Delta\varepsilon_{23} \end{bmatrix} \tag{5}$$

The values for E_{11}, E_{22}, G_{12}, G_{31}, and G_{23} are a function of several factors, including the current stress and strain, the stress and strain history, and the strain rate. The determination of these material properties will be discussed in the following sections.

2.2.4 Determination of E_{11} and E_{22}.

To determine the fabric's stress-strain behavior in the principal material directions, experimental tests at ASU were conducted. Additionally, strain rate effects on this behavior were based on published experimental results [6 and 7].

2.2.4.1 Uniaxial Tension Tests.

Static, uniaxial tension tests in both the warp and fill directions were performed at ASU. A total of six tests were conducted in the warp direction, and a total of four tests were conducted in the fill direction. The warp direction test setup is shown in figure 9. Figures 10 and 11 show the uniaxial stress-strain response for both the warp and fill directions, respectively. The stress values were computed based on the measured thickness of 1420 D 17x17 weave Kevlar 49 of 0.011″. For full details of the test procedure, as indicated in figures 9, 10, and 11, see references 1, 2, and 40. More detailed ASU test results can also be found in Part 2 of this report.

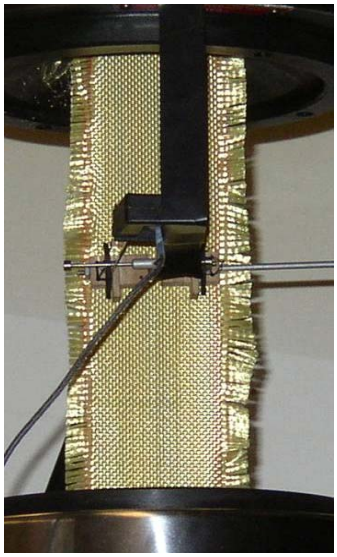

Figure 9. Uniaxial Tension Test Setup for Warp Direction

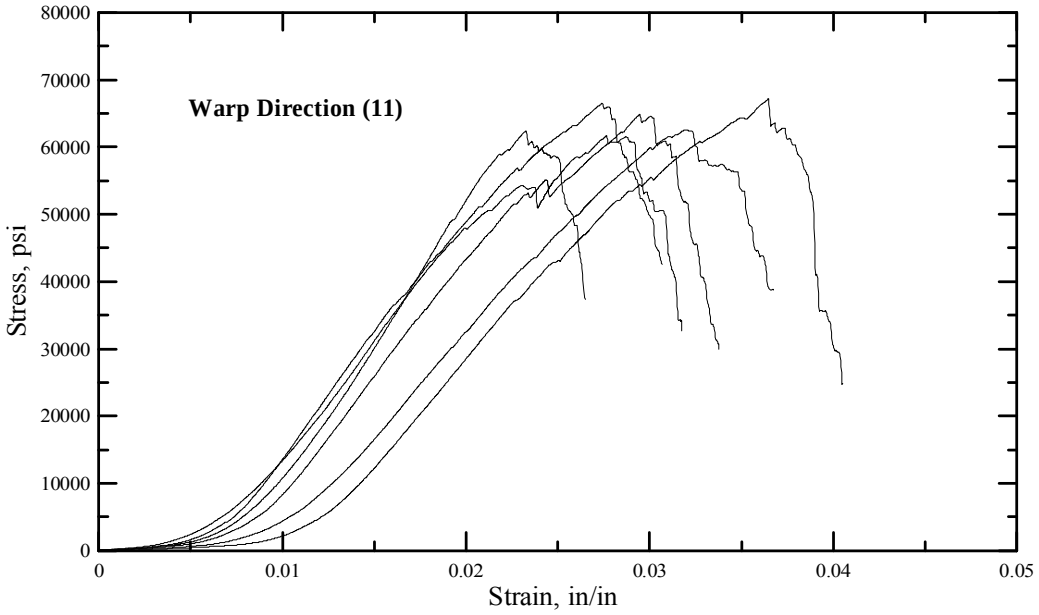

Figure 10. Kevlar 49 Warp Direction Uniaxial Stress-Strain Results

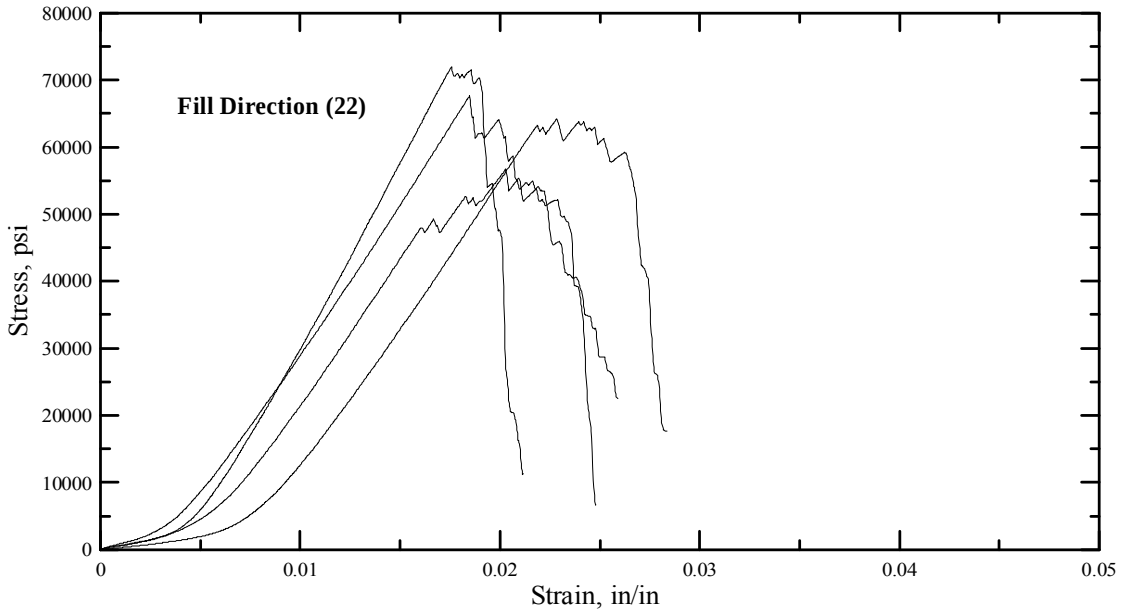

Figure 11. Kevlar 49 Fill Direction Uniaxial Stress-Strain Results

From the experimental tension tests, it is clear that in both the warp and fill directions, the fabric has three distinct regions during loading—an initial region of low stiffness resulting from the low stress required to straighten the yarns (or crimp region), a region of high stiffness where strain increases results in large stress increases (or elastic region), and a region of negative stiffness where the stress decreases rapidly with an increase in strain (or post-peak or softening region). The fill direction has a somewhat different stress-strain response as it reaches relatively the same peak stress as the warp direction, but this peak occurs at a smaller strain value. In other words, the stiffness in the elastic region of the fill direction is greater than in the warp direction. The fill direction also has a smaller crimp region compared to the warp direction. These differences are due to the fabrics' asymmetrical geometry. From photomicrographs, it is clear that the fill direction has slightly different weave geometry than the warp direction.

2.2.4.2 Pre-Peak Behavior in Material Model.

Experimental test results show the behavior of the fabric to be nonlinear in both material directions. The stiffness values are not constant. However, they can be reasonably well approximated by a linear function. For this reason, a simplified approach was used to model the pre-peak stiffness values. A piecewise, linear approximation of the crimp region and elastic region was used and is shown along with the tension test results in figures 12 and 13.

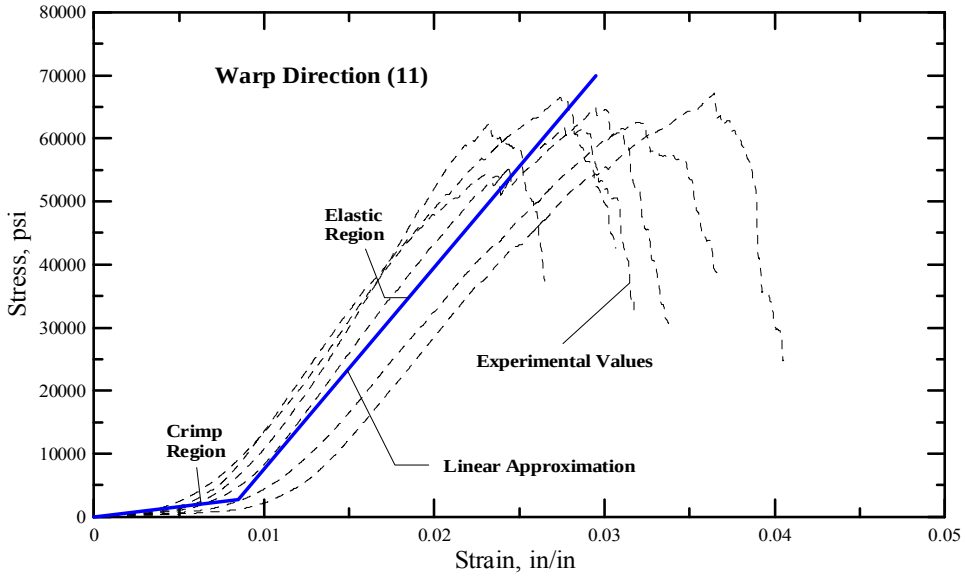

Figure 12. Kevlar 49 Warp Direction Uniaxial Stress-Strain Results With Linear Approximation for Pre-Peak

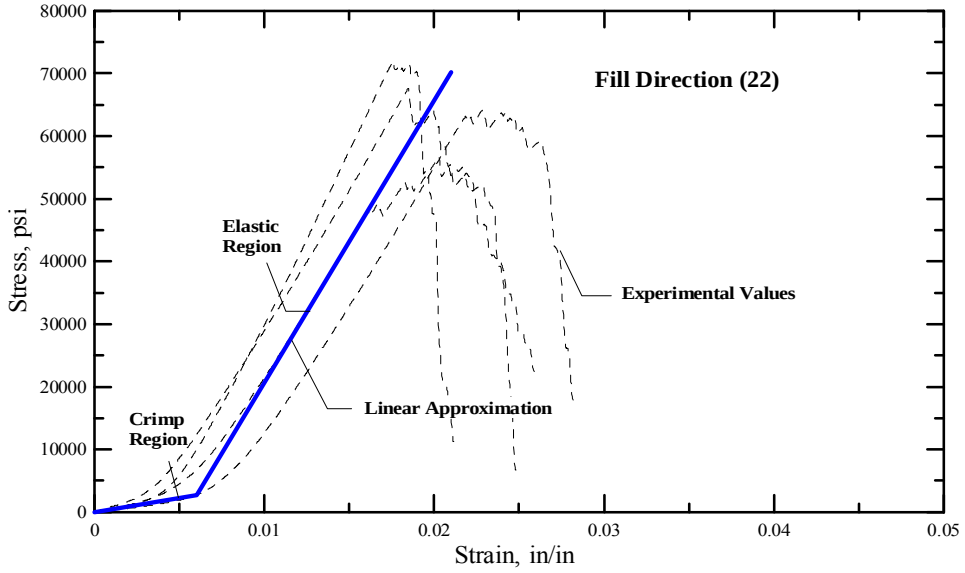

Figure 13. Kevlar 49 Fill Direction Uniaxial Stress-Strain Results With Linear Approximation for Pre-Peak

The linear approximation was constructed as follows. First, the maximum crimp strain and stress at maximum crimp strain were chosen using the average values from the test specimens. Similarly, the strain at peak stress and the peak stress were then chosen by identifying those values for each test and then computing the average value. The peak stress was then adjusted so that the area under the pre-peak region of the curves was approximately equal for both the linearly approximated curves and the average of the experimental curves. An elastic stiffness and crimp stiffness could then be computed. It was determined that the crimp stiffness was approximately 10% of the elastic stiffness in both the warp and fill directions.

The final values used in the material model to describe the warp direction pre-peak behavior were a crimp strain (ε_{11}^{crp}) of 0.0085, a strain to peak stress (ε_{11}^{max}) of 0.0295, an elastic stiffness (E_{11}) of 3.2(10^6) psi, and a crimp stiffness (ε_{11}^{crp}) of 3.2(10^5) psi. In the fill direction, the values were a crimp strain (ε_{22}^{crp}) of 0.0060, a strain to peak stress (ε_{22}^{max}) of 0.0210, an elastic stiffness (E_{22}) of 4.5(10^6) psi, and a crimp stiffness (ε_{22}^{crp}) of 4.5(10^5) psi. These values are shown for each respective material direction in figures 14 and 15.

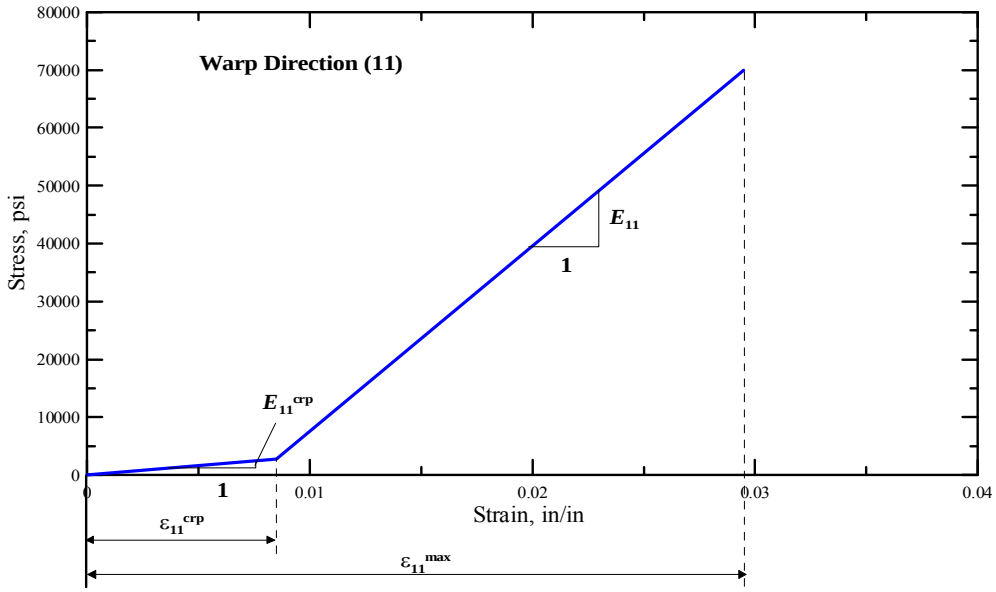

Figure 14. Warp Direction Material Constants for Pre-Peak Stress-Strain Response in Material Model

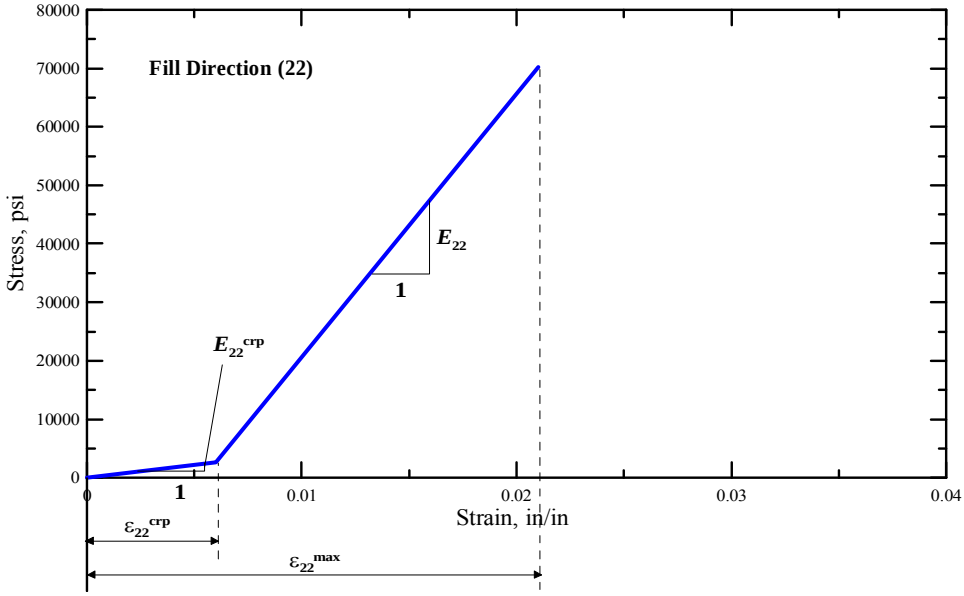

Figure 15. Fill Direction Material Constants for Pre-Peak Stress-Strain Response in Material Model

2.2.4.3 Post-Peak and Failure Behavior in Material Model.

The primary mode of failure of Kevlar 49 is the breakage of the warp or fill direction yarns. Therefore, a simple approach was used to model fabric failure in an FE simulation: once the element representing the fabric experienced a critical level of strain in either the warp or fill directions, the element was considered to have failed. There were several options for the failure strain value. One was to assume the failure strain was simply the strain reported at the end of the tension tests. However, after analyzing the deformed fabric samples, it was determined that much larger strains were required to fully fail the fabric yarns. One of the fabric samples at the end of the warp direction tension test is shown in figure 16.

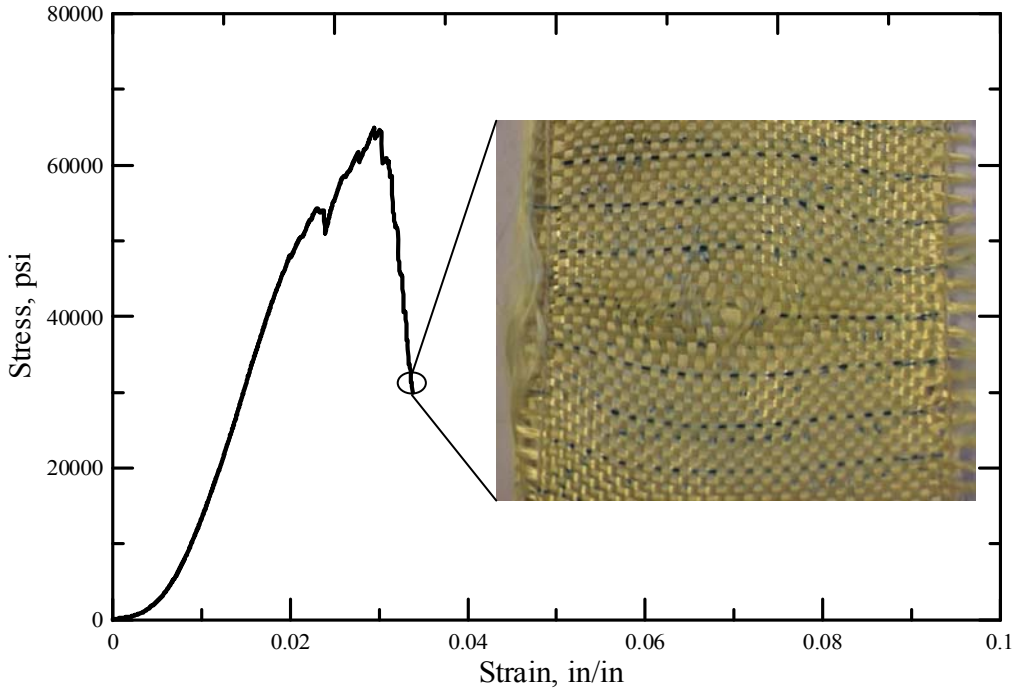

Figure 16. Fabric Sample at end of Warp Direction Tension Test

From the deformation shown in the figure, it is clear that the fabric can experience strains larger than the last reported strain value from the test results. Testing was terminated when the total displacement reached the maximum stroke available for the test machine. To simplify and simulate this in the material model, the post-peak region was approximated with a linear region followed by a nonlinear region up until fabric failure. The linear post-peak region stiffness was determined by fitting a linear curve to the experimental results for both the warp and fill directions. It was found that in both directions, the linear region post-peak stiffness was approximately -2.5 times the elastic stiffness, indicating softening behavior. Thus, the linear region stiffness for the warp (E_{11}^{soft}) and fill (E_{22}^{soft}) directions was $-8.0(10^6)$ psi and $-11.25(10^6)$ psi, respectively. A level of strain or stress had to be assumed for where the nonlinear post-peak region began. In the material model, it was assumed that if the stress was less than 15,000 psi in the warp or fill directions, then the stress-strain response was in the post-peak nonlinear region in that respective direction. Additional tests showed that the fabric began

to elongate rapidly at approximately this value of stress. The stress in the nonlinear region for the warp and fill directions was assumed as follows.

$$\sigma_{11} = \sigma^* \left(1 - \left(\frac{\varepsilon_{11} - \varepsilon_{11}^*}{\varepsilon_{fail} - \varepsilon_{11}^*} \right)^{dfac} \right) \tag{6}$$

$$\sigma_{22} = \sigma^* \left(1 - \left(\frac{\varepsilon_{22} - \varepsilon_{22}^*}{\varepsilon_{fail} - \varepsilon_{22}^*} \right)^{dfac} \right) \tag{7}$$

In the above equations, σ^* and ε^* are the stress and strain values at which the nonlinear region begins in each respective direction, ε_{fail} is the failure strain in each respective direction, and *dfac* is a factor that specifies the rate of decrease in stress. The values for ε^* were computed internally by the material model. The failure strain in both the warp and fill directions were assumed to be 0.2, and the factor *dfac* was assumed to be 0.3. The rate of stress decrease using these equations was limited to the post-peak stiffness. Figures 17 and 18 show the stress-strain response (used in the FE simulations) for the pre- and post-peak behavior for the warp and fill directions, respectively.

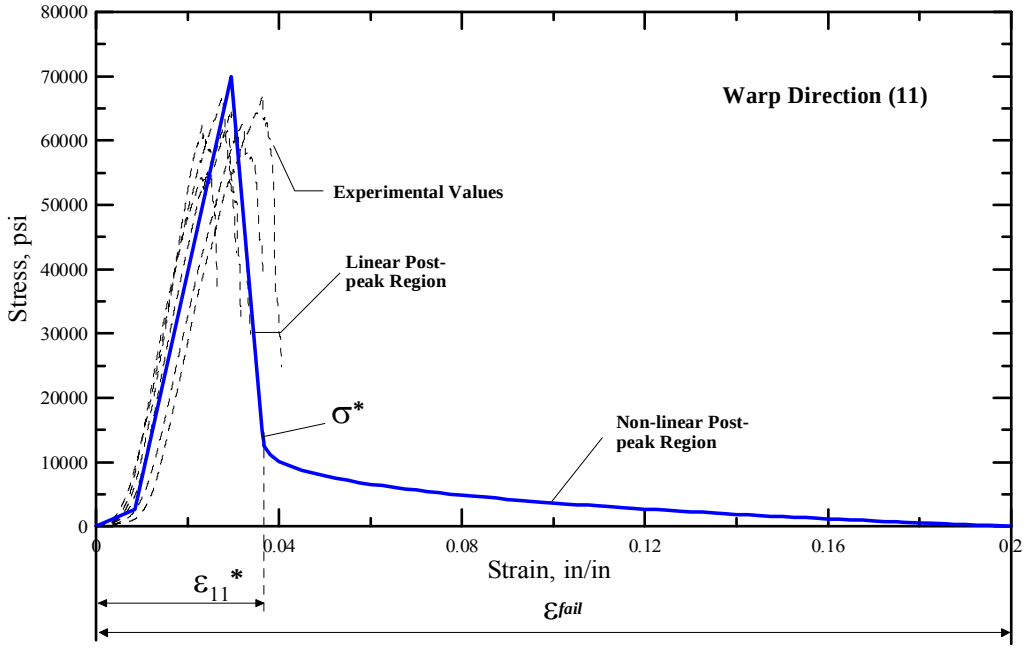

Figure 17. Kevlar 49 Warp Direction Uniaxial Stress-Strain Results With Approximation for Pre- and Post-Peak Behavior

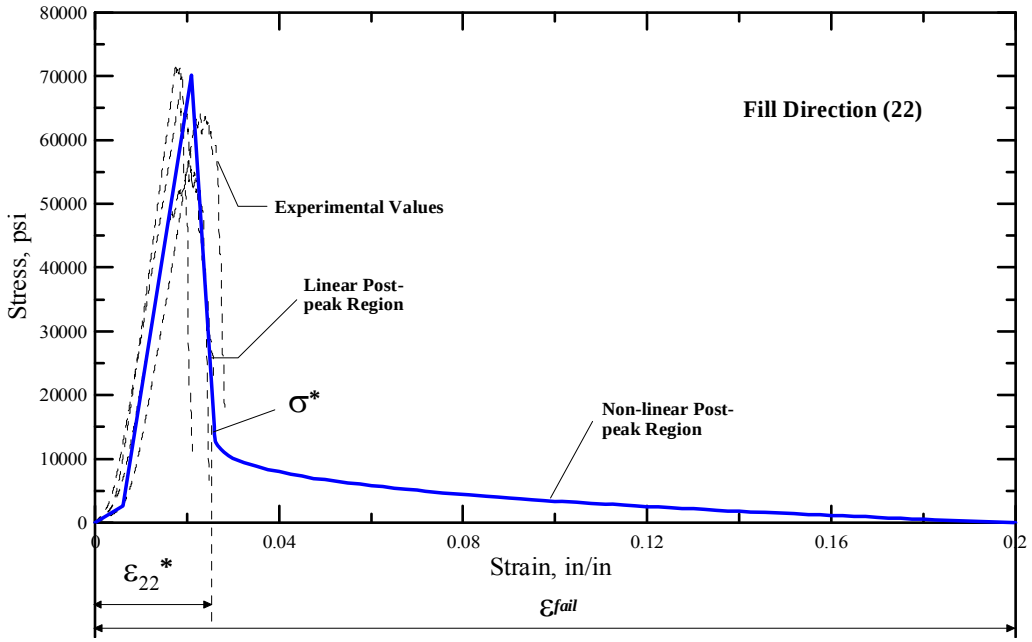

Figure 18. Kevlar 49 Fill Direction Uniaxial Stress-Strain Results With Approximation for Pre- and Post-Peak Behavior

2.2.4.4 Unloading/Reloading and Compression Behavior in Material Model.

When the fabric is subjected to impact loads, it can load and unload many times throughout the event. It is important to determine its cyclic behavior and model it correctly. Cyclic tests in the warp direction for three Kevlar 49 samples were conducted to determine the fabric's unloading and reloading behavior. The results from the cyclic tests are shown in figure 19 [41].

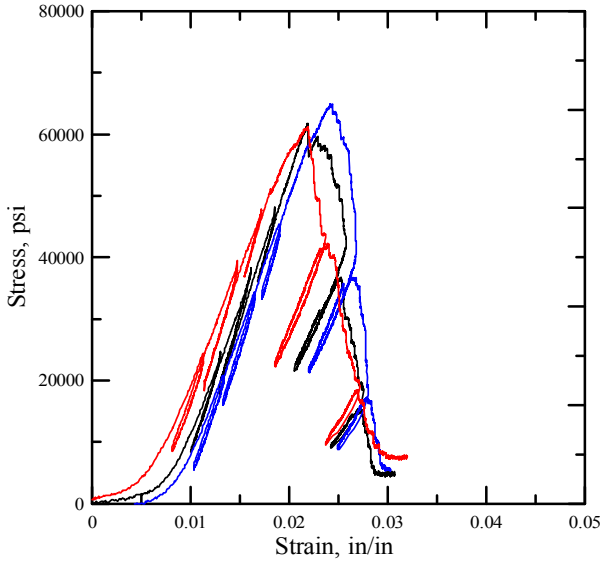

Figure 19. Kevlar 49 Warp Direction Cyclic Loading Stress-Strain Results

The test results show that in the elastic region, the fabric unloads and reloads approximately along the same path but at a rate that is about 1.5 times the elastic stiffness. In the post-peak region, the unloading and reloading stiffness decreases as the strain increases, likely due to an increase in the fiber breakage after the fabric's peak behavior. It should be noted that there is a difference between the strain at peak stress from the cyclic test results compared to the uniaxial test results previously reported. The cyclic test fabric samples showed that the warp direction had an average strain to peak stress of approximately 0.0240, whereas the uniaxial test samples showed an average of approximately 0.0295. This could be due to the variability in the stress-strain response of the fabric. Additional uniaxial tension tests conducted by Sharda [40] verified the strain to peak stress values from figure 10, or approximately 0.0295. Since cyclic testing of the fill direction was not conducted, it was assumed that the unloading and reloading stiffness of the fill direction was similar to the warp direction, or 1.5 times the elastic stiffness.

In the material model, the unloading and reloading stiffness were expressed as a factor of 1.5 times the elastic stiffness. Thus, the unloading and reloading stiffness for the warp (E_{11}^{unl}) and fill directions (E_{22}^{unl}) were 4.8(10^6) psi and 6.75(10^6) psi, respectively. For simplicity, the unloading and reloading stiffness were assumed to be constant for all values of strain; thus, the softening of the unloading and reloading stiffness was not modeled. This assumption proved adequate in the FE simulations as unloading at high strain values in the post-peak region rarely occurred in failing elements.

Kevlar 49 fabric has negligible compressive stiffness. However, to avoid numerical instabilities, a very small stiffness was assumed when the FE experiences compression. The compressive stiffness was taken as 0.5% of the elastic stiffness. Thus, the compressive stiffness in the warp (E_{11}^{comp}) and fill (E_{22}^{comp}) directions were 1.6(10^4) psi and 2.25(10^4) psi, respectively. Figure 20(a) and (b) shows the general unloading, reloading, and compressive behavior of the fabric's warp and fill directions assumed in the material model, respectively.

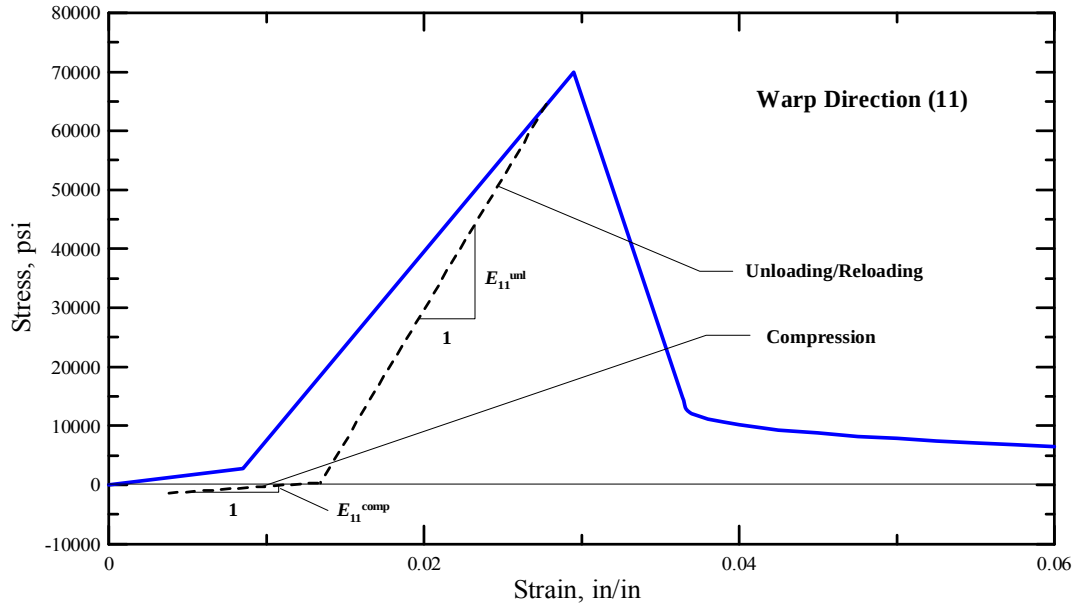

(a)

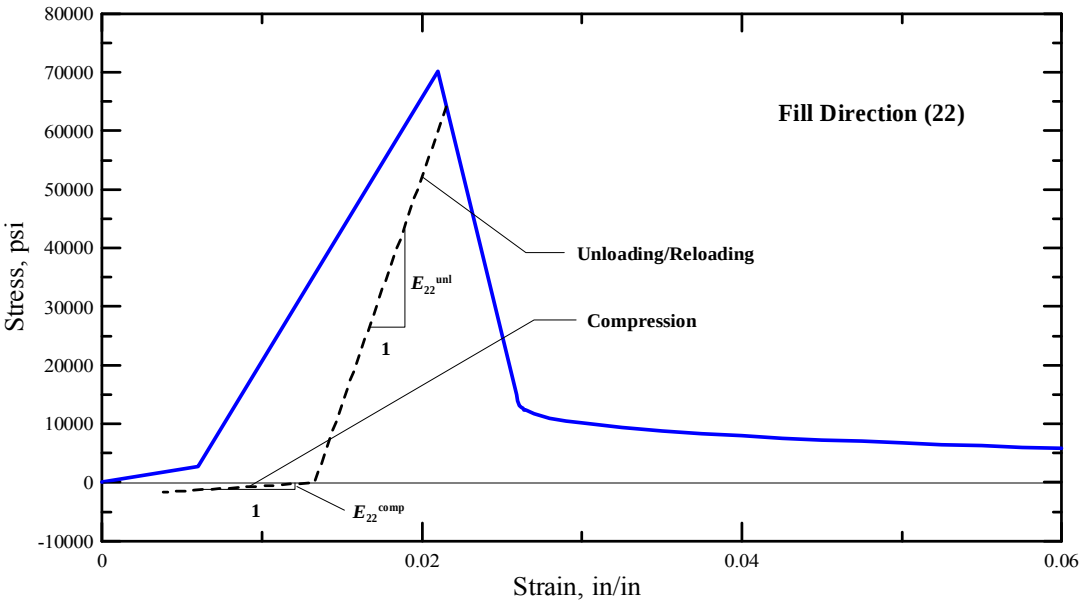

(b)

Figure 20. Unloading/Reloading and Compression Behavior Assumed in Material Model for (a) Warp and (b) Fill Directions

2.2.4.5 Strain Rate Effects.

As previously discussed, little research has been conducted on the effects of strain rate on Kevlar 49, especially for the high strain rates encountered in engine containment system simulations. Very few publications are available that document Kevlar's strain rate effects. Xia

and Wang [6 and 7] report having achieved strain rate tests of Kevlar 49 yarns up to a strain rate of 1350 s^{-1}. The results from their research are shown in figure 21.

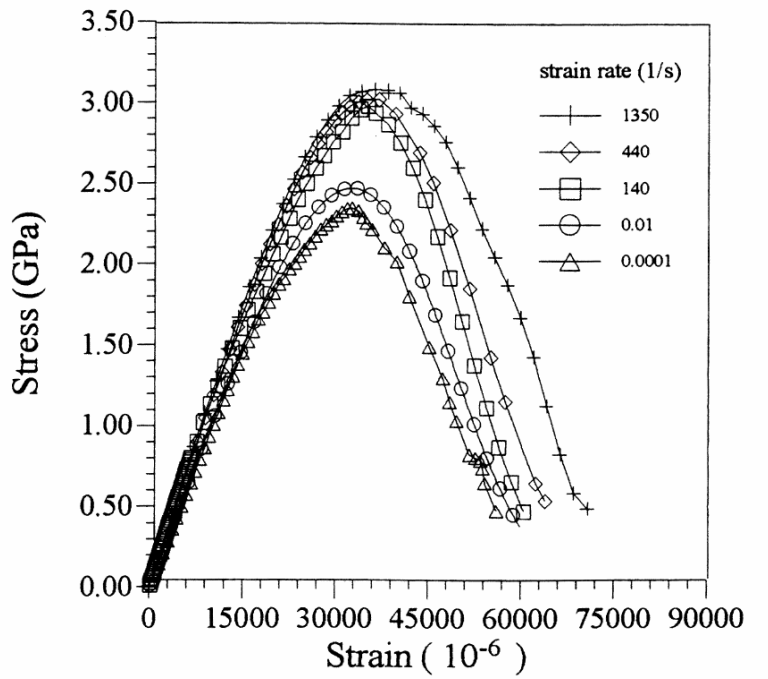

Figure 21. Strain Rate Effect on the Stress-Strain Behavior of Kevlar 49 Yarns [6 and 7]

The results show that there is an increase in the yarn peak stress and failure strain with an increase in strain rate. The increase in peak stress is caused by an increase in stiffness and an increase in the strain at peak stress. In the development of the rate-sensitive constitutive model that is used in the current study, it was assumed that these results for the Kevlar yarns can also be extended to represent the behavior of fabric swath [42]. The Cowper-Symonds model [43] was chosen to simulate the strain rate effects based on the data in figure 21.

The general Cowper-Symonds model accounts for increases in the peak stress of a material with an increase in strain rate, as shown in equation 8.

$$\sigma^{\max(adj)} = \sigma^{\max}\left(1+\frac{\dot{\varepsilon}}{C}\right)^{\frac{1}{P}} \tag{8}$$

In equation 8, $\sigma^{\max}$ is the static peak stress, $\sigma^{\max(adj)}$ is the adjusted peak stress due to strain rate effects, $\dot{\varepsilon}$ is the strain rate, and the C and P factors are unique to each material and need to be determined experimentally. The model captures the nonlinear strain rate effects that many materials experience by simulating the rapid increase in material properties at a lower range of strain rates and a less rapid increase in material properties at very high strain rates.

In the material model, the elastic stiffness and strain to peak stress were assumed to be a function of the strain rate using the Cowper-Symonds model. The peak stress was indirectly assumed to

be a function of the strain rate as the elastic stiffness and the strain at peak stress was increased. The elastic stiffness in the warp and fill directions was adjusted based on the strain rate, as shown in equations 9 and 10, respectively.

$$E_{11}^{adj} = E_{11}\left(1+\frac{\dot{\varepsilon}_{11}}{C_E}\right)^{\frac{1}{P_E}} \tag{9}$$

$$E_{22}^{adj} = E_{22}\left(1+\frac{\dot{\varepsilon}_{22}}{C_E}\right)^{\frac{1}{P_E}} \tag{10}$$

In equations 9 and 10, E is the static elastic stiffness in each respective direction, E^{adj} is the adjusted elastic stiffness in each respective direction, $\dot{\varepsilon}$ is the strain rate in each respective direction, and C_E and P_E are Cowper-Symonds C and P factors describing the strain rate effects on the elastic stiffness. The crimp stiffness, crimp strain, unloading and reloading stiffness, and the post-peak stiffness were assumed not to be functions of strain rate.

The effective strain at peak stress was adjusted based on the strain rate as shown in equations 11 and 12, respectively. The effective strain at peak stress is defined as the strain-to-peak stress minus the crimp strain. For example, in the warp direction, the effective strain-to-peak stress is 0.0295 – 0.0085 = 0.021.

$$\varepsilon_{11}^{\max(adj)} = \varepsilon_{11}^{\max}\left(1+\frac{\dot{\varepsilon}_{11}}{C_\varepsilon}\right)^{\frac{1}{P_\varepsilon}} \tag{11}$$

$$\varepsilon_{22}^{\max(adj)} = \varepsilon_{22}\left(1+\frac{\dot{\varepsilon}_{22}}{C_\varepsilon}\right)^{\frac{1}{P_\varepsilon}} \tag{12}$$

In equations 11 and 12, $\varepsilon^{\max}$ is the effective strain at peak stress in each respective direction, $\varepsilon^{\max(adj)}$ is the adjusted effective strain at peak stress in each respective direction, $\dot{\varepsilon}$ is the strain rate in each respective direction, and C_ε and P_ε are Cowper-Symonds C and P factors. The failure strain was not assumed to be a function of the strain rate since the value is estimated to be much higher than the test results.

The strain rate value was estimated using a backward difference approximation, as follows

$$\dot{\varepsilon}_{11} = \frac{\varepsilon_{11}^{t} - \varepsilon_{11}^{t-\Delta t}}{\Delta t} \tag{13}$$

$$\dot{\varepsilon}_{22} = \frac{\varepsilon_{22}^{t} - \varepsilon_{22}^{t-\Delta t}}{\Delta t} \tag{14}$$

where ε^{t} is the strain at the current time step in each respective direction, $\varepsilon^{t-\Delta t}$ is the strain at the previous time step in each respective direction, and Δt is the current time increment.

The factors C_E, P_E, C_ε, and P_ε were determined by fitting the normalized effect on the peak stress on the material model using those factors with the normalized effect on the peak stress from the experimental results. The normalized peak stress is defined as the adjusted peak stress divided by the static peak stress. Thus in the material model, the normalized peak stress in the warp direction can be represented as follows

$$\frac{\sigma_{11}^{\max(adj)}}{\sigma_{11}^{\max}} = \frac{1}{\sigma_{11}^{\max}}\left(\varepsilon_{11}^{crp} E_{11}^{crp} + \varepsilon_{11}^{\max(adj)} E_{11}^{adj}\right) \tag{15}$$

where ε^{crp} is the crimp strain and E^{crp} is the crimp stiffness. Initial simulations found that the element strain rate exceeded the maximum level found in the experimental tests, often times reaching 10,000 s^{-1} or even 15,000 s^{-1}. Since experimental data at these high strain rates are neither available in the public domain nor likely to be obtained experimentally in the near future, the fitting was based on an estimated extrapolation of the experimental results. The values for C_E, P_E, C_ε, and P_ε that best correlated with the experimental results were 5.0 s^{-1}, 40.0, 5.0 s^{-1}, and 40.0, respectively. Figure 22 shows the normalized peak stress as a function of strain rate using these factors with the Cowper-Symonds model along with the experimental yarn results. The results are shown up to a strain rate of 10,000 s^{-1}.

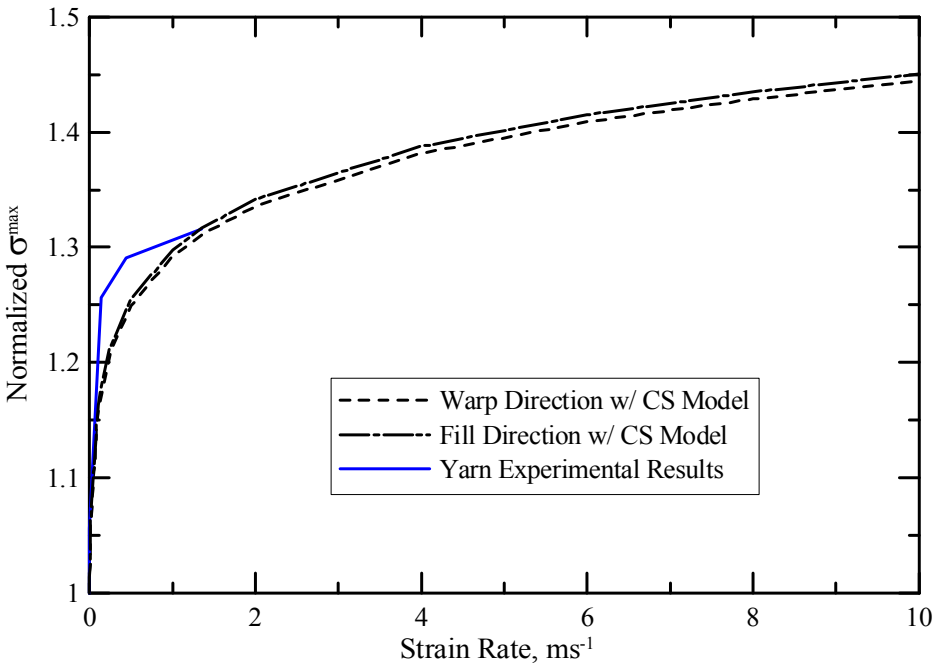

Figure 22. Normalized Peak Stress as a Function of Strain Rate for Material Strain Rate Cowper-Symonds Model and Experimental Results

During a simulation, an element's strain rate is not constant for all time steps. This does not pose a problem for the elastic stiffness strain rate model as the stiffness is simply allowed to change at

each step, depending on the current strain rate. However, in the effective strain at peak stress model, the strain at peak stress cannot be allowed to constantly change throughout the analysis. This would cause complications in the stress-strain path of the element. For this reason, an assumption was made that the effective strain at peak stress would be a function of the maximum strain rate that the element experiences during the analysis. Equations 11 and 12 can now be modified to

$$\varepsilon_{11}^{\max(adj)} = \varepsilon_{11}^{\max}\left(1+\frac{\dot{\varepsilon}_{11}^{\max}}{C_{\varepsilon}}\right)^{\frac{1}{P_{\varepsilon}}} \tag{16}$$

$$\varepsilon_{22}^{\max(adj)} = \varepsilon_{22}^{\max}\left(1+\frac{\dot{\varepsilon}_{22}^{\max}}{C_{\varepsilon}}\right)^{\frac{1}{P_{\varepsilon}}} \tag{17}$$

where $\varepsilon^{\max}$ is the maximum strain rate experienced by the element in each respective direction.

Figures 23 and 24 show the effects of the strain rate model on the stress-strain response in the warp and fill directions, respectively. Constant strain rates are assumed in the figures. The strains are not plotted to full failure.

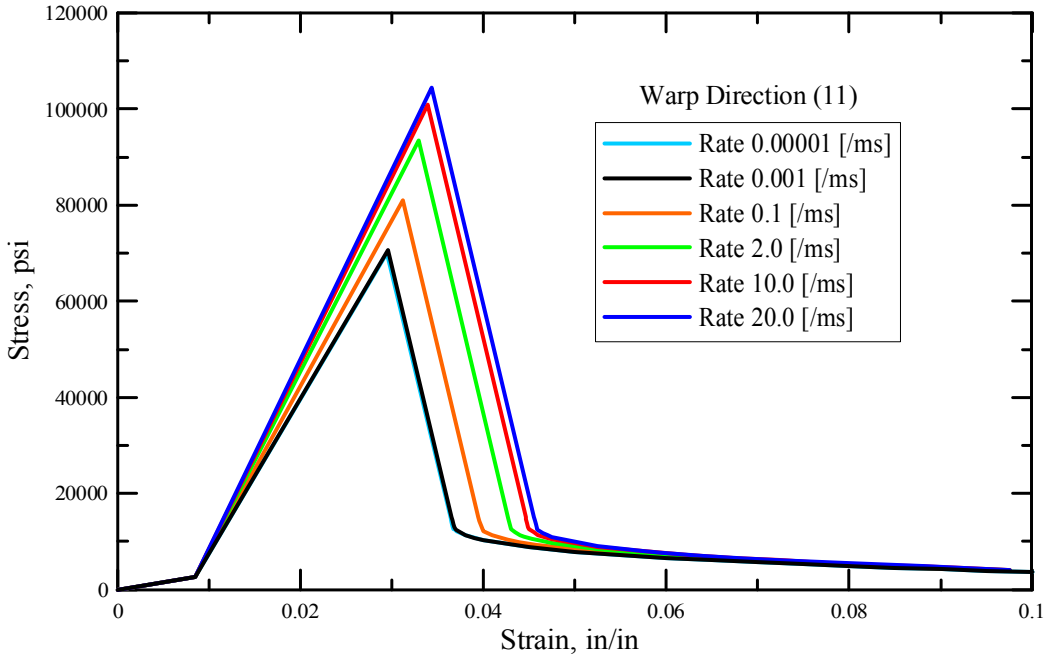

Figure 23. Strain Rate Effects on the Warp Direction Stress-Strain Behavior

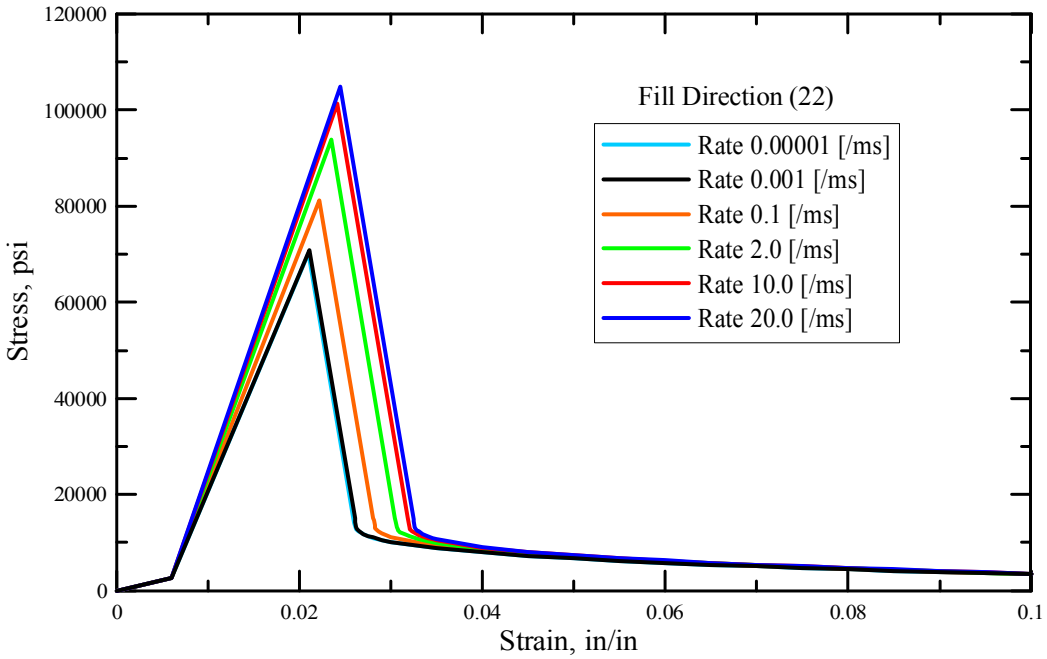

Figure 24. Strain Rate Effects on the Fill Direction Stress-Strain Behavior

2.2.5 Determination of Shear Modulus (G_{12}).

The shear modulus value (G_{12}) was determined based on picture frame shear tests that were conducted at ASU. For details of the picture frame test procedure, see reference 40. Figure 25 shows the test setup with a 5″ by 5″ sample.

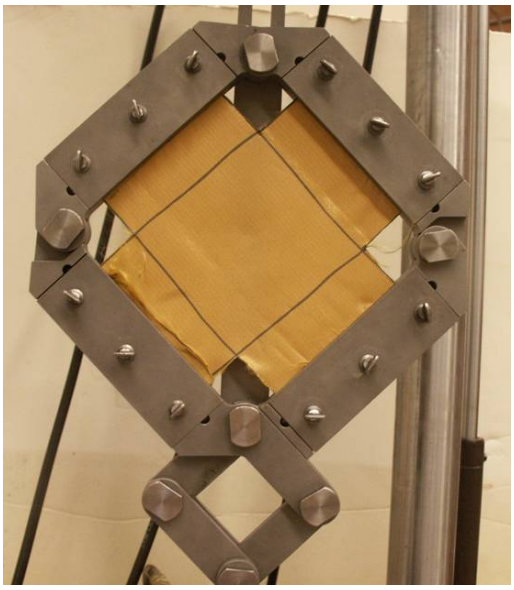

Figure 25. Kevlar 49 Picture Frame Shear Test Setup

For the purpose of describing the shear behavior in the continuum constitutive model (see equation 5), it is necessary to compute an equivalent engineering shear stress versus shear strain relationship. The engineering shear stress versus engineering shear strain results from one test is shown in figure 26. The stress values were computed based on the measured thickness of the fabric (0.011″). Additional tests showed a similar behavior.

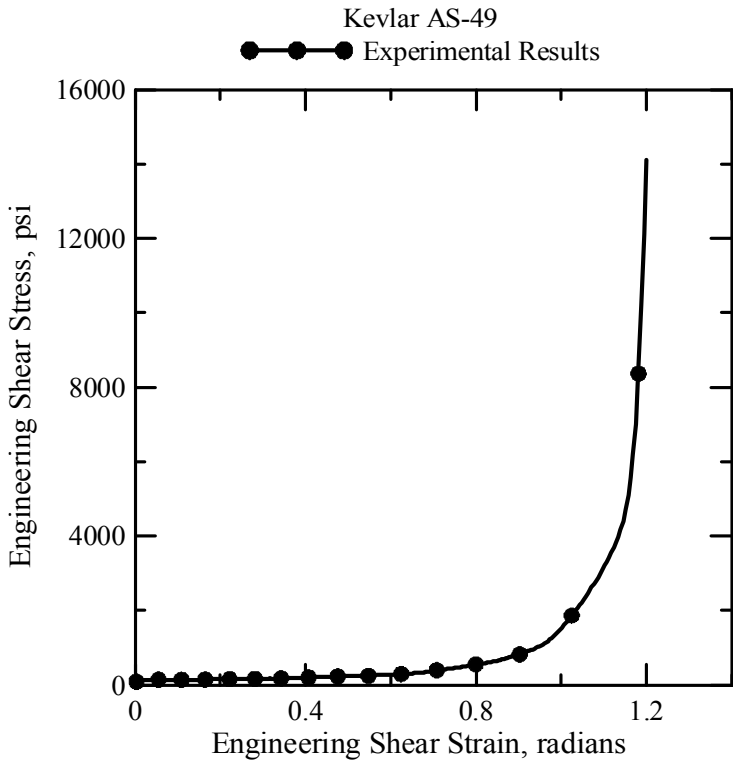

Figure 26. Picture Frame Shear Test Results

The results show that the shear resistance increases with an increase in shear strain. At low shear strains, the fabric has little resistance to shear deformation. However, at higher shear strains, the fabric's resistance to shear deformation increases. The yarns rotate and the warp and fill directions are no longer orthogonal. At some point, there is a very rapid increase in the shear stress value. This is caused by the re-orientation and packing of the fabric yarns as the shear strain increases. Initial FE simulations, discussed in section 2.2.6, were run using shear modulus values based on these results. The simulations were highly inaccurate as the fabric experienced large local deformations around the contact area that were not observed in the experimental tests. A further examination of the fabric's deformation during the picture frame tests revealed that the fabric wrinkled at the edges during the initial stages of loading and experienced excessive buckling during the final stages of loading. Images of these occurrences are shown in figures 27 and 28. With the shear angle at about 25°-30°, the sudden increase in the shear stress value coincides with the formation of wrinkles at the edges.

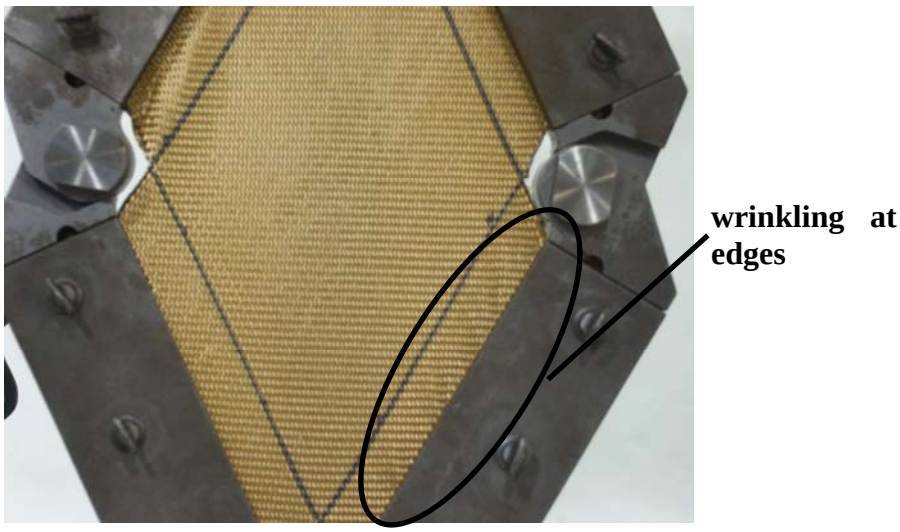

Figure 27. Fabric Wrinkling at Edges During Picture Frame Test

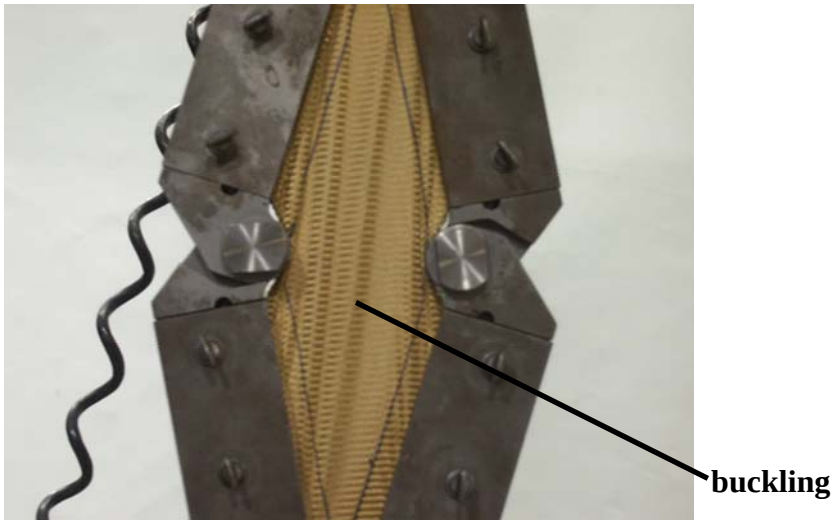

Figure 28. Fabric Buckling During Picture Frame Test

Since the test results were overpredicting the actual shear deformation of the fabric, a simple approach was used to rectify the behavior with more tests planned to study the problem in greater detail. It was assumed the actual shear strain of the fabric was one-half the values reported by the picture frame test. With this correction, the fabric's shear modulus was assumed to be twice the picture frame test values, and the shear stress-strain curve includes only the behavior captured by yarn re-orientation. Using the corrected values, more accurate fabric deformations were found in the simulations. In the material model, a piecewise linear approximation of the corrected results was used to model the nonlinear response, as shown in figure 29.

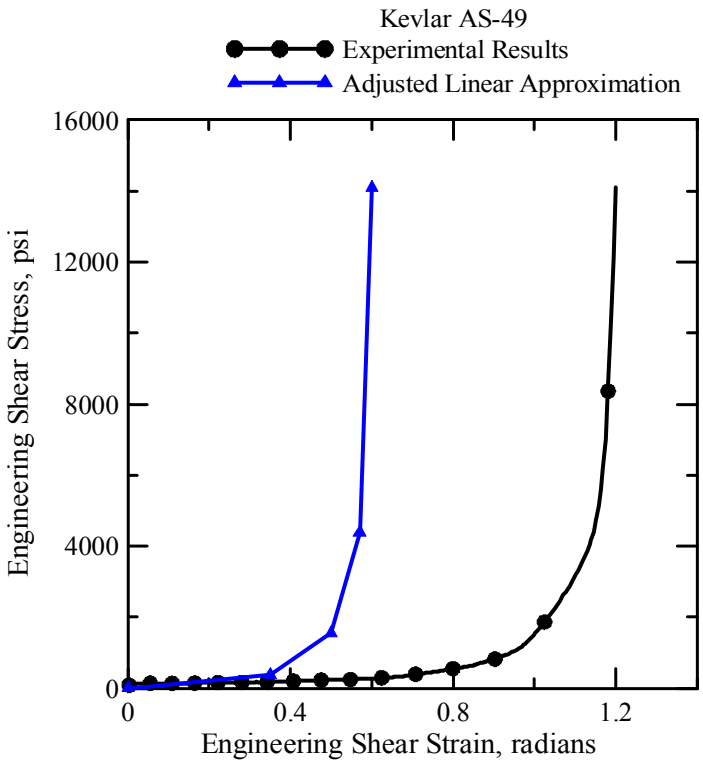

Figure 29. Picture Frame Shear Test Results With Corrected Linear Approximation

The fabric was assumed to unload and reload along the same path. It should be noted that the picture frame tests were conducted under quasi-static conditions. Hence, neither strain rate-dependent data is generated nor does the developed constitutive model use strain rate-dependent data.

The actual shear modulus values at various shear strain values used in the material model are as follows.

For:	$\gamma_{12} < 0.35$	$G_{12} = 1(10^3)$ psi
	$0.35 < \gamma_{12} < 0.50$	$G_{12} = 8(10^3)$ psi
	$0.50 < \gamma_{12} < 0.57$	$G_{12} = 40(10^3)$ psi
	$\gamma_{12} > 0.57$	$G_{12} = 300(10^3)$ psi

Again, the shear modulus values above are based on the assumption that the fabric is 0.011″ thick. The shear strain values are expressed in radians. The shear stress increment was computed based on equation 5 and is shown below in equation 18.

$$\Delta\sigma_{12} = 2\Delta\varepsilon_{12}G_{12} = \Delta\gamma_{12}G_{12} \tag{18}$$

2.2.6 Determination of Additional Shear Modulus Values (G_{31} and G_{23}).

Kevlar 49 does not experience noticeable shear deformations in the out of plane directions of the fabric (in the 31 and 23 directions). Hence, a conservatively low value of 50,000 psi was taken as the shear modulus for G_{31} and G_{23} and the value proved to be adequate for FE simulation purposes.

2.2.7 Determination of Fabric Density.

The actual measured density of Kevlar 49 is 0.052 $\frac{lbf}{in^3}$, or 1.44 $\frac{g}{cm^3}$. Since the material model's properties were computed based on the measured fabric thickness of 0.011″, the actual density needed to be adjusted in the model. This was done by first measuring the mass of a 1″ by 1″ fabric sample, which was approximately 0.144 g. To obtain the mass density of the fabric in the model, the actual mass was divided by the volume of material assumed in the model, or (1″)(1″)(0.011″) = 0.011 in^3. Thus, the fabric density used in the material model was 0.80 $\frac{g}{cm_3}$, or $7.48(10^{-5})$ $\frac{lbf - \sec^2}{in^4}$.

2.3 VALIDATION OF MATERIAL MODEL WITH NUMERICAL RESULTS.

2.3.1 Explicit FE Code for Material Model Implementation.

There are several commercial explicit FE codes, such as LS-DYNA, ABAQUS/Explicit, and PAM-CRASH. Since most engine manufacturers currently use LS-DYNA for simulations involving engine containment systems, in this research work LS-DYNA was also used.

While LS-DYNA supports several different material constitutive models, it does not have a material model suitable for modeling dry fabrics. In situations such as this, LS-DYNA allows users to integrate their own material constitutive behavior through a user-defined material (UMAT) definition, preferably through a FORTRAN® subroutine. For each element that belongs to the user-defined material, LS-DYNA calls the UMAT subroutine at each integration point and passes information, including the material parameters defined by the user at the start of the analysis, the current strain increment, the previous total stress, any history variables defined in the UMAT, the current time increment, the element type ("shell," "brick," etc.), the current analysis time, and a failure indicator. Other information can also be obtained; however, it requires collaboration with the LSTC software developers. The stress and strain values are rotated to the local material coordinate system before being passed to the UMAT. In turn, the statements in UMAT must be configured to compute the stress increment, update any history variables that may be needed in the following time step, and update the element failure indicator if the element meets one or more failure criteria. A chart showing the inputs and outputs of the UMAT subroutine are shown in figure 30.

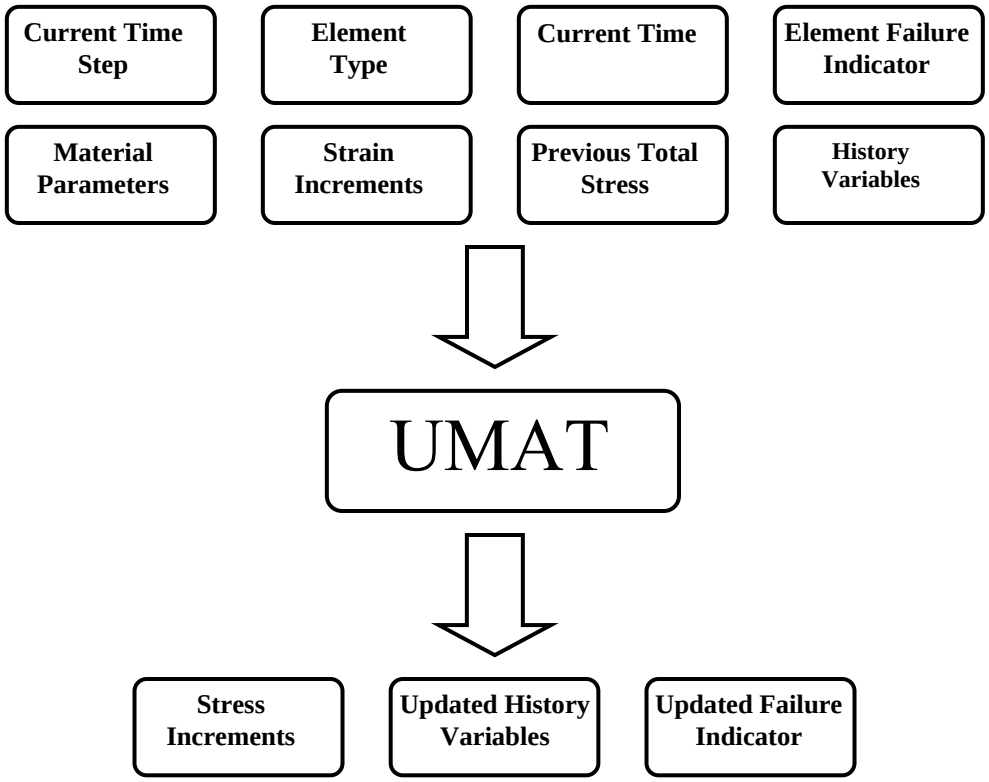

Figure 30. Flow Chart for Inputs and Outputs of UMAT Subroutine

Details of the single-element and constitutive model validation tests that ASU has performed with the developed UMAT can be found in reference 42.

2.3.2 The NASA-GRC Experimental Ballistic Tests.

Experimental ballistic tests involving 1420 D 17x17 weave Kevlar 49 were performed at NASA-GRC [44 and 45]. In the tests, a 40″ diameter steel ring with a 10″ opening was wrapped with one or more layers of Kevlar 49. The fabric was wrapped under a small amount of tension so that there was no slack between fabric layers and at the ring opening. The ring was 1″ thick and 10.5″ wide, and the fabric was 10″ wide. Figure 31 shows the ballistic test setup with the steel ring and fabric wrap. A steel projectile was launched through a gas gun and impacted the fabric at the opening of the ring. The steel ring was tilted at 15° so that the projectile was clear to impact the fabric only. Multiple tests were performed varying the number of fabric layers, projectile velocity, and projectile orientation. Two different projectiles were used in the tests—one was a shorter, thicker projectile with overall dimensions 4.0″ by 2.0″ by 0.3125″ and the other was a longer, thinner projectile with overall dimensions 7.0″ by 1.5″ by 0.235″. Both projectiles had a front edge that was machined to full radius to remove any sharp corners. Figure 32 shows both steel projectiles used in the tests.

Figure 31. The NASA-GRC Ballistic Test Steel Ring With Kevlar 49 Wrap

Figure 32. The NASA-GRC Ballistic Test Steel Projectiles

The projectile's velocity before impact and after impact and its orientation were measured during each test using high-speed cameras. The cameras tracked the position of various points on the projectile to determine its velocity and related the position to a fixed coordinate system to determine its orientation. Figures 33 and 34 show the local coordinate system of the projectile and the fixed or global coordinate system for a 0° and a non-0° test case, respectively.

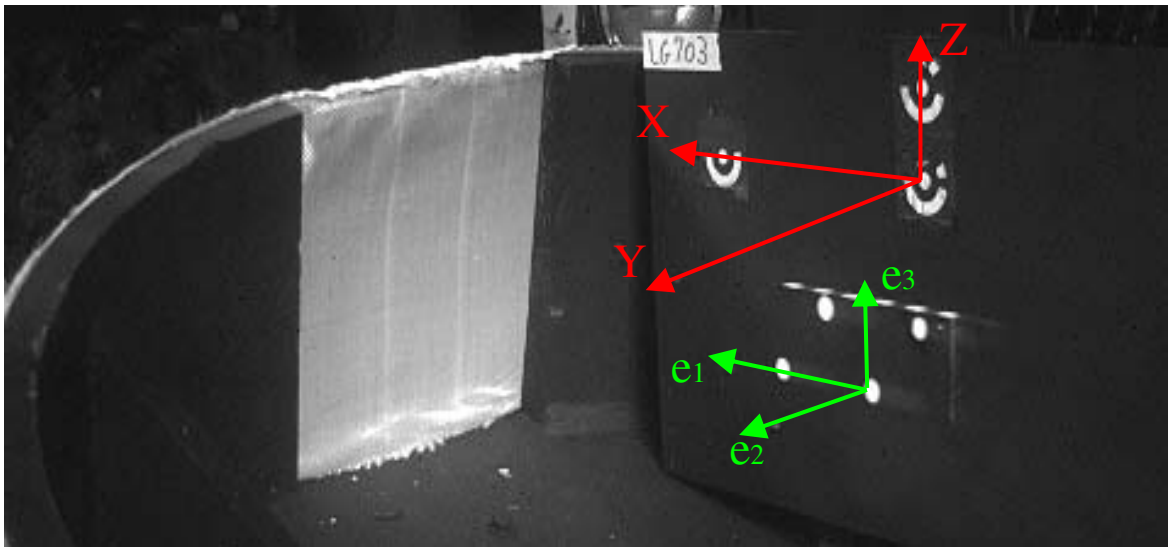

Figure 33. The NASA-GRC Ballistic Test Showing Global Coordinate System (X-Y-Z) and Local Projectile Coordinate System for a 0° Projectile Orientation

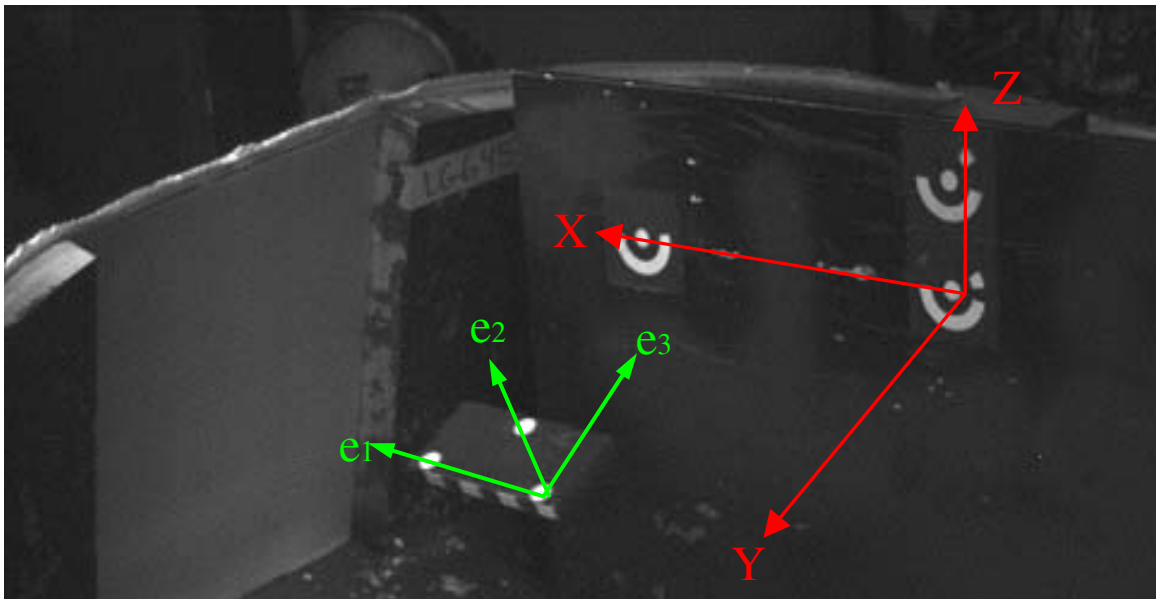

Figure 34. The NASA-GRC Ballistic Test Showing Global Coordinate System (X-Y-Z) and Local Projectile Coordinate System for a Non-0° Projectile Orientation

In the figures, the local coordinate system of the projectile is defined as "e" and the fixed coordinate system is shown. The orientation of the projectile was reported as Euler angles corresponding to roll, pitch, and yaw of the projectile. The roll, pitch, and yaw angles are defined as the rotation about the e_1 axis, e_2 axis, and e_3 axis, respectively, as shown in figure 35, and the local coordinate system is shown at the center of the projectile. A right-hand rule is used to define positive and negative rotations. The order of rotation is important in this case because each angle is reported with respect to the projectile's local coordinate system. With each

rotation, the local coordinate system changes and the next rotation are with respect to the new local coordinate system.

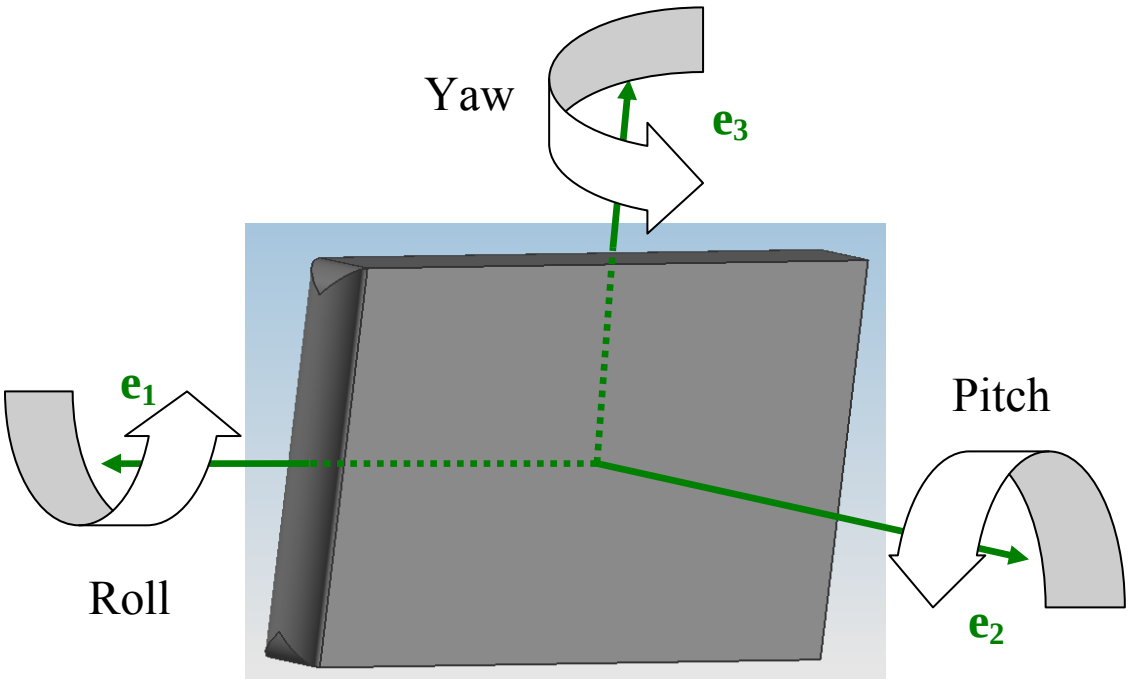

Figure 35. Roll, Pitch, and Yaw Angles of the Projectile

Two phases of tests were conducted. In the first phase, 14 tests were conducted with Kevlar 49 using only the shorter, thicker projectile at a 0° roll, 0° pitch, and 0° yaw orientation while the number of fabric layers and projectile velocity were varied. It should be noted that for these 0° orientation cases, the projectile actually impacted the fabric at a 15° pitch due to the tilt in the ring. Also, the actual projectile impact angle may have been slightly different than the desired angle due to the impact test limitations. The actual angle was measured and recorded. In the second phase, 16 additional tests were conducted varying each parameter: the projectile geometry, projectile orientation, number of fabric layers, and projectile velocity. Of those 16 tests, 12 were validated for accuracy of the reported orientation angles. Table 1 shows the fabric absorbed energy results for the 26 runs for both the first and second phases of testing. The test case number (LGXXX) was designated by NASA-GRC. LG403–LG449 are experimental data from Phase I, and LG594 and LG609-LG689 are from Phase II.

The absorbed energy of the fabric was computed as kinetic energy of the projectile before impact minus the kinetic energy of the projectile after impact, or as

$$E_{abs} = \left(\frac{1}{2}\right) m v_i^2 - \left(\frac{1}{2}\right) m v_f^2 \tag{19}$$

The initial and final velocities are reported with the simulation results in the following section.

Table 1. The NASA-GRC Ballistic Test Experimental Results

Run	Test	Layers	Projectile Orientation			Experimental Results		
			Roll (deg)	Pitch (deg)	Yaw (deg)	Projectile Mass (g)	Absorbed Energy	
							(ft-lb)	(%)
1	LG403	4	0	0	0	318.4	999.43	11
2	LG404	8	0	0	0	317.8	1409.82	16
3	LG405	24	0	0	0	319	6149.76	70
4	LG409	8	0	0	0	316	1506.23	18
5	LG410	4	0	0	0	316.4	885.36	10
6	LG411	24	0	0	0	314.8	6620.27	78
7	LG424	8	0	0	0	320.9	1536.88	20
8	LG427	24	0	0	0	317.9	5113.28	56
9	LG429	16	0	0	0	316.2	3484.30	38
10	LG432	16	0	0	0	320	4168.73	47
11	LG433	1	0	0	0	316.7	188.89	11
12	LG434	1	0	0	0	315.9	185.15	12
13	LG444	2	0	0	0	316.4	473.95	36
14	LG449	2	0	0	0	316.2	443.14	34
15	LG609	8	37.35	0.87	1.63	304.87	1604.04	18
16	LG610	8	25.30	0.70	11.93	306.82	1399.22	17
17	LG611	8	30.89	-1.74	-10.78	321.2	2017.97	22
18	LG612	8	22.78	-3.74	-0.53	321.01	1429.43	16
19	LG618	8	-47.14	6.31	51.55	305.5	4587.67	58
20	LG620	8	-37.79	0.18	55.07	316.2	5001.02	58
21	LG655	32	-32.46	1.29	2.57	313.05	6337.66	46
22	LG656	32	8.98	-2.31	-10.07	321.57	7883.02	76
23	LG657	32	-22.16	9.73	1.42	325.35	7673.78	100
24	LG689	8	-12.83	-1.28	49.72	323.24	4143.62	47
25	LG692	8	38.24	2.31	41.45	315.95	4554.18	54
26	LG594	8	27.00	6.60	47.80	306.77	5017.06	67

2.3.3 Simulation of NASA-GRC Ballistic Tests.

To validate the developed ASU material model, simulations of the NASA-GRC ballistic tests were performed using LS-DYNA. The simulations were run using the single-precision LS-DYNA version 971 (Revision 7600.398) with version date 8-17-2006. The FORTRAN compiler

was Intel® Version 9, and the computer platform was Windows® XP (SP 2). Details of the FE models are discussed in the following sections.

2.3.3.1 The FE Model.

Shell elements were used to represent the fabric, and solid elements were used to represent the steel ring and steel projectiles. The mesh density that was used to describe the steel ring and fabric were chosen based on investigations that were done by other research organizations with collaboration from the FAA and engine manufacturers [27, 29, and 45]. The fabric was modeled with a uniform mesh containing 0.25″ shell elements. The steel ring was modeled with 0.25″ by 0.25″ by 1.0″ hexagonal elements (1.0″ through the ring thickness) since the steel ring is not of interest with respect to the FE analysis results. One layer of shell elements was used to represent the fabric irrespective of the actual number of fabric layers. Thus for an eight-layer test case, the shell element thickness was taken as the thickness of one fabric layer multiplied by 8, or 0.011″ x 8 = 0.088″. There were two motivations for this selection. The overriding concern was the total simulation time. In addition, when the study was started, LS-DYNA had difficulty handling all the contact surfaces between multiple fabric layers. With this methodology, the friction between the fabric layers is not captured.

In the model, the center of the shell elements was placed at a distance of one-half the shell element thickness away from the steel ring, thereby facilitating contact between the shell elements and the steel ring at the start of the analysis. Figure 36 shows the FE mesh of the steel ring and fabric.

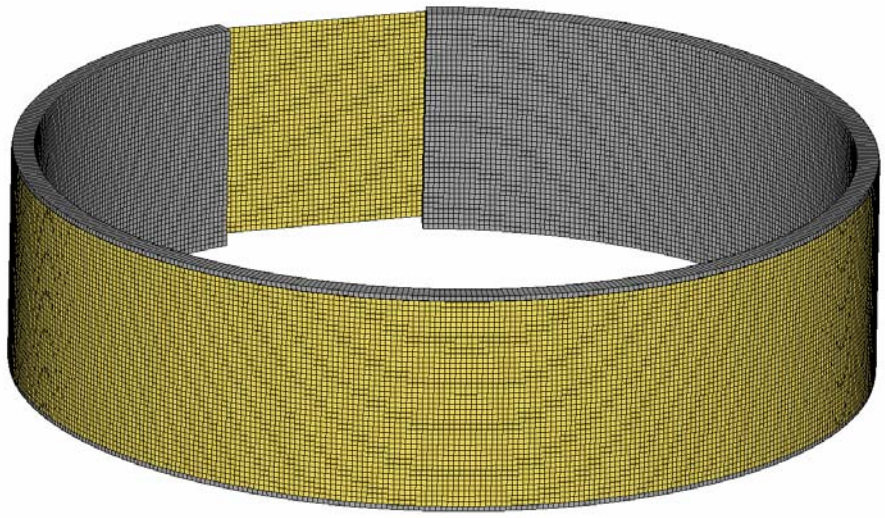

Figure 36. The FE Mesh of the Steel Ring and Fabric

The old (shorter and thicker) projectile was modeled with 0.15″ uniform tetrahedral elements for the tip and 0.2″ by 0.15625″ by 0.2023″ hexahedral elements for the body. The new (longer and thinner) projectile was modeled with 0.10″ uniform tetrahedral elements for the tip and 0.15″ by 0.1175″ by 0.1496″ hexahedral elements for the body. Figure 37 shows the FE mesh for both projectiles.

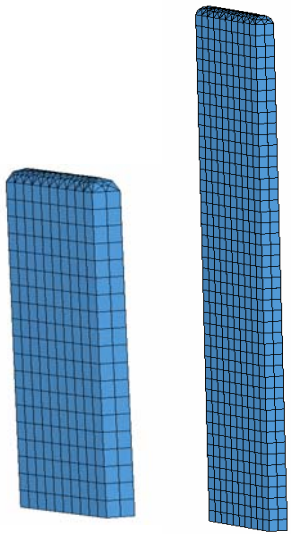

Figure 37. The FE Mesh for Projectiles Used in the NASA-GRC Ballistic Test

The model global coordinate system directions coincided with the global coordinate system used in the experimental tests, as shown in figure 38.

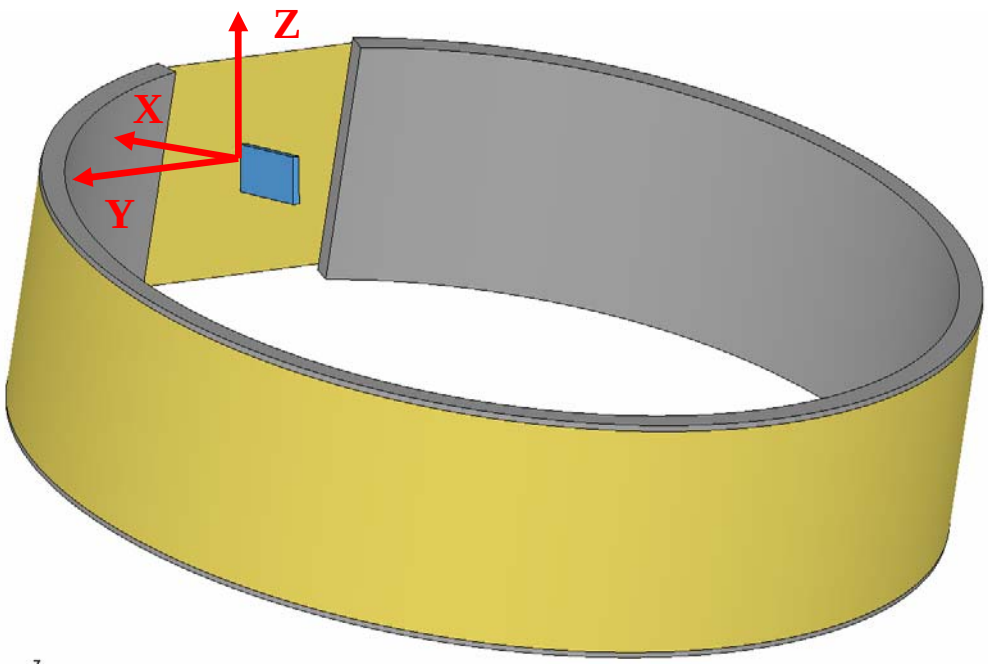

Figure 38. Global Coordinate System Used in Simulations

Thus, the ring and fabric were rotated at 15° from the X-Y plane, and the projectile moved along the X direction. Since the origin of the projectile's local coordinate system was not recorded for each test case, the center of the projectile was assumed to be the origin for orientating the projectile in the model. This was an adequate assumption as the choice for the origin of the local

coordinate system does not affect the final angular orientation. To orient the projectile correctly, the projectile's initial local coordinate system had to be parallel to the global coordinate system. The projectile was then rotated using its reported roll, pitch, and yaw angles from the test. A general example of how a 45° roll, 0° pitch, and 45° yaw projectile would be orientated is shown in figure 39. The orientation of the projectile for each of the 12 test cases was qualitatively compared to the experimental test and was determined to be acceptable.

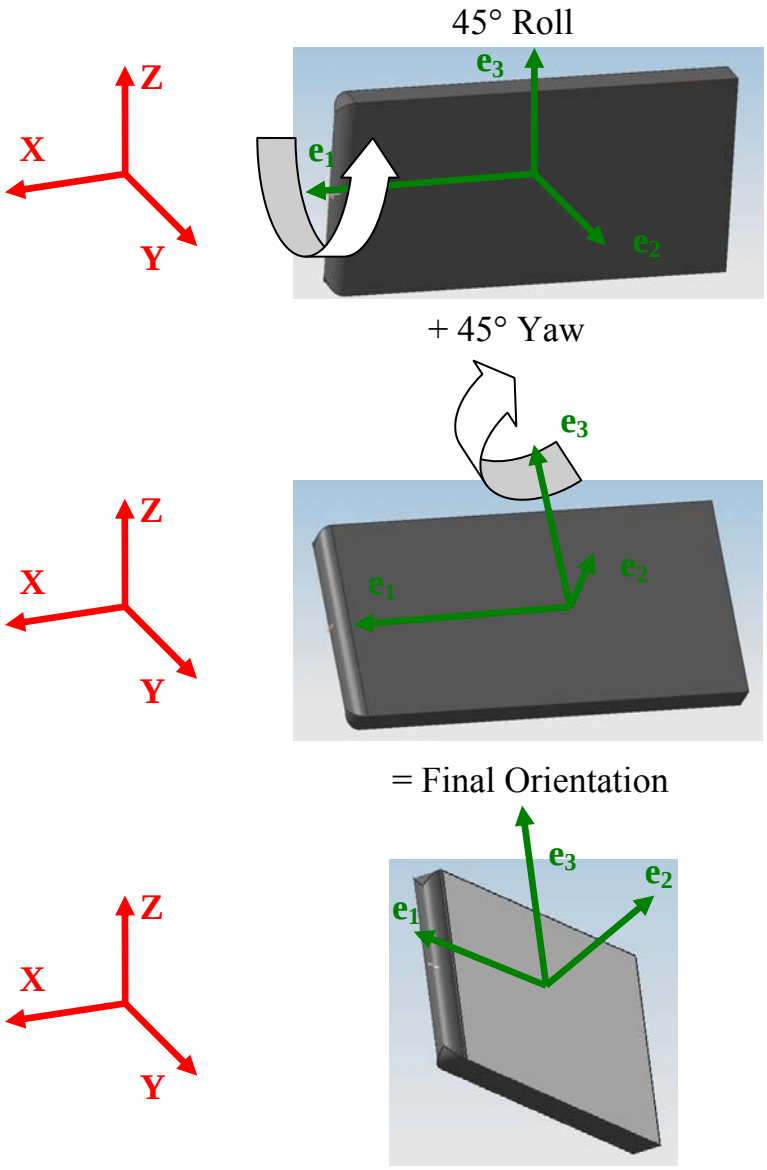

Figure 39. Example of 45° Roll, 0° Pitch, and 45° Yaw Projectile Orientation

2.3.3.2 Analysis Parameters.

LS-DYNA has many options for contact definition, various contact parameters, shell element theory, various shell element parameters, and hourglass parameters.

The contact definition used was the *CONTACT_AUTOMATIC_SURFACE_TO_SURFACE option. The *CONTACT_ERODING_SINGLE_SURFACE option was also investigated but the difference in the results was not significant. Since the fabric and the steel ring/projectile have large differences in their respective stiffness and mesh densities, the pinball segment-based contact constraint option was used as recommended by the LS-DYNA Keyword User's Manual [46]. With this contact option, the contact stiffness is determined based on the time step and nodal masses. Also, segment versus segment contact is checked rather than node versus segment. After penetrating segments are detected, LS-DYNA designates one of the segments as the master segment and penalty forces are applied normal to that segment.

Since there were no experimental friction tests conducted using Kevlar 49 and steel, the static and dynamic coefficients of friction had to be assumed. Experimental friction tests of Kevlar 49 showed that the coefficient of static and dynamic friction for fabric on fabric was approximately 0.20 [2]. Using this value as a guide, a value of 0.10 was assumed for both the static and dynamic coefficients of friction between the steel ring and the fabric. A viscous damping coefficient of 2% of critical was also assumed. Other values for this parameter were not investigated. All other contact parameters were taken as the LS-DYNA default values. The contact card specifying the contact between the projectile and fabric is shown in figure 40. The contact definition between the steel ring and the fabric was similar. All blank values led to default values being used in the analysis.

```
$
$$$$$$$$$$$$$$$$$$$$$$$$$$$$$$$$$$$$$$$$$$$$$$$$$$$$$$$$$$$$$$$$$$$$$$$$$$$$$$$$$$
$
$             PROJECTILE TO FABRIC CONTACT DEFINITION
$
$$$$$$$$$$$$$$$$$$$$$$$$$$$$$$$$$$$$$$$$$$$$$$$$$$$$$$$$$$$$$$$$$$$$$$$$$$$$$$$$$$
$
*CONTACT_AUTOMATIC_SURFACE_TO_SURFACE
$#    ssid      msid     sstyp     mstyp    sboxid    mboxid       spr       mpr
         1        11         3         3
$#      fs        fd        dc        vc       vdc    penchk        bt        dt
     0.100     0.100                         2.000
$#     sfs       sfm       sst       mst      sfst      sfmt       fsf       vsf

$#    soft    sofscl    lcidab    maxpar     sbopt     depth     bsort    frcfrq
         2
$#  penmax    thkopt    shlthk     snlog      isym     i2d3d    sldthk    sldstf
                   0
$#    igap    ignore
```

Figure 40. Contact Card Parameters Used in Each Analysis

The *CONTROL_CONTACT card used for each analysis is shown in figure 41. The SHLTHK parameter specifies that the shell thickness is considered with the contact algorithm.

```
*CONTROL_CONTACT
$    slsfac    RWPNAL    islchk    SHLTHK    penopt    thkcng     ORIEN
                0.000                    1
$    USRSTR    USRFRC     nsbcs    interm     xpene     ssthk      ecdt   tiedprj

$     sfric     dfric       edc       vfc        th     th_sf    pen_sf

$    ignore    frceng   skiprwg    outseg   spotstp   spotdel   spothin
```

Figure 41. Contact Control Card Parameters Used in Each Analysis

The Belytschko-Tsay shell element formulation theory was used with one-point Gaussian integration. The shell normal update option was used and the shell element thickness was kept constant during the analysis. All other shell parameters were taken as the default values.

Hourglass properties were used for the fabric and steel elements for each analysis. For the fabric material, the Flanagan-Belytschko stiffness form was used with an hourglass coefficient of 0.10. For the steel material, the Flanagan-Belytschko viscous form was used with an hourglass coefficient of 0.0. The hourglass card for the fabric and steel is shown in figures 42 and 43, respectively.

```
*HOURGLASS
$     HGID      IHQ         QM       IBQ        Q1        Q2        QB        QW
         1        4        0.1         0       0.0       0.0       0.1       0.1
```

Figure 42. Hourglass Card Used for Fabric Material

```
*HOURGLASS
$     HGID      IHQ         QM       IBQ        Q1        Q2        QB        QW
        11        2        0.0         0       0.0       0.0       0.0       0.0
```

Figure 43. Hourglass Card Used for Steel Material

For each analysis, the time step factor used was 0.75. Thus, the actual time step was 75% of the value computed by LS-DYNA. Using this value, no unstable analyses occurred.

Second-order stress updates and invariant node numbering of shell elements were also used as specified in the *CONTROL_ACCURACY card in each analysis as recommended by LS-DYNA for high-velocity impact problems.

2.3.3.3 Simulation Absorbed Energy Results With Comparison to Experimental Results.

Table 2 shows a comparison between the absorbed energy of the fabric for each experimental test case and its corresponding LS-DYNA simulation result. For the rest of this report, the experimental values are used as baseline reference values. The percent difference (% Diff.) values shown in the table were computed as

$$\% \text{ Diff.} = (\text{Experimental Absorbed Energy \%}) - (\text{Simulated Absorbed Energy \%}) \quad (20)$$

Hence, a positive % Diff. corresponds to the FE simulation underpredicting the absorbed energy and a negative % Diff. corresponds to the FE simulation overpredicting the absorbed energy.

Table 2. Comparison of Absorbed Energy (Experimental Ballistic Tests vs FE Simulations)

Run	Test	Fabric Layers	Experimental							Simulation							% Difference
			Projectile Mass (g)	Before Impact		After Impact		Absorbed Energy		Projectile Mass (g)	Before Impact		After Impact		Absorbed Energy		
				Velocity (ft/sec)	Energy (ft-lb)	Velocity (ft/sec)	Energy (ft-lb)	(ft-lb)	(%)		Velocity (ft/sec)	Energy (ft-lb)	Velocity (ft/sec)	Energy (ft-lb)	(ft-lb)	(%)	
1	LG403	4	318.4	898.95	8,815.57	846.46	7,816.13	999.43	11	315.82	898.92	8,741.42	867.03	8,127.53	613.89	7	4
2	LG404	8	317.8	895.67	8,734.86	820.21	7,325.04	1,409.82	16	315.85	895.67	8,676.67	816.62	7,211.47	1,465.20	17	-1
3	LG405	24	319	898.95	8,832.18	495.41	2,682.42	6,149.76	70	315.82	898.92	8,741.42	0.00	0.00	8,741.42	100	-30
4	LG409	8	316	889.11	8,558.63	807.09	7,052.40	1,506.23	18	315.82	889.08	8,548.02	805.90	7,023.00	1,525.02	18	0
5	LG410	4	316.4	912.07	9,017.76	866.14	8,132.40	885.36	10	315.82	912.08	8,986.13	893.98	8,640.58	345.55	4	6
6	LG411	24	314.8	885.83	8,463.33	413.38	1,843.06	6,620.27	78	315.82	885.83	8,490.76	0.00	0.00	8,490.76	100	-22
7	LG424	8	320.9	833.33	7,635.01	744.75	6,098.13	1,536.88	20	315.82	833.33	7,508.22	699.58	5,291.41	2,216.81	30	-9
8	LG427	24	317.9	915.35	9,125.80	606.96	4,012.52	5,113.28	56	315.82	915.33	9,051.95	588.22	3,745.16	5,306.79	59	-3
9	LG429	16	316.2	915.35	9,077.00	718.5	5,592.70	3,484.30	38	315.82	915.33	9,051.95	693.18	5,204.60	3,847.35	43	-4
10	LG432	16	320	895.67	8,795.33	649.61	4,626.59	4,168.73	47	315.82	895.67	8,676.67	703.98	5,360.81	3,315.86	38	9
11	LG433	1	316.7	390.42	1,653.93	367.45	1,465.04	188.89	11	315.82	390.42	1,648.00	331.42	1,187.74	460.26	28	-17
12	LG434	1	315.9	383.86	1,594.78	360.89	1,409.63	185.15	12	315.82	383.83	1,592.89	320.14	1,108.31	484.58	30	-19
13	LG444	2	316.4	347.77	1,311.07	277.89	837.12	473.95	36	315.82	347.75	1,307.48	136.64	204.33	1,103.15	84	-48
14	LG449	2	316.2	344.49	1,285.65	278.87	842.50	443.14	34	315.82	344.42	1,282.53	136.08	201.41	1,081.12	84	-50
15	LG609	8	304.87	913.72	8,720.61	825.42	7,116.57	1,604.04	18	313.71	913.75	8,975.41	864.44	8,026.58	948.83	11	8
16	LG610	8	306.82	888.09	8,290.94	809.69	6,891.71	1,399.22	17	313.73	888.08	8,475.58	827.34	7,353.74	1,121.84	13	4
17	LG611	8	321.2	905.68	9,026.74	798.05	7,008.77	2,017.97	22	315.81	905.67	8,870.58	846.22	7,745.03	1,125.55	13	10
18	LG612	8	321.01	898.25	8,873.99	822.73	7,444.56	1,429.43	16	315.82	898.25	8,724.67	817.88	7,233.05	1,491.62	17	-1
19	LG618	8	305.5	866.42	7,857.32	558.91	3,269.65	4,587.67	58	313.72	866.42	8,067.03	405.42	1,812.99	6,254.04	78	-19
20	LG620	8	316.2	893.83	8,655.21	580.78	3,654.19	5,001.02	58	313.73	893.83	8,587.42	669.08	4,827.84	3,759.58	44	14
21	LG655	32	313.05	1,131.72	13,737.18	830.6	7,399.52	6,337.66	46	315.81	1,131.67	13,845.25	1015.61	11,158.91	2,686.34	19	27
22	LG656	32	321.57	967.31	10,308.91	469.24	2,425.89	7,883.02	76	315.81	967.33	10,119.92	703.78	5,365.87	4,754.05	47	29
23	LG657	32	325.35	829.71	7,673.78	0	0.00	7,673.78	100	315.81	829.67	7,448.05	0.00	0.00	7,448.05	100	0
24	LG689	8	323.24	896.26	8,896.09	655.08	4,752.47	4,143.62	47	315.81	896.25	8,692.25	684.63	5,102.22	3,590.03	41	5
25	LG692	8	315.95	885.32	8,484.47	602.56	3,930.29	4,554.18	54	315.81	885.33	8,467.50	738.39	5,943.89	2,523.61	30	24
26	LG594	8	306.77	843.85	7,484.27	484.5	2,467.21	5,017.06	67	313.71	843.83	7,653.54	337.19	1,254.58	6,398.96	84	-17

Table 3 shows the statistical results computed from the table 2 data.

Table 3. Statistics for Absorbed Energy % Difference Between Simulations and Experiments

	Total Test Cases
Number	26
Average (%)	-3.8
Maximum (%)	29.5
Minimum (%)	-49.8
Standard deviation (%)	19.9

Overall, the simulations overpredict the absorbed energy by an average of 4%. The simulation that underpredicted the absorbed energy by the largest amount was test case LG656. This was a 32-fabric layer test case with a high projectile velocity relative to the other test cases. The simulation that overpredicted the absorbed energy by the largest value was test case LG449. This was a two-fabric layer test case with the lowest projectile velocity relative to the other test cases. Tables 4 through 7 show additional statistical data.

Table 4. Statistics for Absorbed Energy % Difference for Groups of Fabric Layers

	Number of Fabric Layers	
	8 or Less	Greater Than 8
Number	18	8
Average (%)	-6	1
Maximum (%)	24	29
Minimum (%)	-50	-30
Standard deviation (%)	20	21

Table 5. Statistics for Absorbed Energy % Difference for Groups of Projectile Velocity

	Projectile Velocity		
	300-400 ft/sec	800-900 ft/sec	900+ ft/sec
Number	4	15	7
Average (%)	-33	-3	10
Maximum (%)	-17	24	29
Minimum (%)	-50	-30	-4
Standard deviation (%)	18	14	13

Table 6. Statistics for Absorbed Energy % Difference for Simulations Which Over or Underpredicted the Experimental Results

	Simulations That Underpredicted Test Results	Simulations That Overpredicted Test Results
Number	11	14
Average (%)	13	-17
Maximum (%)	29	0
Minimum (%)	4	-50
Standard deviation (%)	10	16

Table 7. Statistics for Absorbed Energy % Difference for Groups With Similar Projectile Orientations

	0° Projectile	Non-0° Projectile
Number	14	12
Average (%)	-13	7
Maximum (%)	9	29
Minimum (%)	-50	-19
Standard deviation (%)	19	15

There appears to be a weak correlation between absorbed energy and number of fabric layers. On the other hand, there appears to be a noticeable trend involving test cases where the projectile velocity is relatively low or high. For the four test cases that had the lowest velocity projectiles (LG433, LG434, LG444, and LG449), the simulations overpredicted the absorbed energy by an average of 33%. For the seven test cases that had the highest velocity projectiles, the simulations underpredicted the absorbed energy by an average of 10%. The tables show that the simulations that underpredicted the absorbed energy of the fabric had much less scatter in the results compared to the simulations that overpredicted the absorbed energy of the fabric. There also appears to be somewhat less scatter in the comparison between test cases that had 0° projectile orientations and those that had non-0° projectile orientations. Also the non-0° projectile test cases underpredicted the absorbed energy of the fabric on average, while the 0° projectile test cases overpredicted the absorbed energy of the fabric on average. These statistics are likely skewed due to the results from the four low-speed 0° tests.

2.3.3.4 Deformation Comparison Between Simulation and Experiment.

Figures 44, 45, 46, and 47 show the deformation comparison between the simulation and the experiment for test cases LG612, LG620, LG689, and LG429, respectively. These are test cases where the absorbed energy from the simulation matched well with the experimental results.

Figures 48, 49, and 50 show the deformation comparison between the simulation and the experiment for test cases LG433, LG655, and LG405, respectively. These are the test cases in

which the absorbed energy showed the largest difference between the simulation and experimental results. In test cases LG433 and LG405, the simulation overpredicted the absorbed energy of the fabric by 17% and 30%, respectively. In test case LG655, the simulation underpredicted the absorbed energy of the fabric by 27%.

It appears that the material model captures the general deformed shape of the fabric quite well. However, for the test cases in which the absorbed energy from the simulation did not match well with the experiment, the fabric deformation was also not well captured. In the low-velocity test cases, the simulations overpredicted the deformation and the absorbed energy. In the high-velocity test cases, the simulations underpredicted the deformation and the absorbed energy of the fabric. This strong correlation between the quality of the absorbed energy and quality of the deformation pattern (or amount of deformation) was observed in all the test cases.

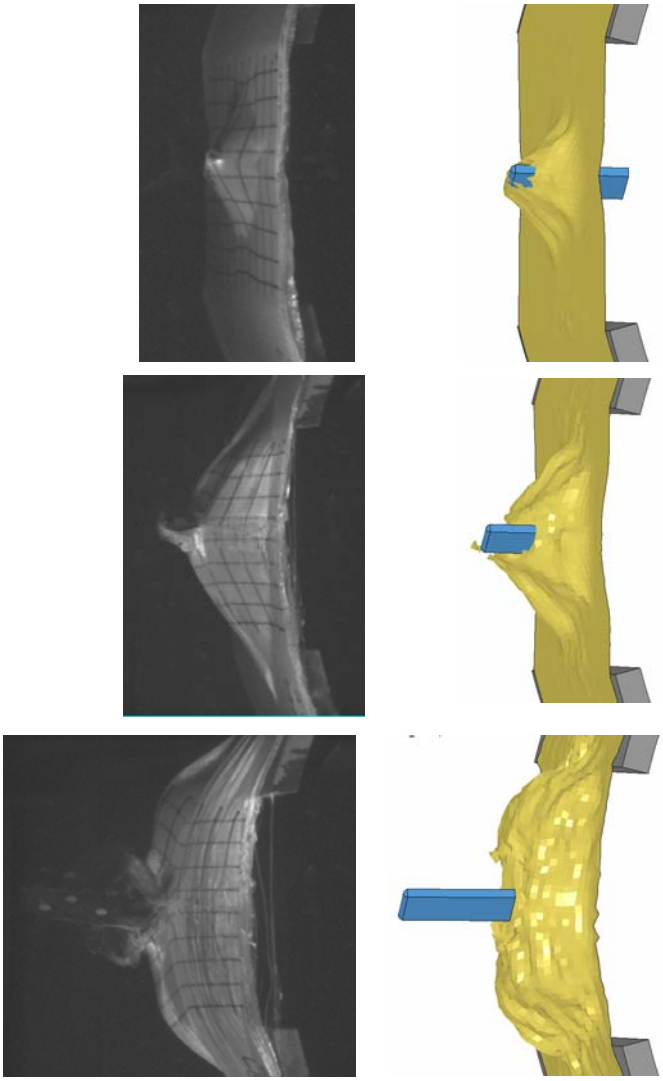

Figure 44. Deformation Comparison Between Experiment and Simulation for Test Case LG612 (Experimental Absorbed Energy = 16%, Simulated Absorbed Energy = 17%)

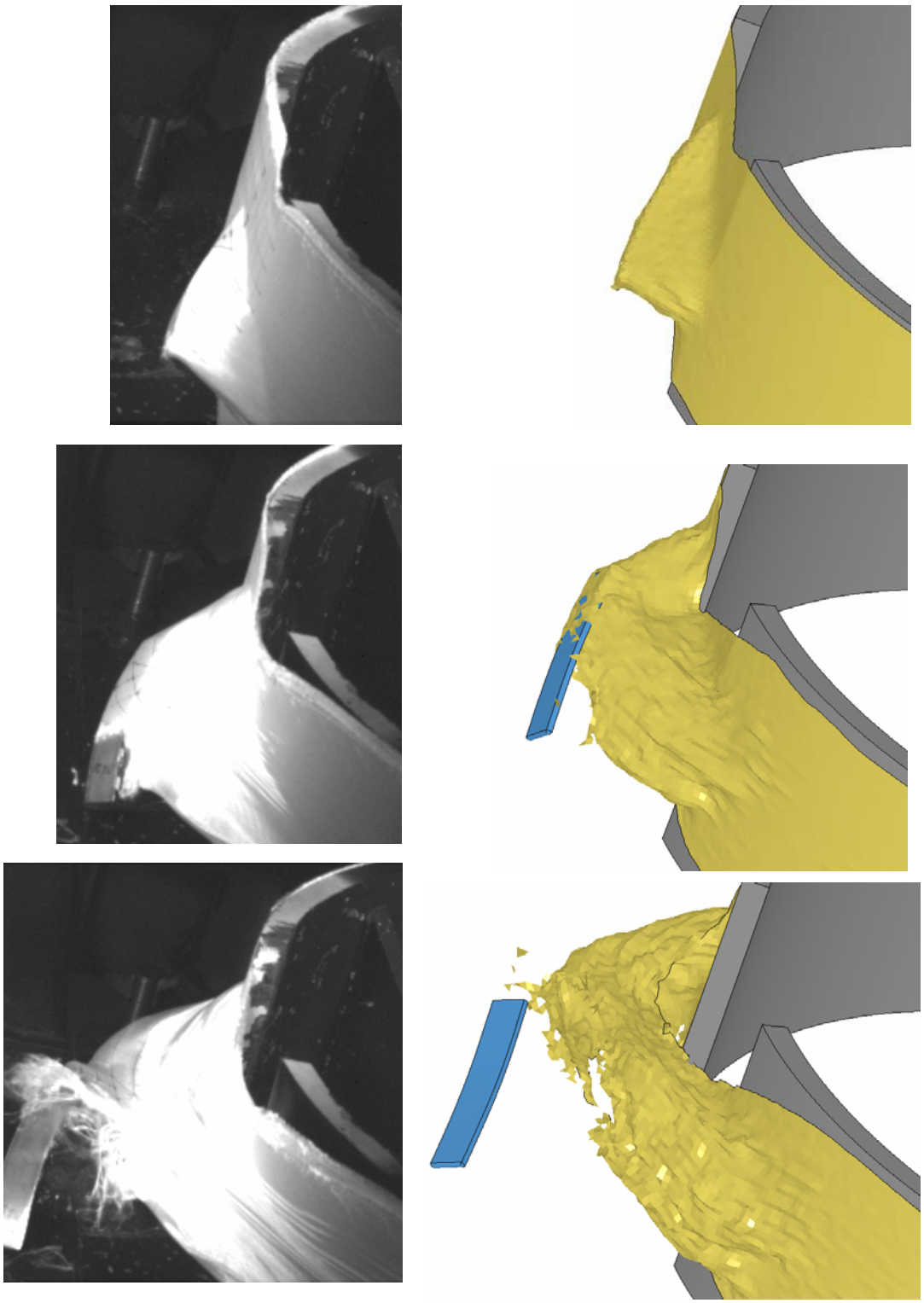

Figure 45. Deformation Comparison Between Experiment and Simulation for Test Case LG620 (Experimental Absorbed Energy = 58%, Simulated Absorbed Energy = 44%)

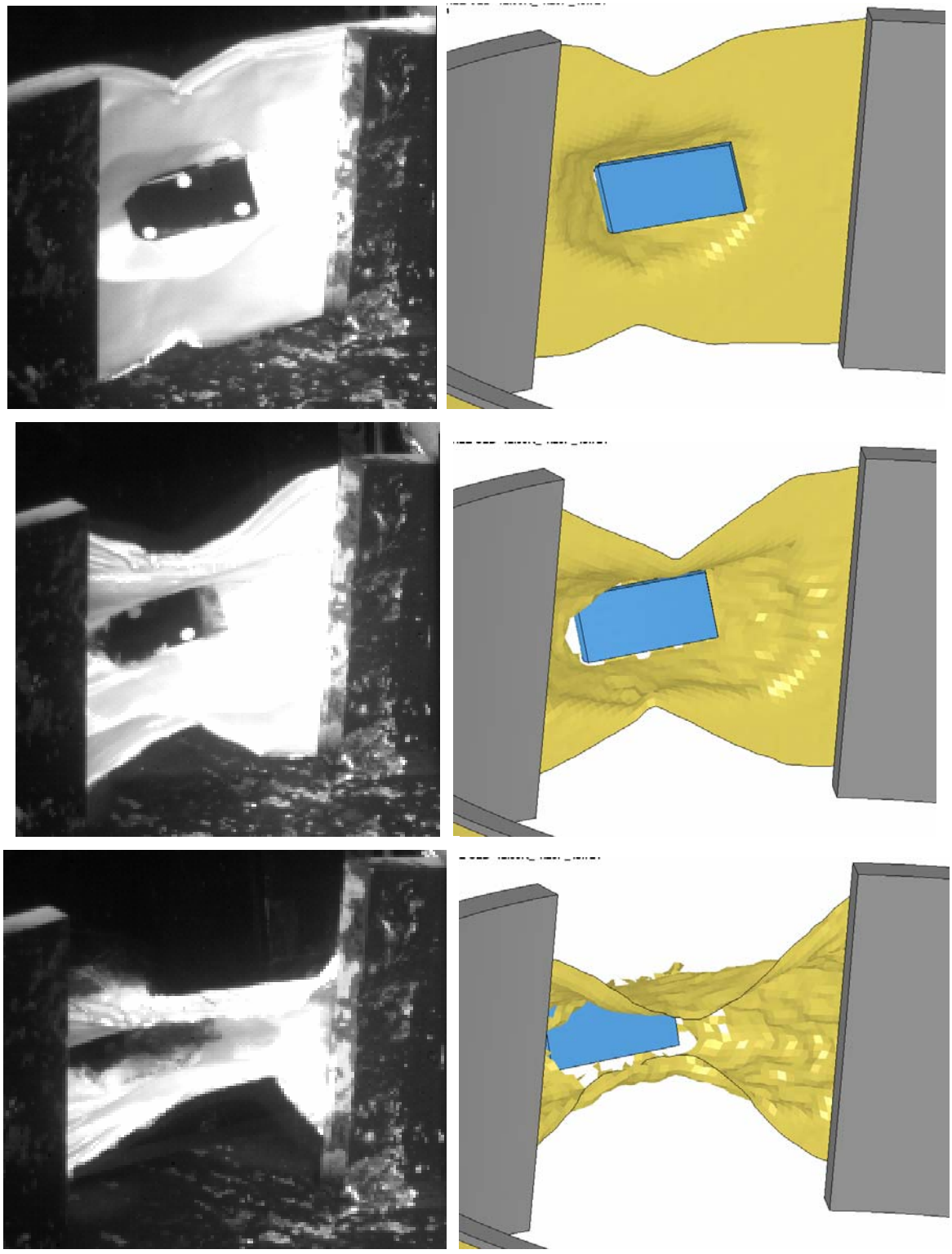

Figure 46. Deformation Comparison Between Experiment and Simulation for Test Case LG689 (Experimental Absorbed Energy = 47%, Simulated Absorbed Energy = 41%)

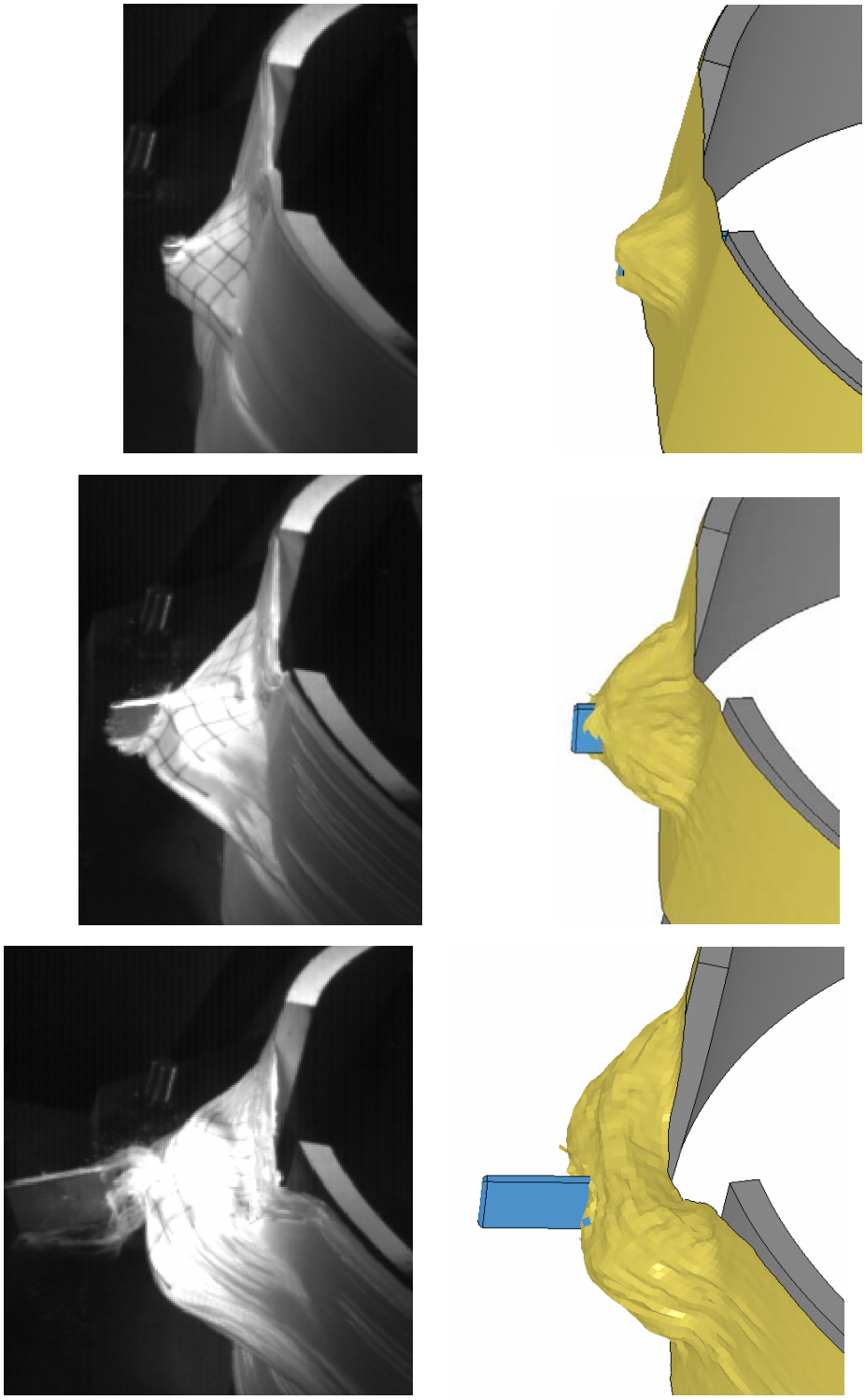

Figure 47. Deformation Comparison Between Experiment and Simulation for Test Case LG429 (Experimental Absorbed Energy = 38%, Simulated Absorbed Energy = 43%)

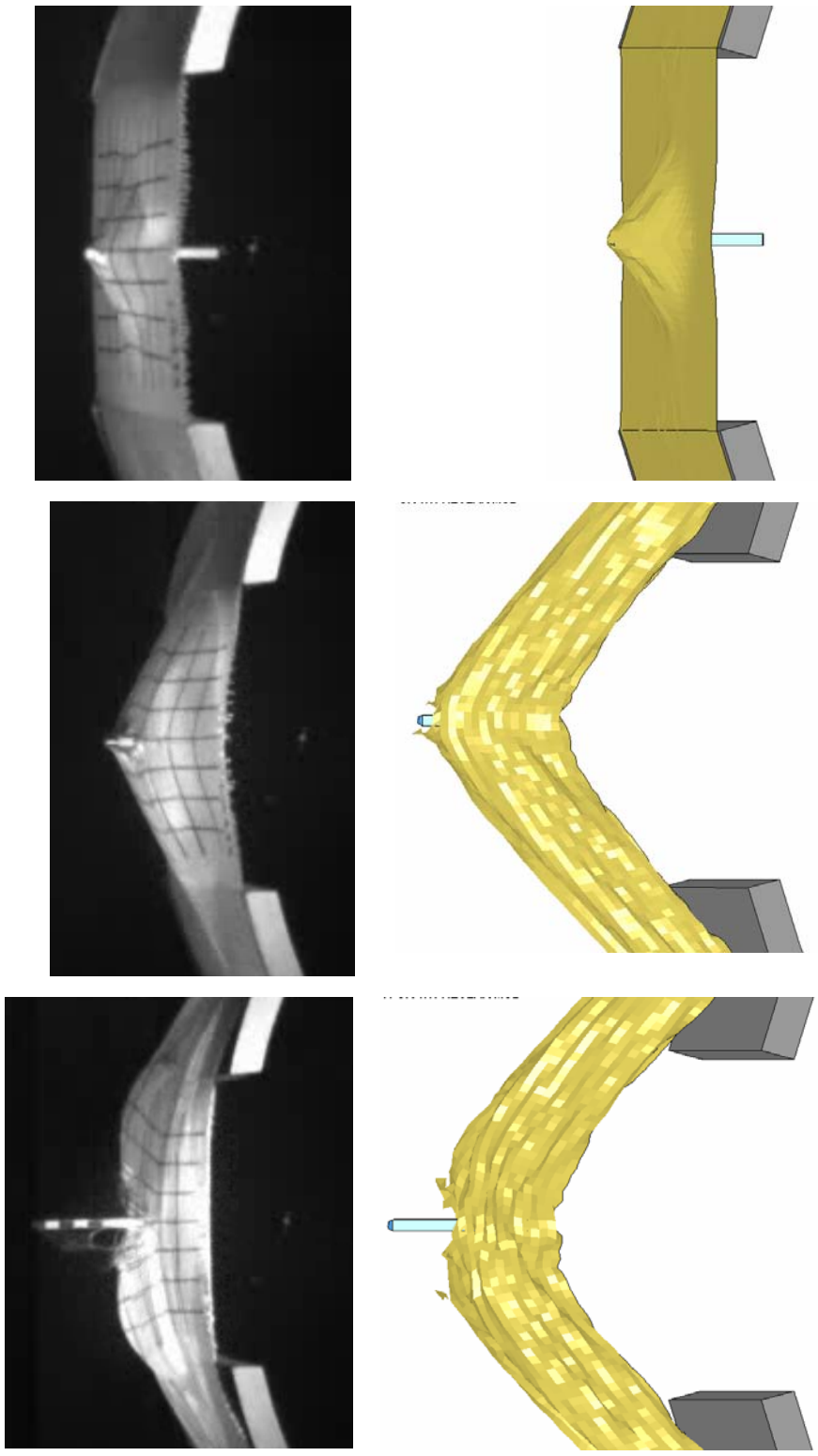

Figure 48. Deformation Comparison Between Experiment and Simulation for Test Case LG433 (Experimental Absorbed Energy = 11%, Simulated Absorbed Energy = 28%)

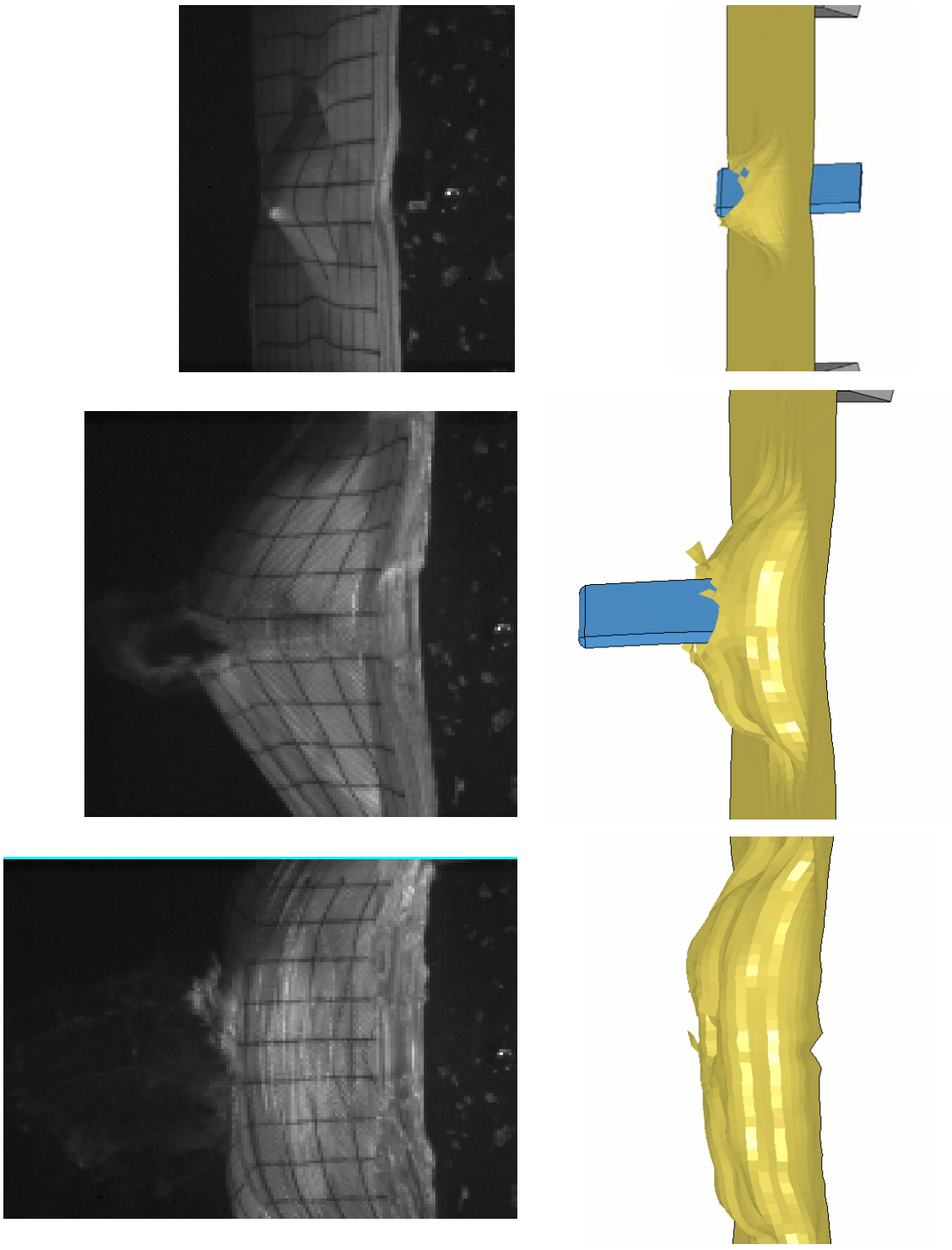

Figure 49. Deformation Comparison Between Experiment and Simulation for Test Case LG655 (Experimental Absorbed Energy = 46%, Simulated Absorbed Energy = 19%)

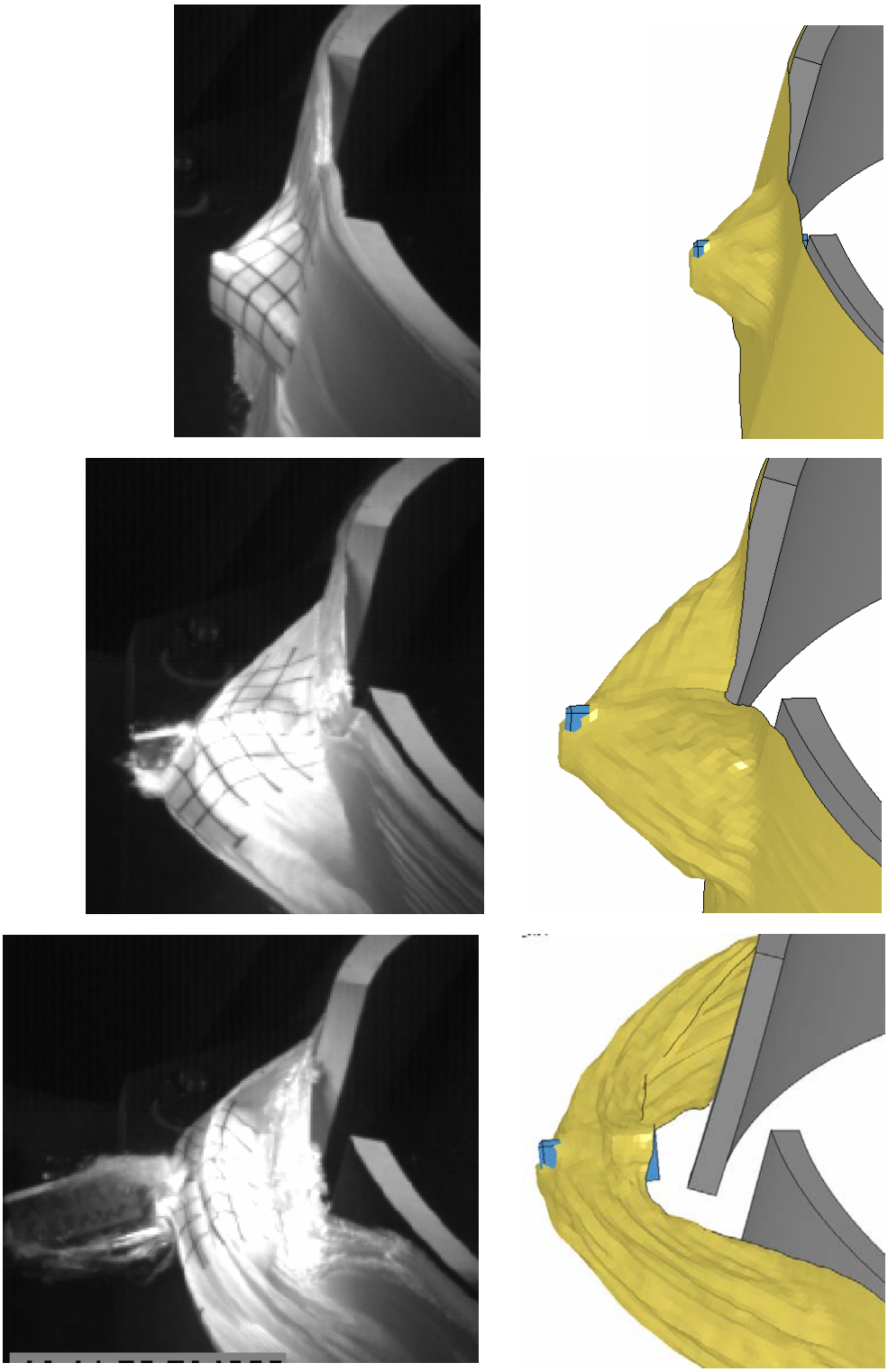

Figure 50. Deformation Comparison Between Experiment and Simulation for Test Case LG405 (Experimental Absorbed Energy = 70%, Simulated Absorbed Energy = 100%)

2.3.3.5 Warp and Fill Direction Stress-Strain Response in Simulation.

To better understand the developed constitutive model, the behavior of elements in the region of first failure was examined. Figures 51 and 52 show the warp and fill direction stress-strain response from the first failed element. Each data point represents a value from a specific time instance. For example, figure 51 shows the element in the simulation under continuous loading state with the stress in the element rising to about 55,000 psi. The element then unloads. It reloads with the final peak stress as 100,000 psi (ultimate stress value). The stress in the element (now in the post-peak region) then decreases, the element then unloads, reloads, enters the nonlinear stage of the softening region and finally fails when the strain reaches the limit value of 0.2. To show how the typical behavior of a failed element is much more complex than those encountered in simple tension tests, figure 51 also shows the stress-strain curve obtained experimentally from a simple tension test that shows the stress-strain behavior under quasi-static loading conditions. The behavior of another failed element in the fill direction is shown in figure 52. The element is in the loading state to about 80,000 psi, it unloads then reloads all the way up to 100,000 psi. Subsequently, the element enters the post-peak region followed by the softening region and failure.

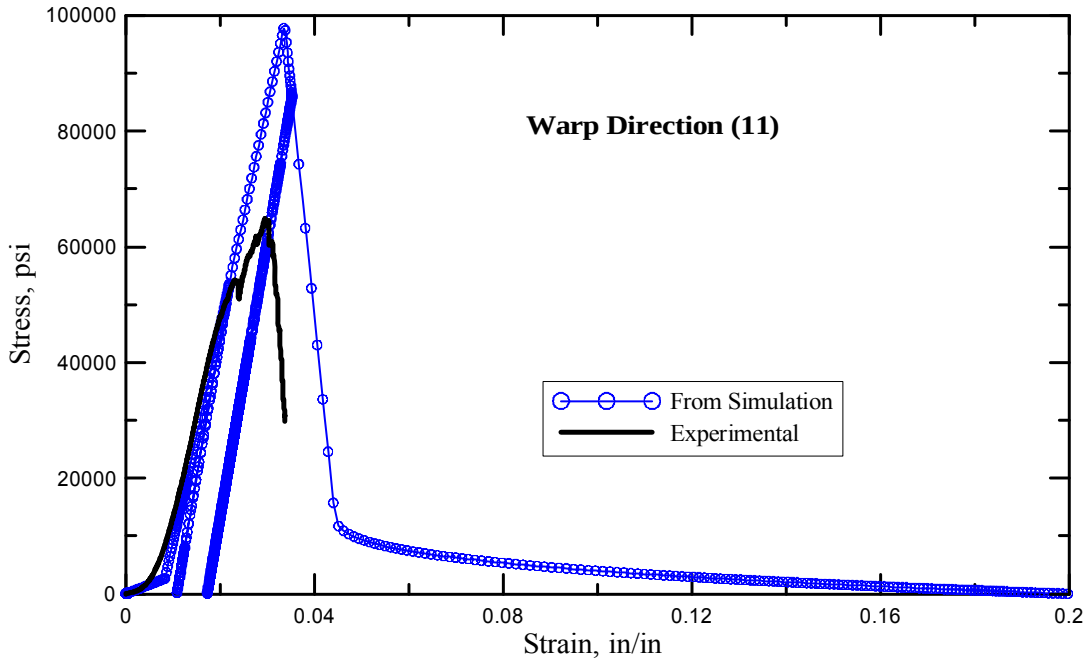

Figure 51. Warp Direction Stress-Strain Response in Simulation

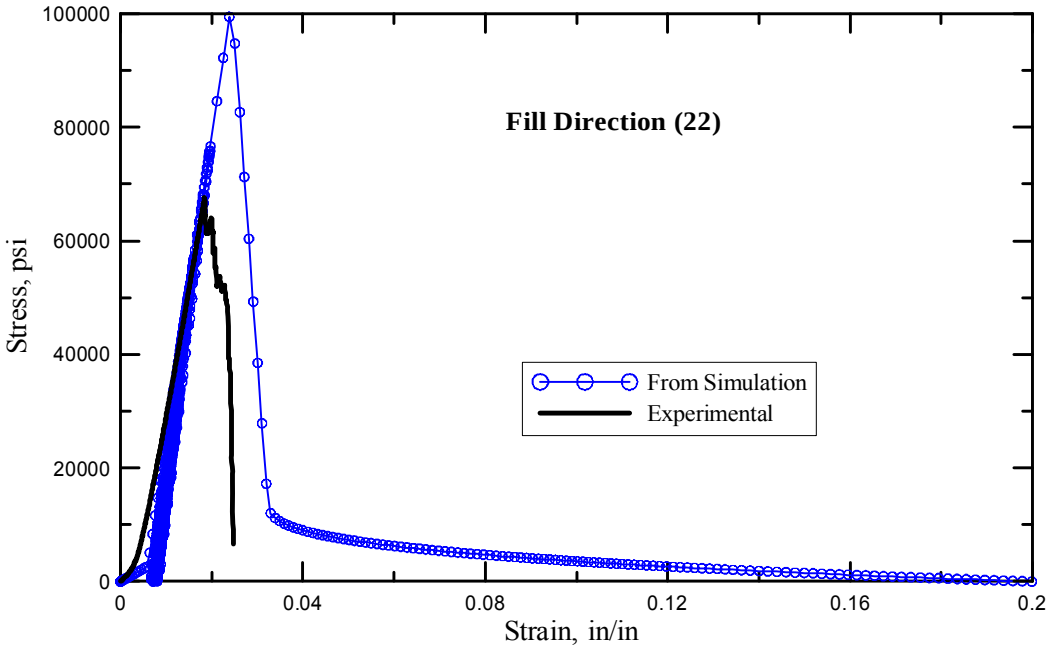

Figure 52. Fill Direction Stress-Strain Response in Simulation

2.3.3.6 Energy Balance Check.

The quality of each analysis was ascertained by comparing the hourglass energy against the total energy of the material or system. In addition, the energy ratio of the system, defined as the total energy in the system at any time divided by the initial total energy of the system, was checked as well.

LG404 is a typical simulation for a 0° impact where there is a relatively low amount of element deletions. Figure 53 shows the energy ratio as a function of time for the LG404 simulation. Figure 54 shows various energy values versus time for the LG404 simulation, including the total kinetic, internal, sliding, and hourglass energies of the system. Figure 55 shows the kinetic, internal, and hourglass energies of the fabric material only versus time for the LG404 simulation. The time units are in milliseconds and the energy units are in lbf-in(10^6).

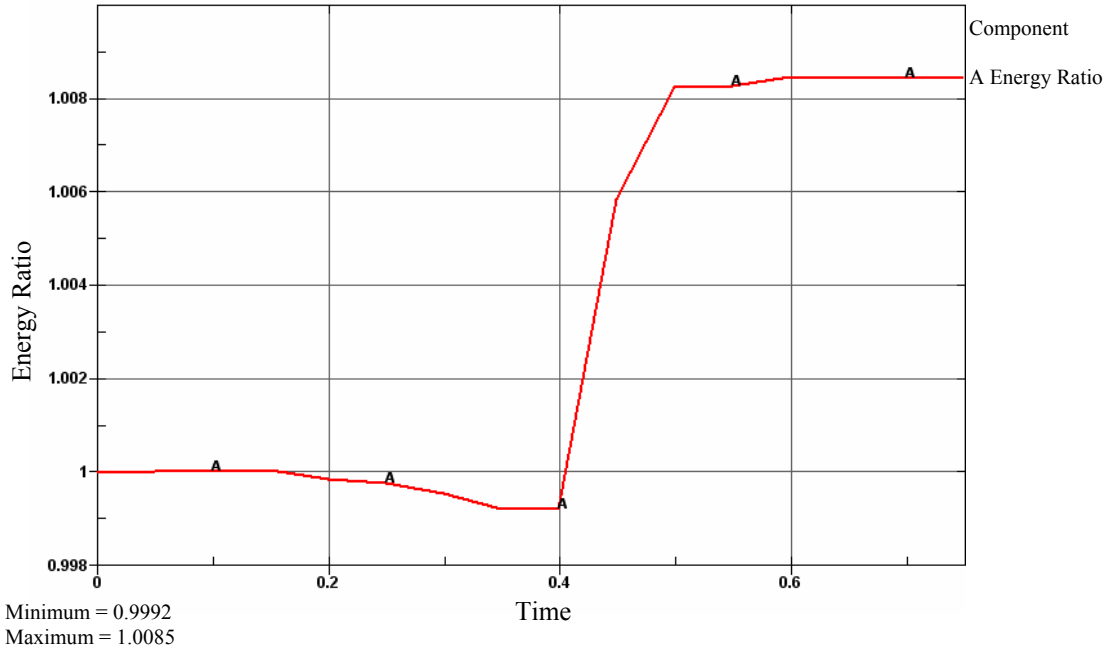

Figure 53. Energy Ratio vs Time for LG404 Simulation

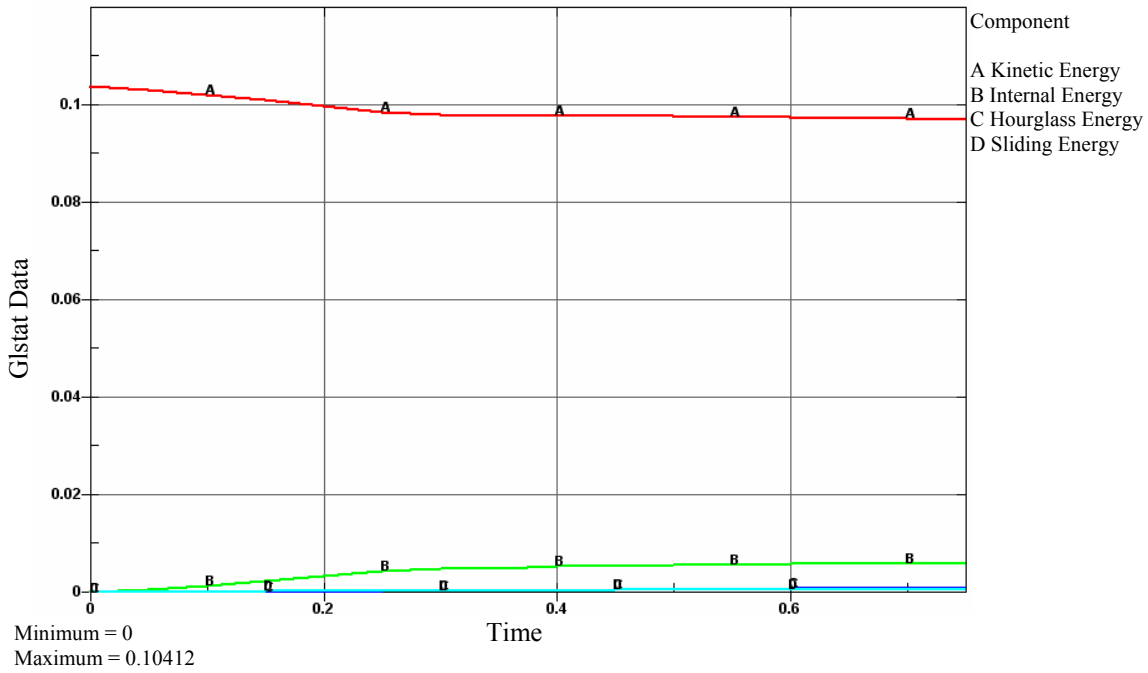

Figure 54. Various Energy Values vs Time for LG404 Simulation

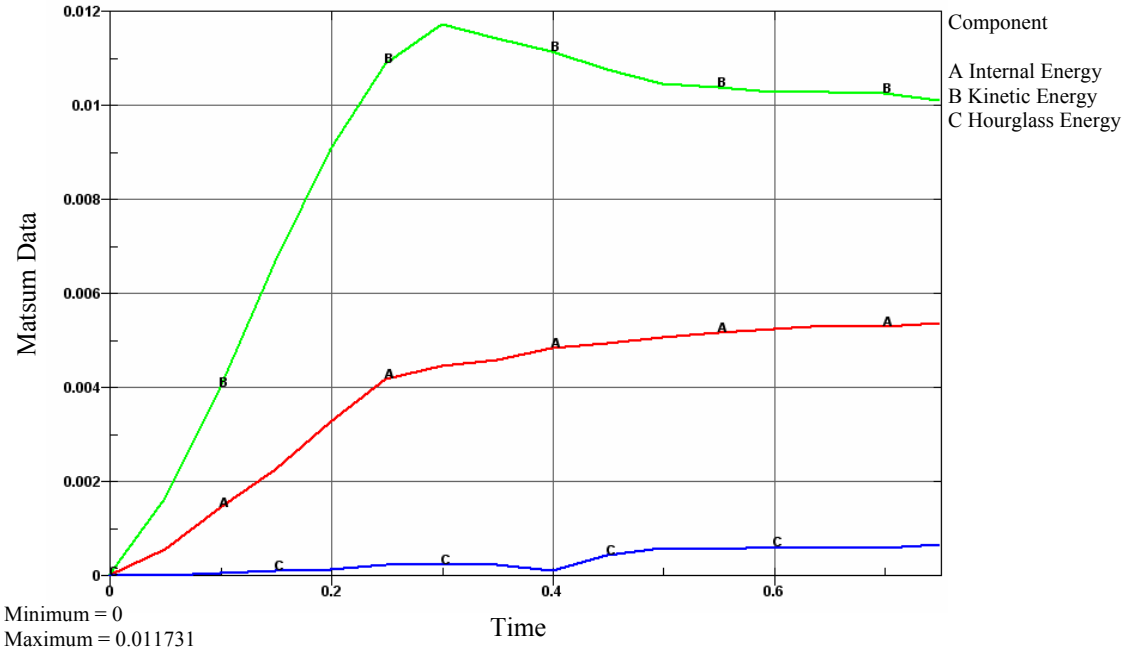

Figure 55. Various Energy Values vs Time of Fabric Material Only for LG404 Simulation

LG620 is a typical simulation for an oblique impact where there is a relatively high amount of element deletions. Figure 56 shows the energy ratio as a function of time for the LG620 simulation. Figure 57 shows various energy values vs time for the LG620 simulation, including the total kinetic, internal, sliding, and hourglass energies of the system. Figure 58 shows the kinetic, internal, and hourglass energies of the fabric material only versus time for the LG620 simulation.

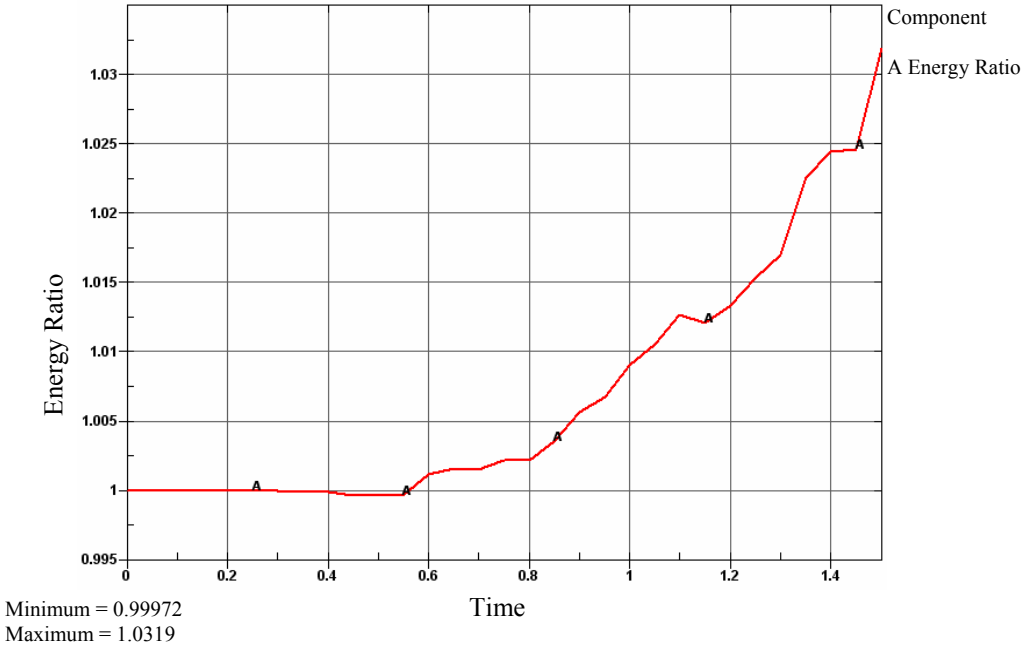

Figure 56. Energy Ratio vs Time for LG620 Simulation

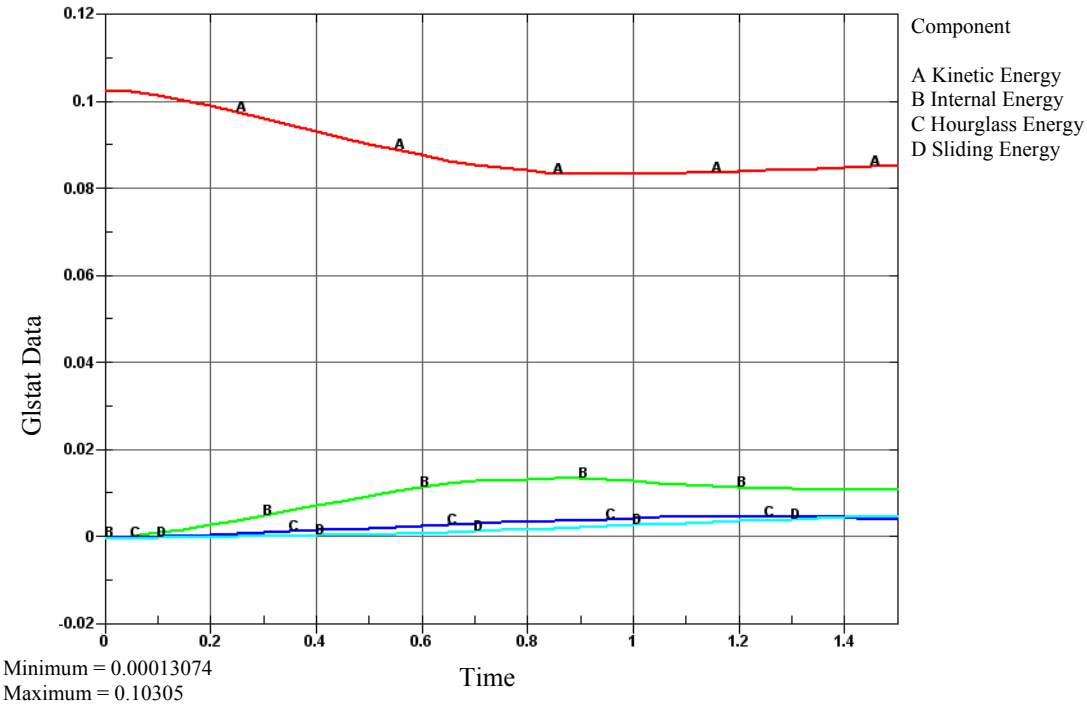

Figure 57. Various Energy Values vs Time for LG620 Simulation

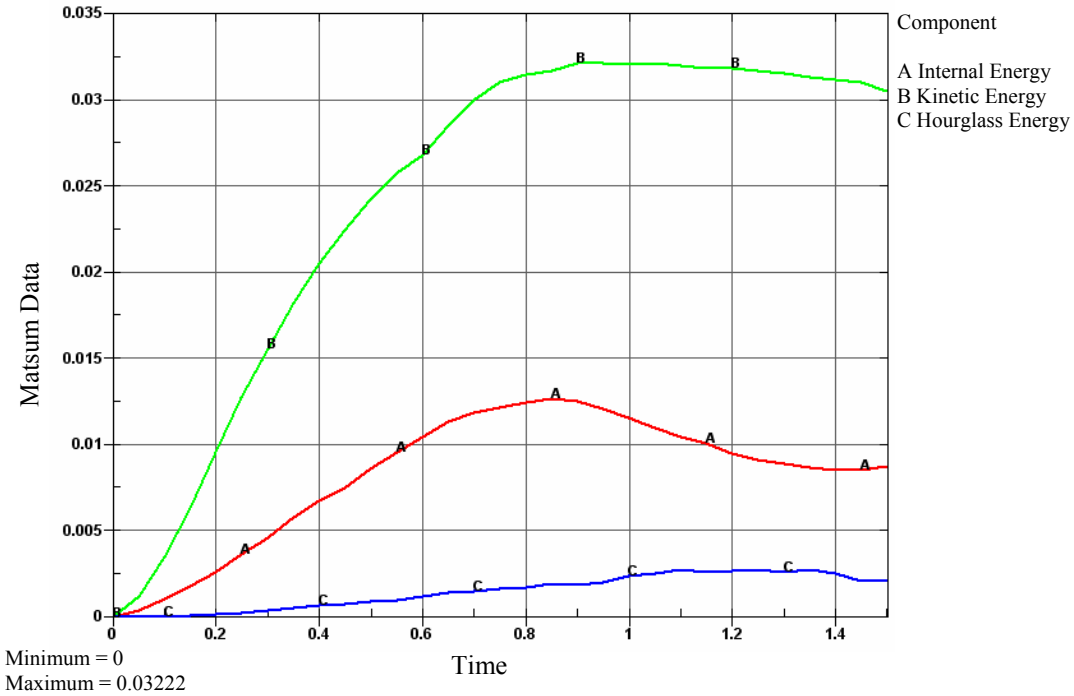

Figure 58. Various Energy Values vs Time of Fabric Material Only for LG620 Simulation

It is clear from the figures that the hourglass energies are relatively small. Table 8 shows various energy values for all the simulations. It is apparent that the hourglass energies of the fabric are small compared to the total energy of the fabric.

Table 8. Various Fabric Energy Values for All Simulations

Run	Test	Maximum/ Minimum Energy Ratio	Energy Ratio Just After Projectile Penetration	Fabric Hourglass Energy Just After Projectile Penetration (lbf-in(10^6))	Fabric Kinetic Energy Just After Projectile Penetration (lbf-in(10^6))	Fabric Internal Energy Just After Projectile Penetration (lbf-in(10^6))	Hourglass Energy as % of Total Energy of Fabric
1	LG403	1.008	0.999	0.0001	0.0044	0.0020	1.9
2	LG404	1.003	1.000	0.0004	0.0110	0.0044	2.5
3	LG405	1.002	—	0.0111	0.0507	0.0308	12.0
4	LG409	1.004	0.999	0.0002	0.0113	0.0046	1.5
5	LG410	1.004	1.000	0.0001	0.0019	0.0013	2.2
6	LG411	1.000	—	0.0102	0.0494	0.0305	11.3
7	LG424	1.009	0.999	0.0006	0.0166	0.0058	2.8
8	LG427	0.996	0.998	0.0033	0.0364	0.0166	5.9
9	LG429	0.999	0.999	0.0015	0.0286	0.0113	3.6
10	LG432	0.999	0.999	0.0011	0.0240	0.0100	3.1
11	LG433	1.000	1.000	0.0001	0.0028	0.0024	2.7
12	LG434	1.000	1.000	0.0002	0.0028	0.0026	3.1
13	LG444	0.998	0.998	0.0003	0.0038	0.0076	2.2
14	LG449	1.080	1.080	0.0001	0.0021	0.0104	1.0
15	LG609	1.000	0.993	0.0004	0.0063	0.0039	3.9
16	LG610	1.005	1.005	0.0011	0.0103	0.0055	6.4
17	LG611	1.002	1.002	0.0011	0.0144	0.0053	5.3
18	LG612	1.006	1.000	0.0009	0.0100	0.0039	6.3
19	LG618	1.031	1.020	0.0035	0.0510	0.0203	4.7
20	LG620	1.032	1.013	0.0028	0.0322	0.0126	5.8
21	LG655	0.997	0.998	0.0018	0.0094	0.0085	9.1
22	LG656	0.990	0.991	0.0051	0.0260	0.0160	10.9
23	LG657	1.002	—	0.0086	0.0476	0.0320	9.7
24	LG689	1.003	0.999	0.0032	0.0390	0.0110	6.0
25	LG692	1.111	1.003	0.0052	0.0581	0.0109	7.0
26	LG594	1.112	1.026	0.0035	0.0453	0.0186	5.2

2.3.4 Sensitivity Analysis of Material Model.

A sensitivity analysis of the material model was performed to determine the model's sensitivity to various input parameters. These parameters included the elastic modulii (E_{11} and E_{22}), the unloading and reloading modulus (E^{unl}), the shear modulii (G_{12}, G_{23}, and G_{31}), the factor *dfac*,

the failure strain, the coefficient of friction, the stress at which the nonlinear stress-strain relation begins in the post-peak region (σ*), the projectile orientation, and the computational precision. For parameters that were taken from experimental results, such as E_{11} and E_{22}, the values were adjusted by -10%, -5%, -1%, +1%, +5%, and +10%. For other parameters that were assumed in the material model, such as *dfac* and the failure strain, lower and higher values than the assumed values were used. Only 6 of the 26 test cases were used for the sensitivity analysis. The six cases were chosen to be representative of all the cases. Table 9 lists the selected test cases.

Table 9. Test Cases Used in Sensitivity Analysis

Test	Layers	Projectile Orientation			Initial Velocity (ft/sec)
		Roll (deg)	Pitch (deg)	Yaw (deg)	
LG404	8	0	0	0	895.67
LG432	16	0	0	0	895.67
LG611	8	30.89	-1.74	-10.78	905.68
LG620	8	-37.79	0.18	55.07	893.83
LG656	32	8.98	-2.31	-10.07	967.31
LG689	8	-12.83	-1.28	49.72	896.26

Reported in the following sections are the percent difference values between the simulations using the actual values and the simulations using the adjusted values. A positive difference indicates a lower absorbed energy using the adjusted value, and a negative difference indicates a higher absorbed energy using the adjusted value. For the parameters that were adjusted by a percentage, the average difference values are shown on the plot and are connected by a line to show the general trend.

2.3.4.1 Sensitivity of Material Model to E_{11} and E_{22}.

The values for E_{11} and E_{22} were adjusted by -10%, -5%, -1%, +1%, +5%, and +10%, and simulations of the six test cases were run. Figures 59 and 60 show the results.

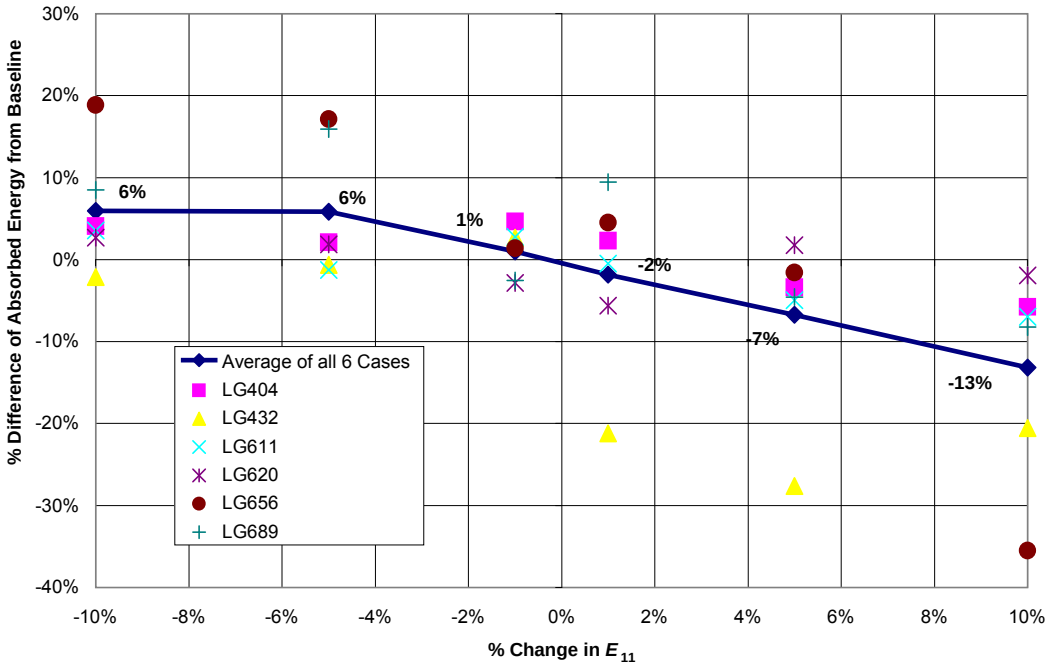

Figure 59. Sensitivity of Material Model to E_{11}

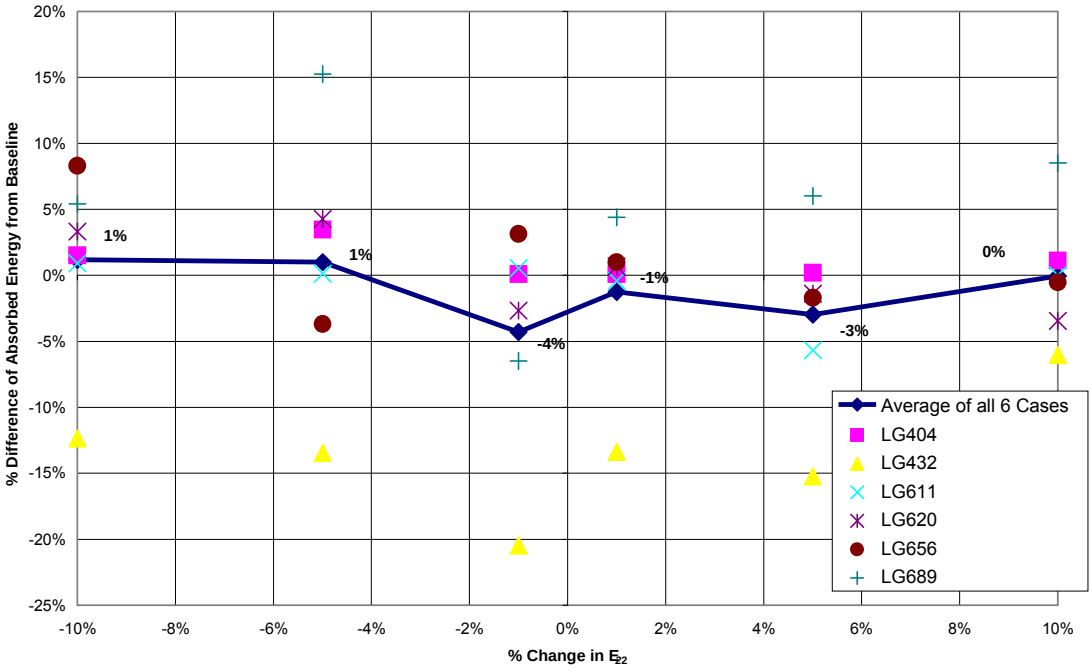

Figure 60. Sensitivity of Material Model to E_{22}

2.3.4.2 Sensitivity of Material Model to G_{12}.

The value for G_{12} was adjusted by -10%, -5%, -1%, +1%, +5%, and +10%, and simulations of the six test cases were run. Figure 61 shows the results.

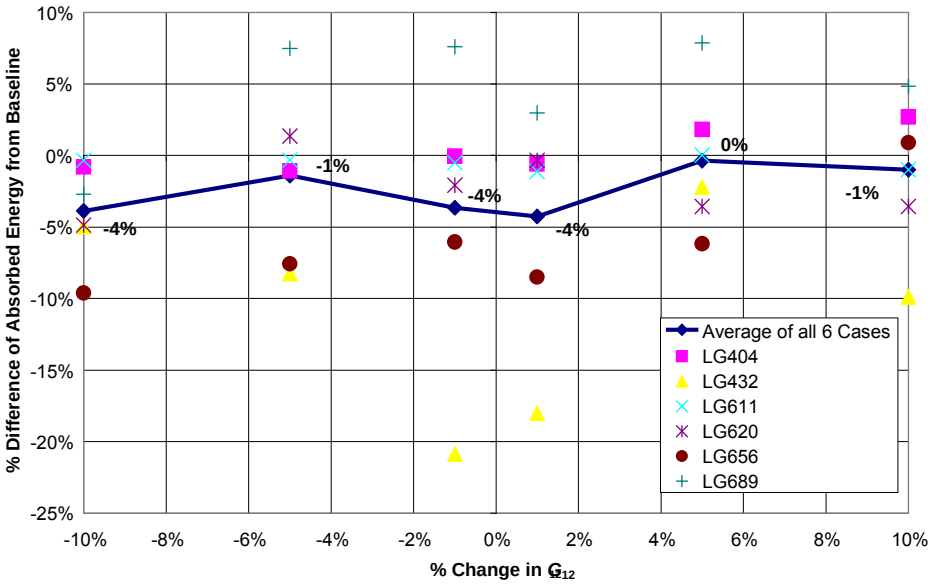

Figure 61. Sensitivity of Material Model to G_{12}

2.3.4.3 Sensitivity of Material Model to the Unloading and Reloading Modulus.

The value for the unloading and reloading modulus, E^{unl}, was adjusted by -10%, -5%, -1%, +1%, +5%, and +10%, and simulations of the six test cases were run. Figure 62 shows the results.

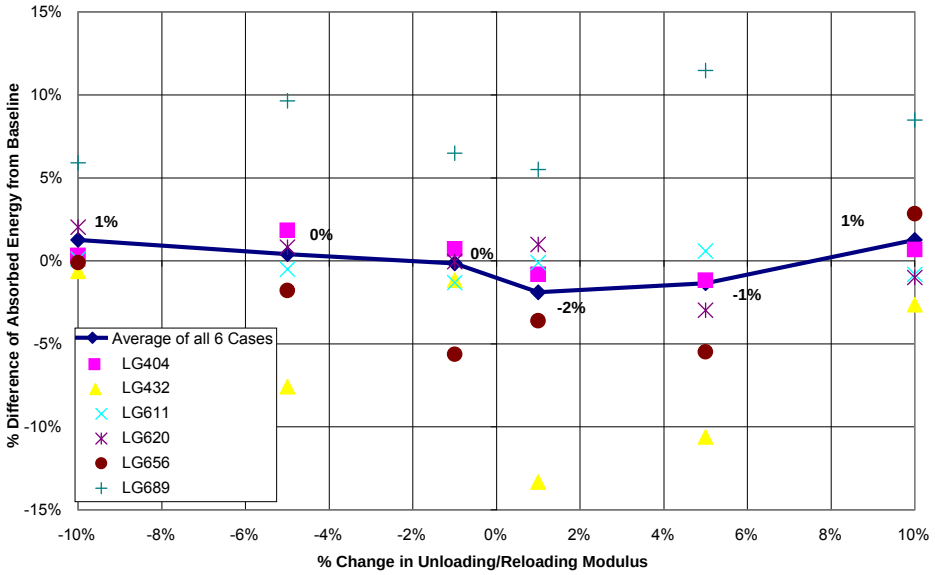

Figure 62. Sensitivity of Material Model to Unloading/Reloading Modulus

2.3.4.4 Sensitivity of Material Model to the Coefficient of Friction.

The static and dynamic coefficient of friction for steel on fabric (μ_{sf}) used in the material model was 0.10. Simulations of the six test cases were run using different values—0.0, 0.05, 0.15, and

0.20. Figure 63 shows that the average differences from baseline are 4%, 3%, -2%, and -11%, respectively, when the coefficient of friction for steel on fabric increases from 0 to 0.20.

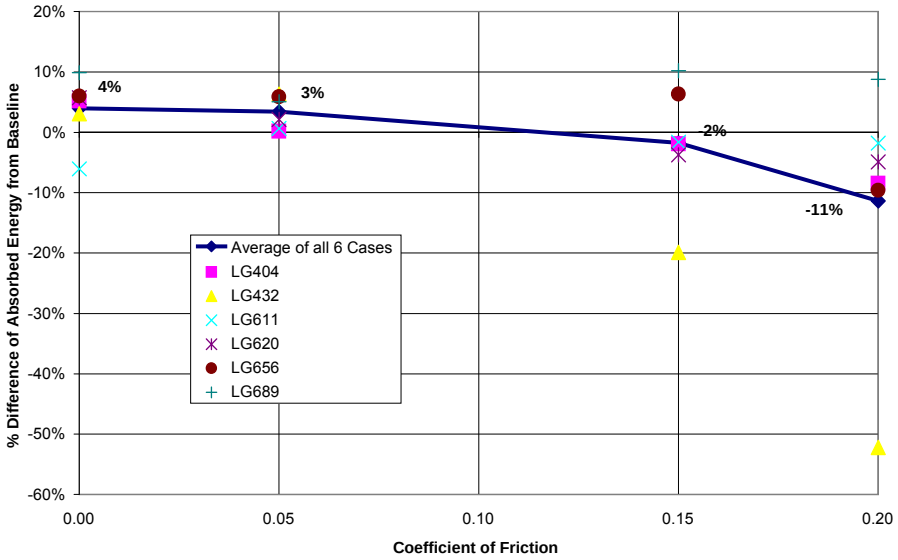

Figure 63. Sensitivity of Material Model to the Coefficient of Friction

2.3.4.5 Sensitivity of Material Model to the Failure Strain.

The failure strain used in the material model was 0.20 for both the warp and fill directions. Simulations of the six test cases were run using alternative values of 0.15 and 0.25. Figure 64 shows the results.

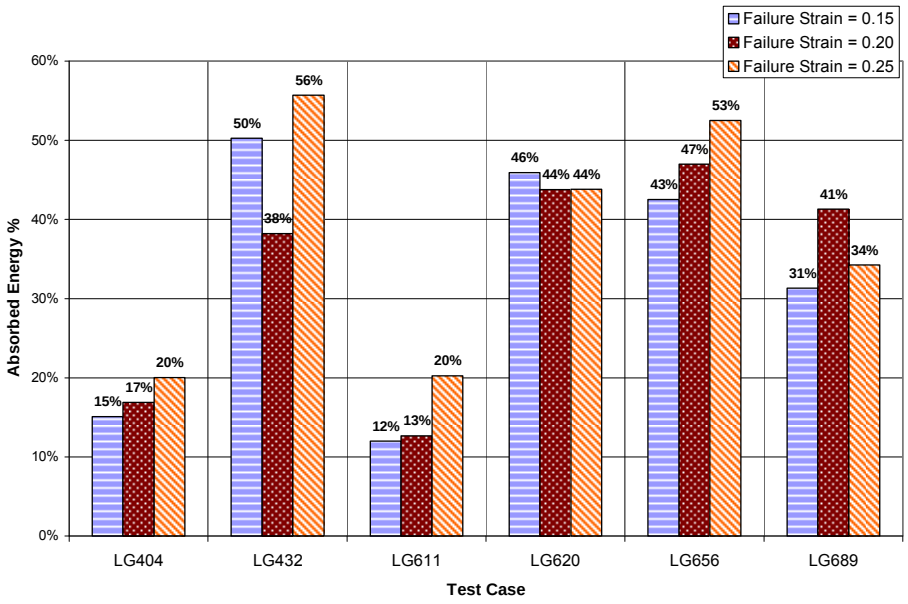

Figure 64. Sensitivity of Material Model to Failure Strain

2.3.4.6 Sensitivity of Material Model to the *dfac* Factor.

The *dfac* factor used in the material model was 0.30 for both the warp and fill directions. Simulations of the six test cases were run using alternative values of 0.20 and 0.40. Figure 65 shows the results.

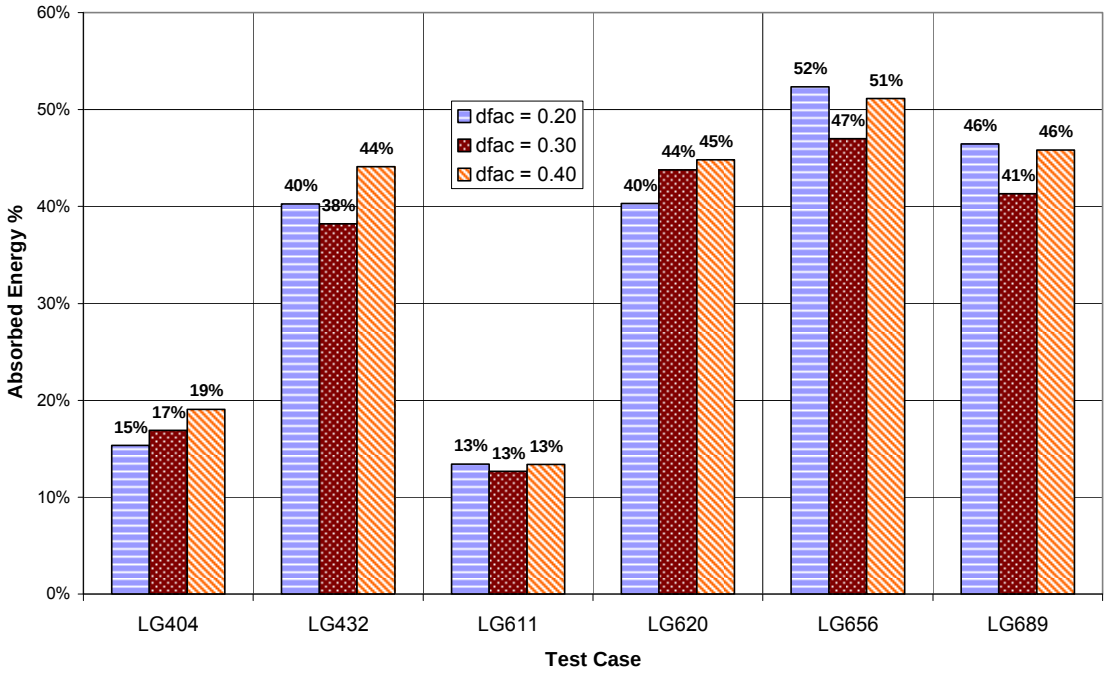

Figure 65. Sensitivity of Material Model to *dfac* Factor

2.3.4.7 Sensitivity of Material Model to the σ* Value.

The σ* value used in the material model was 15,000 psi for both the warp and fill directions. Simulations of the six test cases were run using alternative values of 10,000 and 20,000 psi. Figure 66 shows the results.

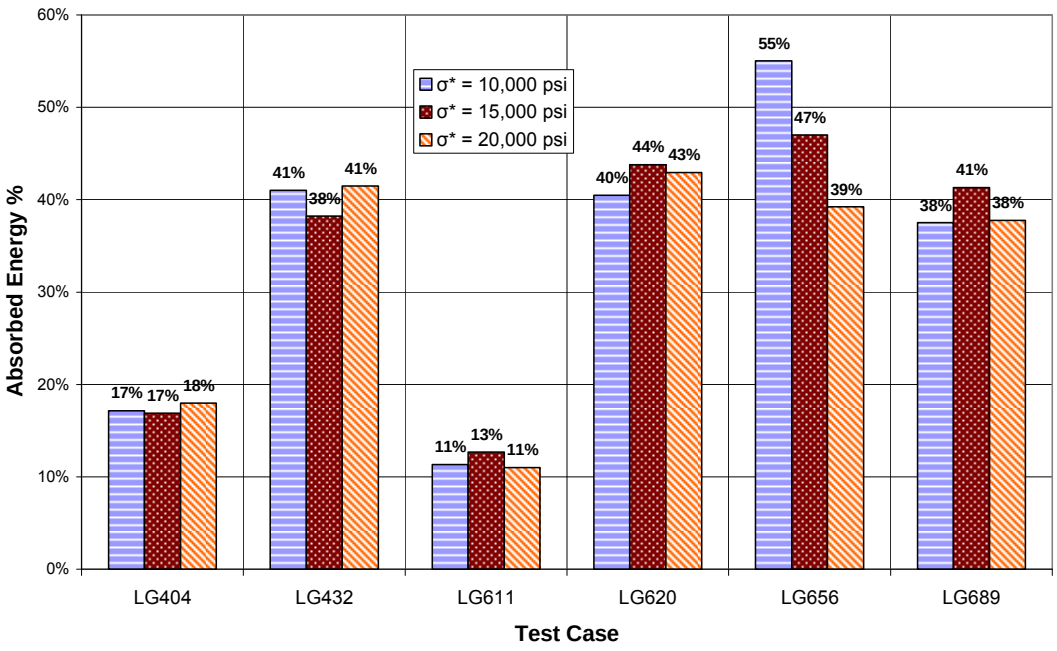

Figure 66. Sensitivity of Material Model to σ* Value

2.3.4.8 Sensitivity of Material Model to the Projectile Orientation.

For the six test cases, the projectile orientation was adjusted by +1.0° in the pitch direction. Figure 67 shows the results. Note that LG656 and LG689 were quite sensitive to the change of projectile orientation. LG656 is an 8-FE layer model. The 1-degree change in the pitch increased the absorbed energy from 47% to 73%. There are two reasons for this large change. First, the pitch change increases the (projected) area where the projectile comes into contact with the fabric. This allows for larger fabric deformation to take place. Second, there is a slight decrease in the number of failed elements (from 47 to 39). Consequently, there is an increase in the overall absorbed energy. On the other hand, LG689 is a 2-FE layer model. The 1-degree change in the pitch decreased the absorbed energy from 41% to 26%. In this case, there is a large decrease in the contact area. In both cases, the projectile rotates and tumbles out after penetrating the fabric layers. The kinetic energy of the projectile decreases from 11,785 to 6,953 J in about 1.9 ms in the baseline model. In the rotated model, the decrease is only to 8721 J in about 1.8 ms.

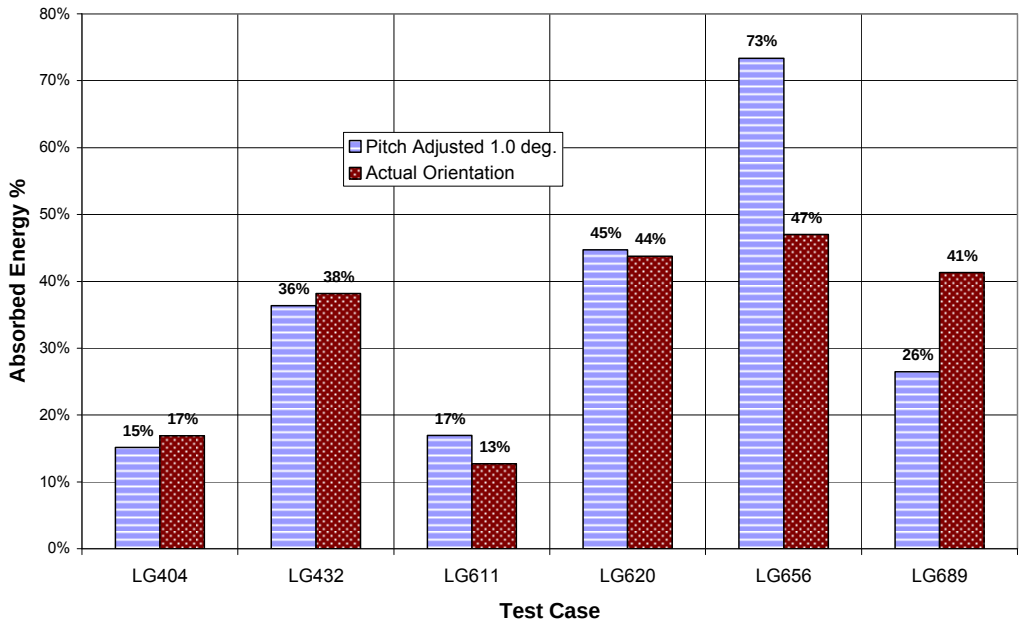

Figure 67. Sensitivity of Material Model to Projectile Orientation

2.3.4.9 Sensitivity of Material Model to the G_{23} and G_{31}.

The out-of-plane shear modulus (G_{23} and G_{31}) used in the material model was 50,000 psi. Simulations of the six test cases were run using alternative values of 40,000 and 60,000 psi. Figure 68 shows the results.

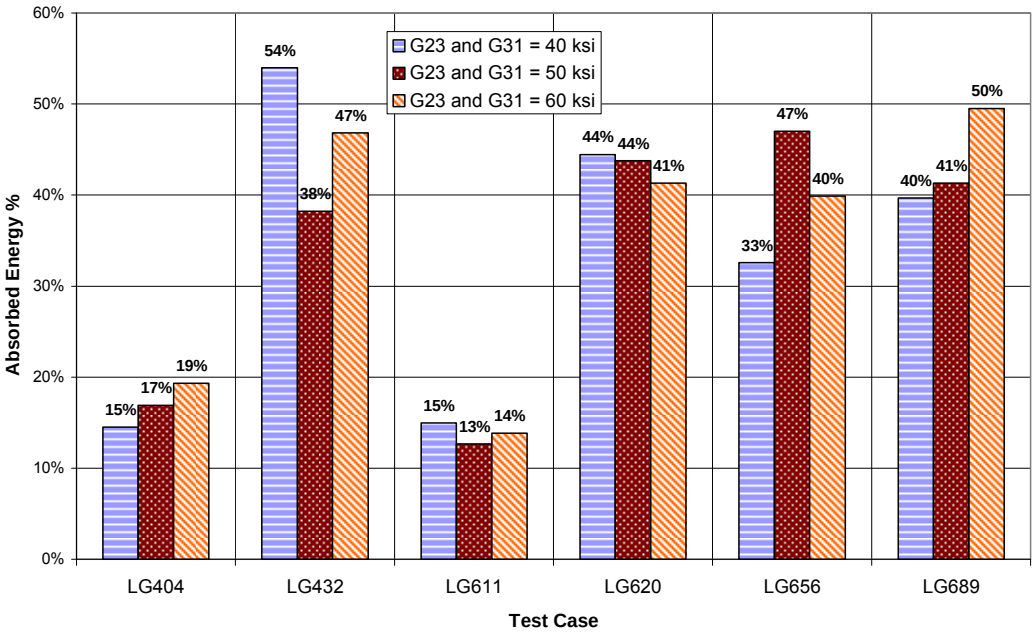

Figure 68. Sensitivity of Material Model to G_{23} and G_{31}

2.3.4.10 Sensitivity of Material Model to the Analysis Precision.

All 26 test cases were run using LS-DYNA's single-precision version. The six test cases for the sensitivity analysis were run using LS-DYNA's double-precision version. Figure 69 shows the results. Figure 70 shows a comparison of the total analysis time.

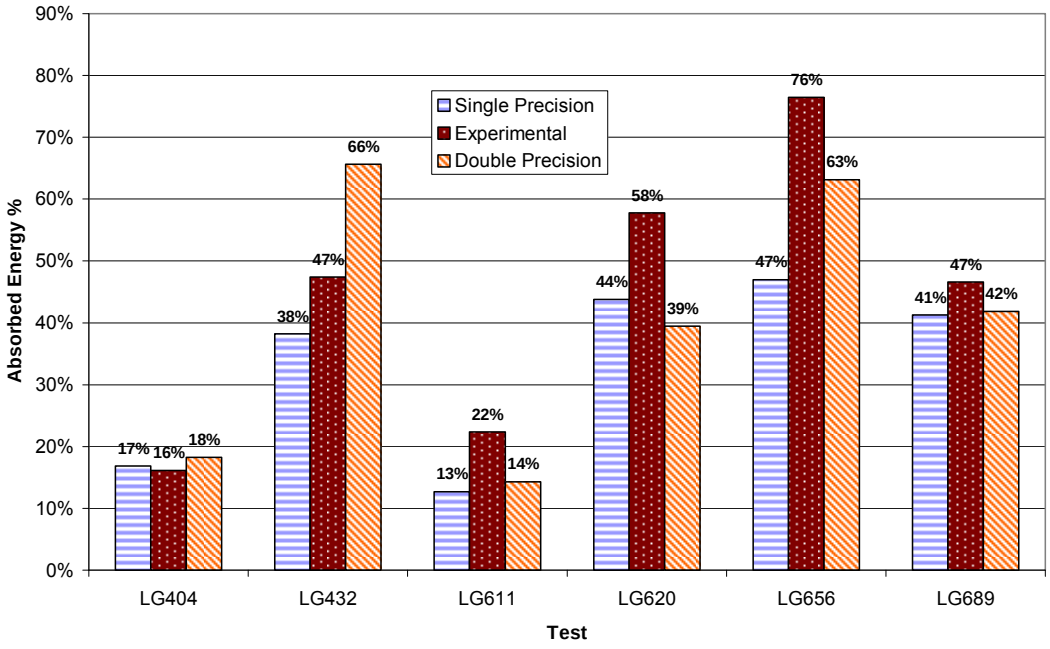

Figure 69. Sensitivity of Material Model to Analysis Precision

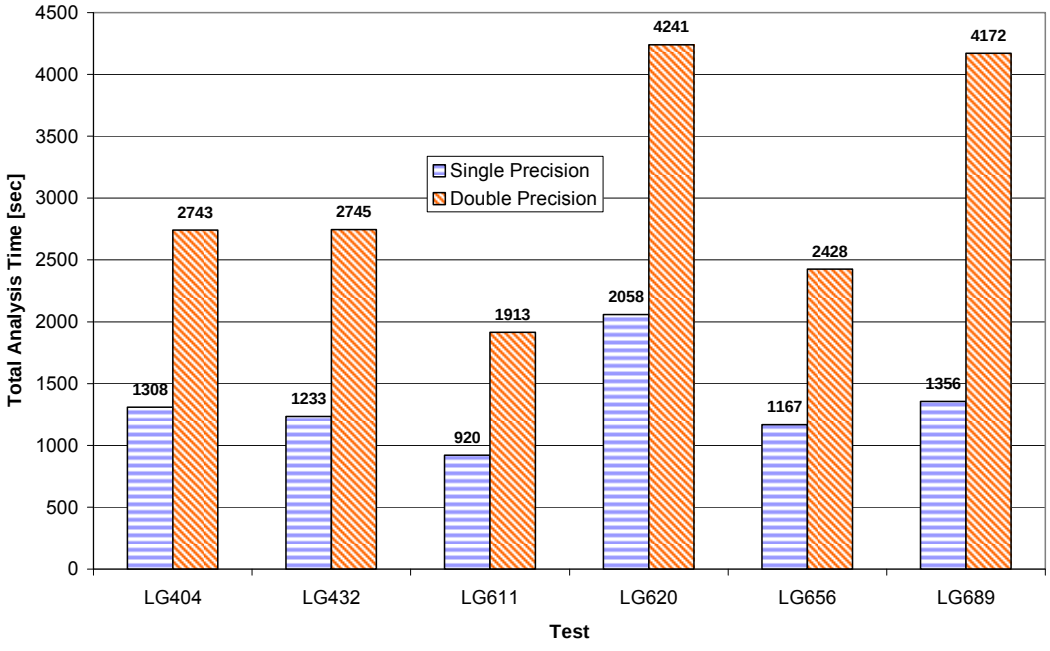

Figure 70. Total Analysis Time for Single- and Double-Precision Versions

2.3.4.11 Summary.

In general, the material model's performance appears to be fairly sensitive to its parameters, as summarized in table 10. The test cases in the study that were the most sensitive were those that had a larger number of fabric layers (LG432 – 16 layers and LG656 – 32 layers). This was most apparent in the model's sensitivity to the out of plane shear modulii (G_{23} and G_{31}). This was expected, however, due to the inaccuracies in modeling the shear response with only one element thick assumption for multiple layers of fabric. The sensitivity of the projectile orientation was studied, as it is unknown how accurate the reported projectile orientations were. Results show that by changing the reported orientation by 1 degree in the pitch direction, the model was quite sensitive in two cases (LG656 and LG689). However, a larger suite of test cases would likely be needed to draw a more general conclusion.

Table 10. Comparison of Sensitivity Values

Parameter	Change From Baseline Percentage					
	-10	-5	-1	1	5	10
E_{11}	6 (1)	6 (1)	1	-2	-7 (1)	-13 (1)
E_{22}	1	1	-4 (1)	-1	-3	0
G_{12}	-4	-1	-4 (1)	-4 (1)	0	-1
E^{unl}	1	0	0	-2	-1	1

Friction Coefficient	Change From Baseline			
μ_{sf}	0	0.05	0.15	0.20
	4%	3%	-2%	-11%

A ranking of the parameters from the material model's highest sensitivity to lowest sensitivity based on the sensitivity analysis and from general observations during this research is as follows:

- (1) E_{11}
- (2) Cowper-Symonds factors
- (3) Coefficient of friction
- (4) G_{12}
- (5) Projectile orientation
- (6) Analysis precision
- (7) G_{23} and G_{31}
- (8) E_{22}
- (9) Failure strain
- (10) Unloading/reloading modulus
- (11) *dfac* factor
- (12) σ* value

Although the Cowper-Symonds factors were not included formally in the sensitivity analysis, experience has shown that the model is very sensitive to them as well. In general, it can be concluded that the model is most sensitive to any parameter that affects the area under the assumed stress-strain curves such as the elastic stiffness, the strain-to-peak stress, and the strain rate parameters.

2.4 RE-ANALYSIS AND IMPROVEMENTS FOR THE ASU CONTINUUM MODEL.

2.4.1 Introduction.

In section 2.3, a Kevlar 49 material model was developed based on the results from static and dynamic experimental tests and included a nonlinear stress-strain response, strain rate effects, and a failure criterion. The constitutive model was incorporated into the LS-DYNA FE program through a user-defined material model and was validated by comparing the results against experimental ballistic tests. In this model, fabric layers were represented by a single FE layer. The thickness of the FE layer was assumed to be equal to the thickness of the total number of layers in the model. Although the simulation results were shown to match closely with the experimental tests for most test cases, the results for the very low or very high projectile velocity test cases showed noticeable differences. Further, the friction between the fabric layers is considered to be an important factor in fabric behavior. However, a single-layer model cannot capture the layer-to-layer frictional behavior. In the following sections, the improvements made to the constitutive and modeling methodologies are discussed.

2.4.2 The ASU Continuum Model Version 1.1.

2.4.2.1 Improvements in Current Continuum Model.

The primary failure mode of Kevlar 49 is the tensile breakage of the warp or fill direction yarns. There were several options to compute the failure strain value. One was to assume the failure strain was simply the strain reported at the end of the tension tests. However, after analyzing the deformed fabric samples, it was determined that much larger strains are required to fully fail the fabric yarns. One of the fabric samples at the end of the warp direction tension test is shown in figure 71.

From the deformation shown in figure 71, it is clear that the fabric can experience strains larger than the last reported strain value from the test results. Testing was terminated when the load-carrying capacity of the fabric reached almost zero. To simplify and simulate this in the material model, the post-peak region was approximated with a linear region followed by a nonlinear region to fabric failure.

Figures 72 and 73 show the experimental swath tensile test results and the ASU material model (ASUumatV1.0). In ASUumatV1.0, a simple approach was used to model fabric failure in an FE simulation—once the element representing the fabric experienced a critical level of strain in either the warp or fill directions, the element was considered to have failed. The critical value was taken as 0.2 for fill and warp directions.

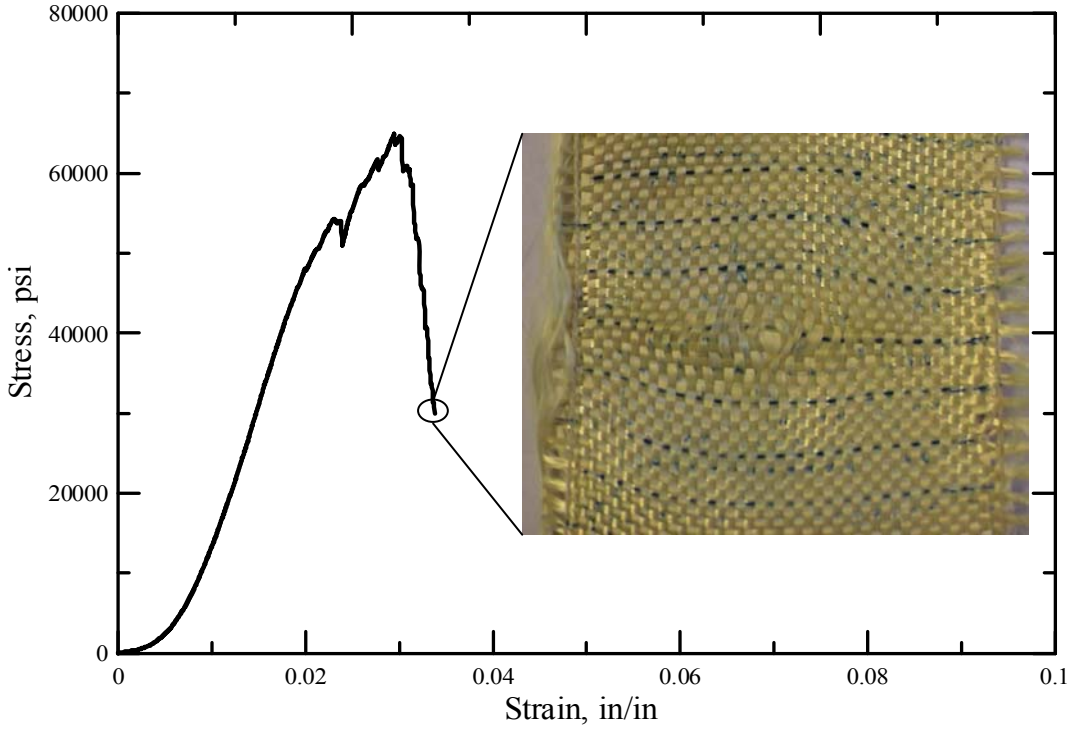

Figure 71. Fabric Sample at the end of Warp Direction Tension Test

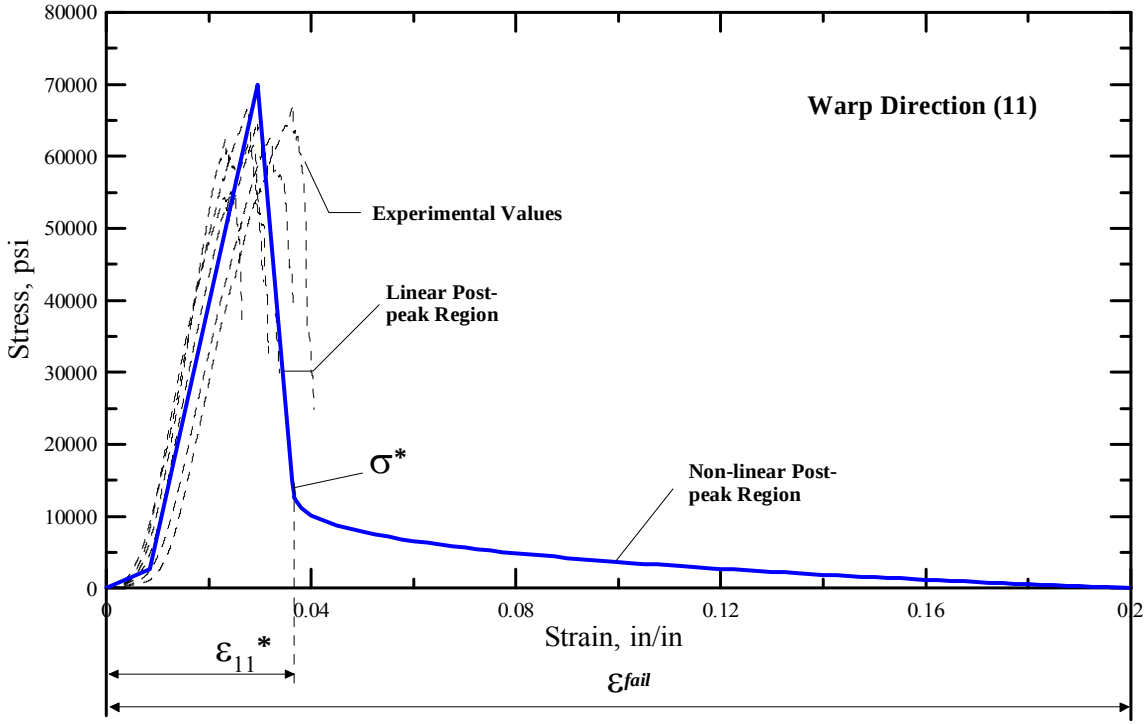

Figure 72. Kevlar 49 Warp Direction Uniaxial Stress-Strain Results With Approximation for Pre- and Post-Peak Behavior

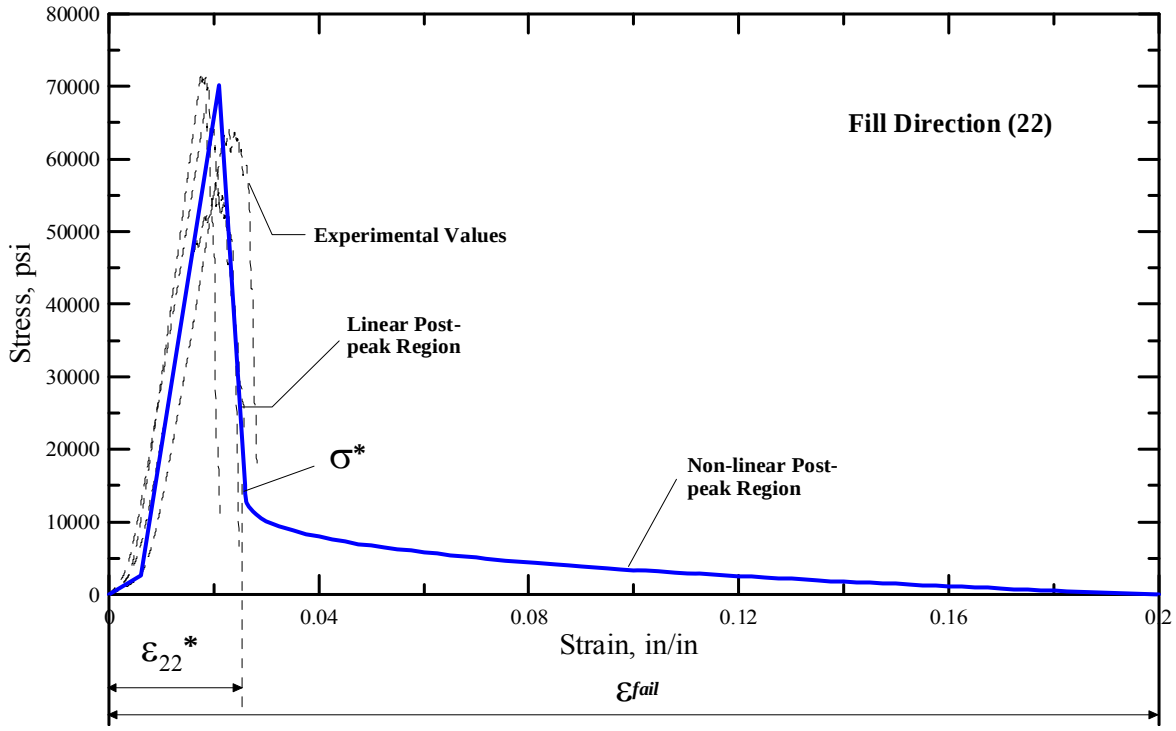

Figure 73. Kevlar 49 Fill Direction Uniaxial Stress-Strain Results With Approximation for Pre- and Post-Peak Behavior

In ASUumatV1.1, the following two modifications were made to improve the material model.

1. The stress at which the post-peak nonlinear curve starts was reduced from 15,000 to 5,000 psi. This resulted in lesser load-carrying capacity of the fabric under the post-peak region, which is closer to actual experimental tests.

2. The failure in the fill and warp directions was decoupled by providing separate failure strains in both directions. If the strain in one direction reaches the failure value, the load-carrying capacity in that direction was reduced to zero. The other direction still had load-carrying capacity until the strain in that direction reached failure strain. This failure strain in ASUumatV1.1 is taken as 0.1. To limit total strain in any direction, the overall strain in the element in any direction was restricted to 0.35. The element was eroded when the strain reached this limiting value.

Figures 74 and 75 show the comparison of the ASUumatV1.0 and ASUumatV1.1 material models for both warp and fill directions, respectively. Table 11 lists the parameters used in these two material models.

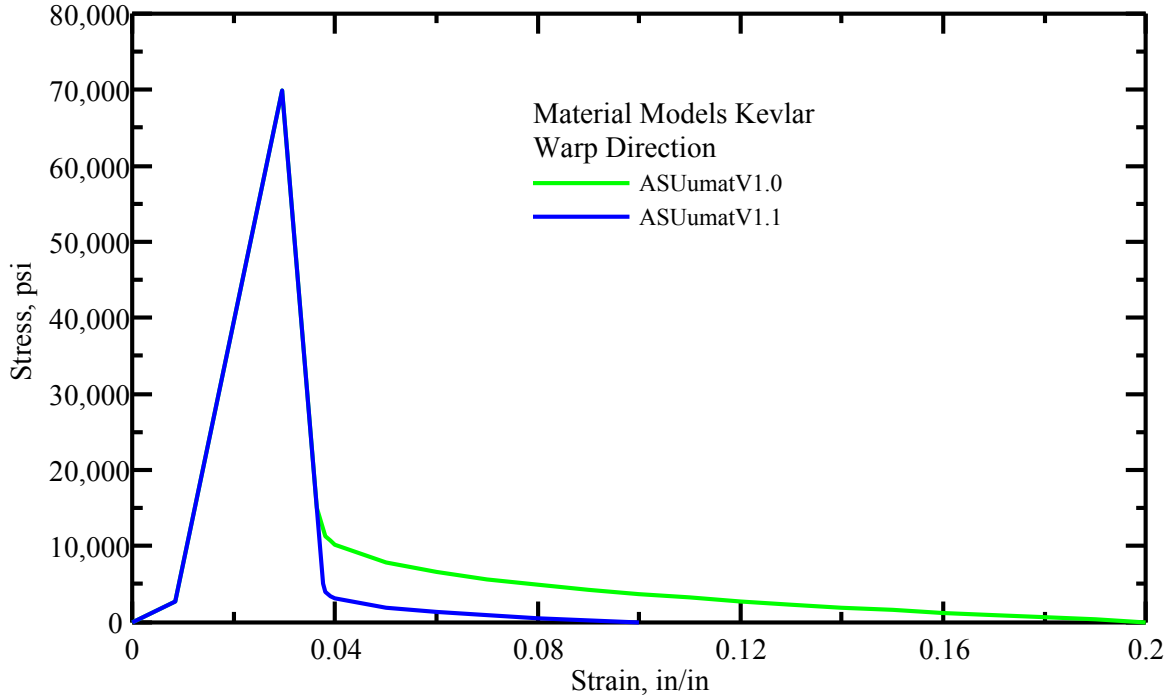

Figure 74. Kevlar 49 Warp Direction Load Curves Used in ASUumatV1.0 and ASUumatV1.1

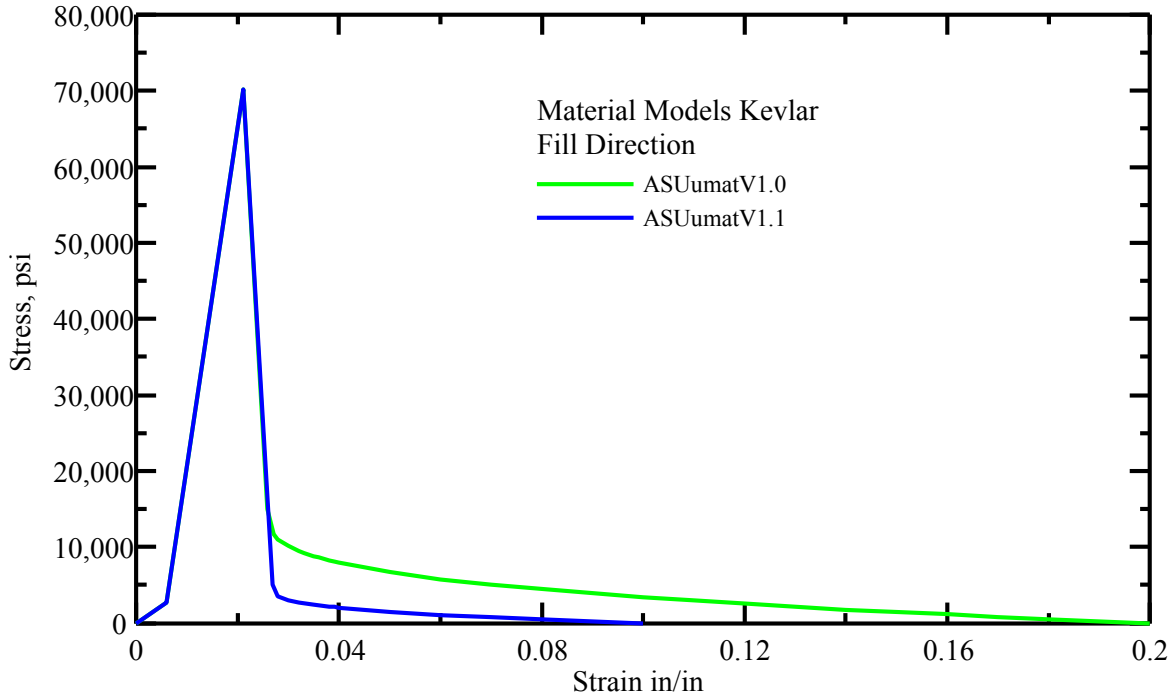

Figure 75. Kevlar 49 Fill Direction Load Curves Used in ASUumatV1.0 and ASUumatV1.1

Table 11. Comparison of Parameters Used in ASUumatV1.0 and ASUumatV1.1

Material Constant	UMAT Notation	Symbol	Value ASUumatV1.0	Value ASUumatV1.1
Warp stiffness in elastic region (psi 10^6)	Ex	E_{11}	3.2	3.2
Fill stiffness in elastic region (psi 10^6)	Ey	E_{22}	4.5	4.5
Warp and fill direction crimp stiffness factor	Ecrfac	E^{crp}	0.1	0.1
Warp and fill direction post-peak linear region stiffness factor	Esoftfac	E^{soft}	-2.5	-2.5
Unloading/reloading stiffness factor	Eunlfac	E^{unl}	1.5	1.5
Compressive stiffness factor	Ecompfac	E^{comp}	0.005	0.005
Shear stiffness (G_{23}) (psi 10^6)	Gyz	G_{23}	0.05	0.05
Shear stiffness (G_{23}) (psi 10^6)	Gzx	G_{31}	0.05	0.05
Shear stiffness linear region 1 (G_{12}) (psi 10^6)	Gxy1	G_{12}	0.001	0.001
Shear stiffness linear region 2 (G_{12}) (psi 10^6)	Gxy2	G_{12}	0.008	0.008
Shear stiffness linear region 3 (G_{12}) (psi 10^6)	Gxy3	G_{12}	0.040	0.040
Shear stiffness linear region 4 (G_{12}) (psi 10^6)	Gxy4	G_{12}	0.300	0.300
Shear strain 1 (rad)	gammaxy1	γ_{12}	0.350	0.350
Shear strain 2 (rad)	gammaxy2	γ_{12}	0.500	0.500
Shear strain 3 (rad)	gammaxy3	γ_{12}	0.570	0.570
Warp direction crimp strain (in/in)	ecrpx	ε_{11}^{crp}	0.0085	0.0085
Fill direction crimp strain (in/in)	ecrpy	ε_{22}^{crp}	0.006	0.006
Warp direction strain at peak stress (in/in)	emaxx	$\varepsilon_{11}^{\max}$	0.0295	0.0295
Fill direction strain at peak stress (in/in)	emaxy	$\varepsilon_{22}^{\max}$	0.0210	0.0210
Stress at post-peak nonlinearity (psi 10^6)	sigpost	σ^*	0.015	0.005
Warp direction failure strain (in/in)	efailx	ε_{11}^{fail}	0.2	0.1
Fill direction failure strain (in/in)	efailx	ε_{22}^{fail}	0.2	0.1
Cowper-Symonds factor for stiffness (ms^{-1})	C(E)	C_E	0.005	0.005
Cowper-Symonds factor for stiffness (ms^{-1})	P(E)	P_E	40.0	40.0
Cowper-Symonds factor for strain (ms^{-1})	C(e)	C_ε	0.005	0.005
Cowper-Symonds factor for strain (ms^{-1})	P(e)	P_ε	40.0	40.0
Post-peak nonlinear region factor	dfac	$dfac$	0.3	0.35
Failure strain of element	fail_e	ε^{fail}	N/A	0.35

2.4.2.2 Analysis Parameters.

The material model discussed in paragraph 2.4.2.1 was incorporated into the LS-DYNA FE program through a UMAT definition (subroutine). Important analysis parameters used in single- and multilayer FE models are listed in table 12 and briefly explained below.

- (1) Contact Type

  Automatic contact definition was used to model the contact surfaces in the model. LS-DYNA control card *CONTACT_AUTOMATIC_SURFACE_TO_SURFACE was used. Since the fabric and the steel ring/projectile have large differences in their respective stiffness and mesh densities, the pinball segment-based contact constraint option was used, as recommended by the LS-DYNA Manual [46]. This type of contact is invoked by supplying a value of 2 for the soft variable in the control card, as shown in table 12. With this contact option, the contact stiffness is determined based on the time step and nodal masses. Also, segment versus segment contact is checked rather than node versus segment. After penetrating segments are detected, LS-DYNA designates one segment as the master segment and penalty forces are applied normal to that segment. For the contact between fabric and fabric in the cutout section of the model (see figures 31 and 36), the default method (soft=0) is used. This method uses the size of contact segment and its material properties to determine the contact spring stiffness. As this method depends on the material constants and the size of the segments, it works effectively when the material stiffness parameters between the contacting surfaces are the same order of magnitude. Contact between the fabrics on the ring is modeled using pinball segment-based contact with a soft value of 2, as discussed above. The reason for using this type of contact is that sliding energy values are negative if soft=0 is used. A viscous damping coefficient of 2% of critical was assumed. All other contact parameters were taken as the LS-DYNA default values.

- (2) Coefficient of Friction

  Experimental friction tests of Kevlar 49 showed that the coefficient of static (FS) and dynamic (FD) friction for fabric on fabric was approximately 0.20 [1]. Therefore, a value of 0.2 was used for both FS and FD between the fabric layers. Since there were no experimental friction tests conducted using Kevlar 49 and steel, the FS and FD had to be assumed. Using friction between fabrics as a guide, a value of 0.10 was assumed for both the FS and FD between steel and the fabric.

- (3) Shell Theory

  The shell element formulation theory used was Belytschko-Tsay with one-point Gaussian integration. The shell normal update option was used and the shell element thickness was kept constant during the analysis. All other shell parameters were taken as the default values.

- (4) Hourglass Properties

  For the fabric material, the Flanagan-Belytschko stiffness form was used with an hourglass coefficient of 0.10. For the steel material, the Flanagan-Belytschko viscous form was used with an hourglass coefficient of 0.0.

- (5) Time step and accuracy

  For each analysis, the time step factor used was 0.75. Thus, the actual time step was 75% of the value computed by LS-DYNA. Using this value, no unstable analyses occurred. Second-order stress updates and invariant node numbering of shell elements were also used as specified in the *CONTROL_ACCURACY card in each analysis as recommended by LS-DYNA for high-velocity impact problems.

Table 12. Description of Important Control Parameters Used in Single- and Multilayer Models Developed at ASU

Definition	Single-Layer Model	Multilayer Model
Number of FE layers	1	4 fabric layers are represented by 1 FE layer (i.e., 1x4)
	HOURGLASS	
Fabric		
IHQ	4 (stiffness form hourglass control)	4 (stiffness form hourglass control)
QM	0.1 (hourglass coefficient-default)	0.1 (hourglass coefficient-default)
QB, QW	0.1 (should equal QM)	0.1 (should equal QM)
Metal		
	HOURGLASS	HOURGLASS
IHQ	2 (viscous form hourglass control)	2 (viscous form hourglass control)
QM	0.0 (hourglass coefficient)	0.0 (hourglass coefficient)
IBQ	0 (bulk viscosity type for solids only)	1 (bulk viscosity type for solids only)
QB,QW	0.0 (bending/warping coefficient)	0.0 (bending/warping coefficient)
	CONTACT_AUTOMATIC_SURFACE_TO_SURFACE	
SSTYP	3 (Part ID)	3 (Part ID)
FS	0.1 (between steel and fabric)	0.1 (between steel and fabric) 0.2 (between fabric and fabric)
FD	0.1 (between steel and fabric)	0.1 (between steel and fabric) 0.2 (between fabric and fabric)
DT	1.00E+20	1.00E+20
SFS	1.0 (scale factor on penalty stiffness)	1.0 (scale factor on penalty stiffness)
SFM	1.0 (scale factor on penalty stiffness)	1.0 (scale factor on penalty stiffness)
SFST/SFM	1.0 (default)	1.0 (default)
Card A		
SOFT	2.0 (between steel and fabric)	2.0 (between steel and fabric) 0.0 (between fabrics on ring cutout) 2.0 (between fabrics on the ring)

Table 12. Description of Important Control Parameters Used in Single-Layer and Multilayer Models Developed at ASU (Continued)

Definition	Single-Layer Model	Multilayer Model
	CONTACT_AUTOMATIC_SURFACE_TO_SURFACE (Continued)	
SOFSCL	0.1 (default)	0.1 (default)
IGAP	1	1
	CONTROL_SHELL	
THEORY	2	2
	CONTROL_ENERGY	
HGEN	2 (hourglass energy is computed)	2 (hourglass energy is computed)
SLNTEN	2 (sliding energy is computed)	2 (sliding energy is computed)
	CONTROL_TIMESTEP	
TSSFAC	0.75	0.75

LS-DYNA Model Terms:

IHQ Hourglass control type (LS-DYNA 971 Keyword User's Manual Section 16.1 (HOURGLASS))

QM Hourglass coefficient

IBQ Bulk viscosity type: bulk viscosity is necessary to propagate shock waves in solid materials and therefore applies only to solid elements.

QB Hourglass coefficient for shell bending. The default QB=QM.

QW Hourglass coefficient for shell warping. The default QB=QM.

SSTYP Slave segment or node set type. The type must correlate with the number specified for SSID (Keyword User's Manual Section 7.10 (CONTACT))

FS Static coefficient of friction if FS is >0 and not equal to 2. The frictional coefficient is assumed to be dependent on the relative velocity v_{rel} of the surfaces in contact μ_c=FD + (FS – FD)$e^{-DC|\,vrel\,|}$. (7.12 (CONTACT))

FD Dynamic coefficient of friction if FS is >0 and not equal to 2. The frictional coefficient is assumed to be dependent on the relative velocity v_{rel} of the surfaces in contact μ_c=FD + (FS – FD)$e^{-DC|\,vrel\,|}$. (7.12 (CONTACT))

DT Death time (contact surface is deactivated at this time). DT defaults to 1.0E+20. (7.14 (CONTACT))

SFS Scale factor on default slave penalty stiffness. (7.15 (CONTACT))

SFM Scale factor on default master penalty stiffness. (7.15 (CONTACT))

SFST Scale factor for slave surface thickness (scales true thickness). (7.15 (CONTACT))

SFMT Scale factor for master surface thickness (scales true thickness). (7.15 (CONTACT))

SOFT Soft constraint option: the soft constraint may be necessary if the material constants of the elements which make up the surfaces in contact have a wide variation in the elastic bulk moduli. (7.34 (CONTACT))

SOFSCL Scale factor for constraint forces of soft constraint option (default = 0.10). (7.34 (CONTACT))

IGAP Flag to improve implicit convergence behavior at the expense of creating some sticking if parts attempt to separate. (Implicit only, default = 1.0) (7.39 (CONTACT))

THEORY Default shell theory: EQ.2: Belytschko-Tsay (8.111 (CONTROL))

HGEN Hourglass energy calculation option: EQ.2: hourglass energy is computed and included in the energy balance. (8.40 (CONTROL))

SLNTEN Sliding interface energy dissipation option. This parameter is always set to 2 if contact is active. EQ.2: energy dissipation is computed and included in the energy balance. (8.40 (CONTROL))

TSSFAC Scale factor for computed time step. Default = 0.90; if high explosives are used, the default is lowered to 0.67. (8.133 (CONTROL))

2.4.2.3 Quality Assurance Checks for Simulation.

Quality assurance (QA) checks of FE simulations can be broadly divided into two parts. The first compares model configuration and results against experimental data and the second ensures numerical stability of simulations.

Phase I data were obtained using one high-speed camera, whereas two cameras were used during Phase II. The projectile orientations were not measured in Phase I and qualitative analyses of the photographs were performed to see if the projectile hits were at the desired orientation (0, 0, 0) roll, pitch, and yaw angles. It was observed that at least five test cases, including LG424, LG427, LG432, LG434, and LG449, had nonzero rotational angles. Two of these test cases are shown in figures 76 and 77. The projectile angles in the experiment video and the simulations appear dissimilar because the simulations of these tests were carried out with (0, 0, 0) roll, pitch, and yaw angles. The results are included in the subsequent analyses and discussions.

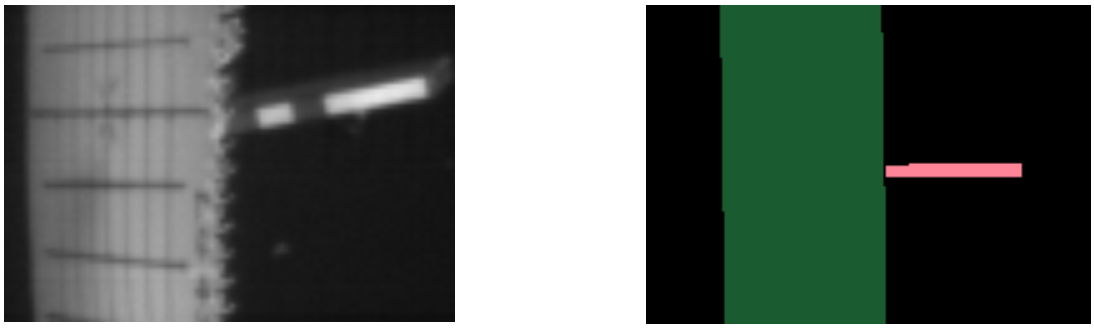

Figure 76. Comparison of Experimental and Simulation Orientation for LG432

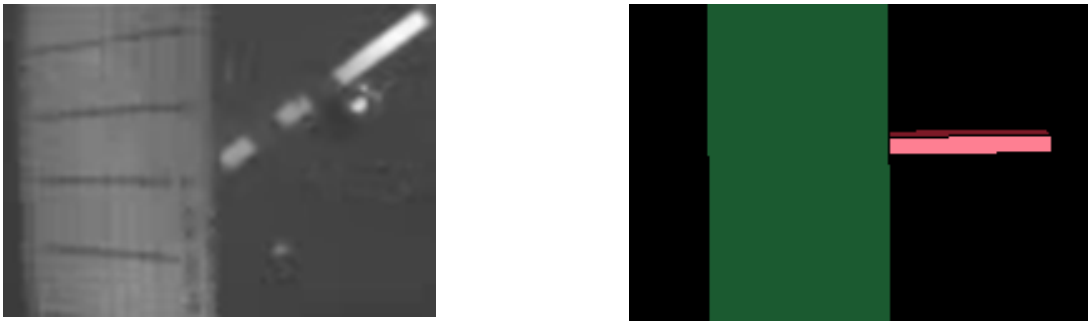

Figure 77. Comparison of Experimental and Simulation Orientation for LG449

The numerical stability during the simulation was ensured by conducting the following checks. A summary of these tests is shown in table 13.

1. The ratio of global kinetic energy/global total energy and global internal energy/global total energy should be less than unity. A ratio of greater than unity indicates the numerical errors.

2. The ratio of global hourglass energy/global total energy and global sliding energy/global total energy should be less than 0.1.

3. Variation in energy ratio should be less than 0.1.

4. Hourglass energy/total energy for the fabric directly in contact with the projectile should be less than 0.1. To compute hourglass energy of fabric directly in contact with projectile, each layer of fabric is modeled using two parts. One part represents the fabric on the ring cutout and the other represents the fabric over the solid ring.

Table 13. Energy Ratios and Values Used for QA Check of Simulations

Column Number	Variable Name		Variable Definition	Acceptable Limit
1	Test case		Test case number	-
2	Fabric layers		Number of fabric layers in the test case	-
3	Minimum energy ratio		Minimum ratio of (current total energy)/ (initial total energy + external work)	>0.90
4	Maximum energy ratio		Maximum ratio of (current total energy)/ (initial total energy + external work)	<1.1
5	Minimum sliding energy ratio		Minimum ratio of (sliding energy)/ (total energy)	>-0.1
6	Maximum sliding energy ratio		Maximum ratio of (sliding energy)/ (total energy)	<0.1
7	Maximum kinetic energy ratio		Maximum ratio of (kinetic energy)/ (total energy)	<1.0
8	Maximum internal energy ratio		Maximum ratio of (internal energy)/ (total energy)	<1.0
9	Hourglass energy ratio	Global	Maximum ratio of (global hourglass energy)/(global total energy)	<0.1
10		Fabric	Maximum ratio of (hourglass energy)/ (total energy) for fabric directly in contact with projectile for single layer model.	<0.1

2.4.3 Single-Layer FE Ballistic Test Simulations.

In this model, only one FE layer is used to represent all the fabric layers.

2.4.3.1 FE Model.

Shell elements were used to represent the fabric, and solid elements were used to represent the steel ring and steel projectiles. The fabric was modeled with a uniform mesh containing 0.25″ shell elements. The steel ring was modeled with 0.25″ by 0.25″ by 1.0″ hexagonal elements (1.0″ through the ring thickness) since the ring was not of interest with respect to the FE analysis

results. One layer of shell elements was used to represent the fabric irrespective of the actual number of fabric layers. Thus for an eight-layer test case, the shell-element thickness was taken as the thickness of one fabric layer multiplied by 8, or 0.011″ x 8 = 0.088″. With this methodology, the friction between the fabric layers is not captured. In the model, the center of the shell elements was placed at a distance of one-half the shell element thickness away from the ring, thereby facilitating contact between the shell elements and the ring at the start of the analysis.

The fabric model was meshed using two different parts. The fabric directly in contact with the penetrator was given a separate part identification than the rest of the fabric. This type of configuration allows the energy balance to be traced separately in this area. Figure 78 shows the typical ring and fabric model used for these simulations.

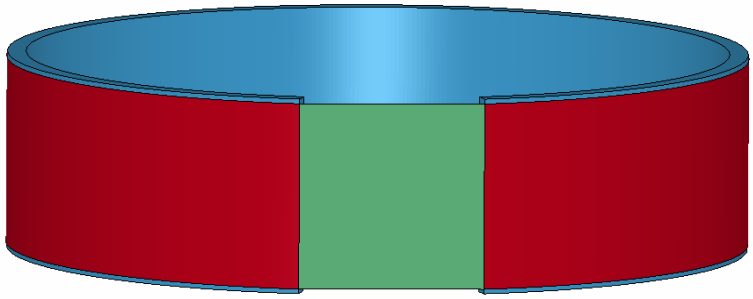

Figure 78. Single-Layer FE Ballistic Test Model

2.4.3.2 Results and Discussion.

Table 14 shows a comparison of results between the absorbed energy during the experiments and its corresponding LS-DYNA simulation.

It should be noted that roll, pitch, and yaw angles for tests LG424, LG427, LG432, LG434, and LG449 were determined not to be (0,0,0) by posttest video analysis; however, simulations for all Phase I tests were set at (0,0,0). Because only one camera was used in Phase I, the actual angles could not be determined. Phase II simulations all used the actual projectile angles in the simulations.

Table 15 shows statistical analysis of the data from table 14 for ASUumatV1.0 and ASUumatV1.1.

Table 14. Comparison of Absorbed Energy (Experimental Ballistic Tests vs FE Single-Layer Simulations)

Test	Fabric Layers	NASA Test						Simulations						% Difference
		Before Impact		After Impact		Absorbed Energy		Before Impact		After Impact		Absorbed Energy		
		Velocity (ft/sec)	Energy (J)	Velocity (ft/sec)	Energy (J)	(J)	%	Velocity (ft/sec)	Energy (J)	Velocity (ft/sec)	Energy (J)	(J)	(%)	
LG403	4	899	11,952	846.5	10,597	999	11.3	899.2	11,852	864.9	10,964	888	7.5	3.8
LG404	8	895.7	11,843	820.2	9,931	1,911	16.1	895.8	11,764	802.7	9,443	2,321	19.7	-3.6
LG405	24	899	11,975	495.4	3,637	6,150	69.6	899.2	11,852	0	0	11,852	100	-30.4
LG409	8	889.1	11,604	807.1	9,562	1,506	17.6	889.2	11,590	797.5	9,324	2,266	19.6	-2
LG410	4	912.1	12,226	866.1	11,026	885	9.8	911.7	12,183	892.4	11,675	508	4.2	5.6
LG411	24	885.8	11,474	413.4	2,499	8,976	78.2	885.8	11,503	495.1	3,604	7,899	68.7	9.6
LG424	8	833.3	10,352	744.8	8,268	1,537	20.1	833.3	10,180	716.1	7,519	2,661	26.1	-6
LG427	24	915.4	12,373	607	5,440	5,113	56	915	12,273	599.9	5,288	6,985	56.9	-0.9
LG429	16	915.4	12,307	718.5	7,583	3,484	38.4	915	12,273	672.8	6,638	5,635	45.9	-7.5
LG432	16	895.7	11,925	649.6	6,273	5,652	47.4	895.8	11,764	651.7	6,234	5,529	47	0.4
LG433	1	390.4	2,242	367.5	1,986	189	11.4	390.4	2,234	274.3	1,104	1,130	50.6	-39.2
LG434	1	383.9	2,162	360.9	1,911	185	11.6	383.8	2,160	312.4	1,431	729	33.8	-22.1
LG444	2	347.8	1,778	277.9	1,135	474	36.1	347.8	1,773	121.7	223	1,549	87.4	-51.2
LG449	2	344.5	1,743	278.9	1,142	443	34.5	344.4	1,739	119.3	215	1,524	87.6	-53.2
LG609	8	913.7	12,110	825.4	9,883	2,228	18.4	914.3	12,169	853.3	10,606	1,564	12.8	5.5
LG610	8	888.1	11,440	809.7	9,510	1,931	16.9	888.4	11,492	789.9	9,108	2,384	20.7	-3.9
LG611	8	905.7	12,348	798.1	9,588	2,760	22.4	905.8	12,026	846.8	10,513	1,513	12.6	9.8
LG612	8	898.3	12,146	822.7	10,190	1,957	16.1	898.3	11,829	803.5	9,466	2,363	20	-3.9
LG618	8	866.4	10,889	558.9	4,531	6,358	58.4	866.8	10,937	470	3,386	7,552	69	-10.7
LG655	32	1131.7	19,281	830.6	10,386	8,895	46.1	1131.7	18,772	1016.6	15,150	3,622	19.3	26.8
LG656	32	967.3	14,086	469.2	3,315	10,771	76.5	967.5	13,721	626.9	5,764	7,956	58	18.5
LG657	32	829.7	10,363	0	0	10,363	100	829.6	10,090	0	0	10,090	100	0
LG692	8	885.3	11,799	602.6	5,466	6,333	53.7	885	11,480	661.3	6,515	4,966	43.3	10.4
LG594	8	843.9	10,147	484.5	3,345	6,802	67	844.3	10,377	368.7	2,217	8,160	78.6	-11.6
LG689	8	896.3	12,061	655.1	6,443	5,618	46.6	896.7	11,785	697.6	7,214	4,571	38.8	7.8
LG620	8	893.8	11,735	580.8	4,954	6,780	57.8	894.3	11,643	670.7	6,647	4,995	42.9	14.9

Table 15. Statistics for Absorbed Energy % Difference Between FE Single-Layer Simulations and Experiments

	ASUumatV1.0			ASUumatV1.1		
	Phase I	Phase II	Overall	Phase I	Phase II	Overall
Number of tests	14	12	26	14	12	26
Average (%)	-13.1	7.0	-3.8	-14.0	5.3	-5.1
Maximum (%)	9.2	29.5	29.5	9.6	26.8	26.8
Minimum (%)	-49.8	-19.1	-49.8	-53.2	-11.6	-53.2
Standard Deviation (%)	19.1	15.4	19.9	21.5	11.7	19.8

To better understand the behavior of the two material model versions with regard to a comparison with ballistic test data from both phases, a series of data analyses were carried out. Table 16 summarizes the results from both versions for test cases where the number of fabric layers is less than or equal to 2.

Table 16. Statistics for Absorbed Energy % Difference Between Simulations and Experiments for Test Cases LG433, LG434, LG444, and LG449

	ASUumatV1.0	ASUumatV1.1
Number of test cases	4	4
Average (%)	-33	-41
Maximum (%)	-17	-22
Minimum (%)	-50	-53
Standard Deviation (%)	18	14

The four test cases with the fewest layers and lowest velocities were poorly simulated by both versions. Table 17 shows the statistics of the results without these four test cases. As the results show, ASUumatV1.1 shows an overall improvement in the results compared to ASUumatV1.0.

Table 17. Statistics for Absorbed Energy % Difference Between Simulations and Experiments Without Test Cases LG433, LG434, LG444, and LG449

	ASUumatV1.0	ASUumatV1.1
Number of test cases	22	22
Average (%)	2	1
Maximum (%)	29	27
Minimum (%)	-30	-30
Standard Deviation (%)	15	12

2.4.4 The QA Check Using Energy Ratios.

The QA checks for the energy ratios are shown in table 18. It can be observed that these ratios are well within the expected range, except for 2 (LG405 and LG657) of the 26 test cases where the hourglass energy is observed to be higher than 10% of total energy. These cases involve (simulation) contained projectiles, and high hourglass energy was observed when projectile velocity neared zero. When the time period near the end of the simulation is removed from the analysis, the hourglass energy values are in the acceptable range.

Table 18. The QA Check of Single-Layer FE Models

Test Case	Fabric Layers	Minimum Energy Ratio	Maximum Energy Ratio	Minimum Sliding Energy Ratio	Maximum Sliding Energy Ratio	Maximum Kinetic Energy Ratio	Maximum Internal Energy Ratio	Hourglass Energy Ratio —Global	Hourglass Energy Ratio —Fabric
LG403	4	1	1	0	0.0014	1	0.016	0.0009	0.0193
LG404	8	0.9999	1.0001	0	0.0055	1	0.0488	0.0044	0.0179
LG405	24	1	1.0389	0	0.079	1	0.2418	0.1344	0.1544
LG409	8	0.9997	1	0	0.0051	1	0.0469	0.0041	0.0186
LG410	4	0.9999	1	0	0.001	1	0.0091	0.0011	0.0339
LG411	24	0.9988	1	0	0.018	1	0.2087	0.0408	0.0713
LG424	8	0.9993	1.0005	0	0.0072	1	0.0662	0.006	0.0267
LG427	24	0.9978	1	0	0.0143	1	0.1667	0.0475	0.0804
LG429	16	0.9987	1.0001	0	0.0114	1	0.1148	0.0166	0.0311
LG432	16	0.9983	1.0001	0	0.0136	1	0.1212	0.0186	0.0349
LG433	1	0.9986	1.0002	-0.008	0.0057	1	0.2833	0.0144	0.0603
LG434	1	0.9998	1	0	0.0067	1	0.1606	0.009	0.0094
LG444	2	0.9962	1.0003	0	0.0622	1	0.5478	0.0216	0.0168
LG449	2	0.9994	1.0008	0	0.0444	1	0.6823	0.02	0.0547
LG594	8	0.9988	1.1794	0	0.0562	1	0.2218	0.0588	0.0668
LG609	8	0.999	1	0	0.0015	1	0.0332	0.0031	0.025
LG610	8	0.9996	1.0001	0	0.0029	1	0.0458	0.0033	0.02
LG611	8	0.9997	1	0	0.0028	1	0.0305	0.003	0.0303
LG612	8	0.9995	1.0001	0	0.0052	1	0.0497	0.0056	0.0246
LG618	8	0.9999	1.0199	0	0.0413	1	0.1861	0.0533	0.0495
LG620	8	0.9988	1.0047	-0.0006	0.0129	1	0.1089	0.036	0.0383
LG655	32	0.9991	1	0	0.0036	1	0.0478	0.0078	0.0601
LG656	32	0.9961	1	0	0.0302	1	0.1594	0.0673	0.064
LG657	32	1	1.0021	0	0.063	1	0.3518	0.1146	0.3037
LG689	8	0.9985	1.0001	0	0.011	1	0.0773	0.0204	0.0525
LG692	8	0.9962	1.0001	0	0.0096	1	0.082	0.0281	0.0507

2.4.5 Multilayer FE Ballistic Test Simulation.

Using a single-layer FE to represent all the fabric layers loses the model resolution that is needed to see how the fabric containment system responds to the projectile hit. For example, if 24 fabric layers make up the containment system and the projectile is contained, the single-layer model

does not have the resolution to show how much of the fabric system is damaged and how much is intact. A multilayer FE model can provide the answer to this question and more.

2.4.5.1 The FE Model.

In this multilayer model, one layer of shell elements was used to represent the four fabric layers. Thus for an eight-fabric layer test case, there are two FE layers. Each FE shell element is four times as thick as one fabric layer, or 0.011″ x 4 = 0.044″. With this methodology, the friction between the fabric layers can also be captured.

In the model, the center of the shell element was placed at a distance of one-half the shell element thickness away from the ring and one shell element away from the adjacent shell layer to facilitate contact between them at the start of the analysis. Figure 79 shows the FE model of the ring and the fabric for 16 fabric layers that was modeled using a four-layer FE model.

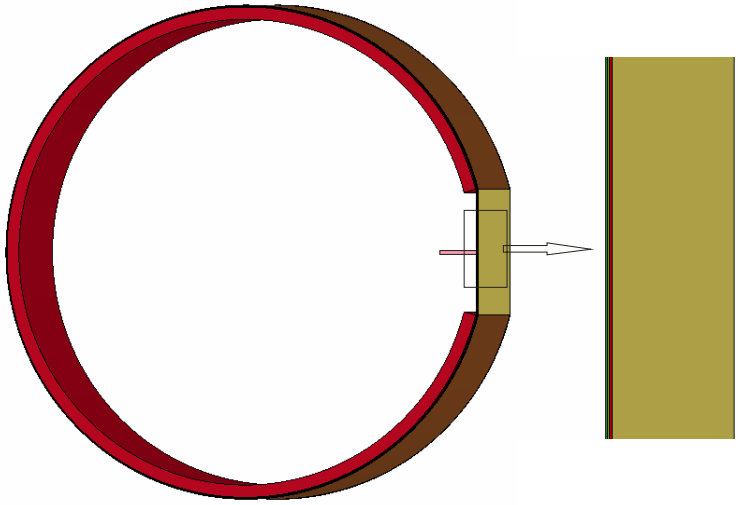

Figure 79. Multilayer FE Ballistic Test Model

2.4.5.2 Results and Discussion.

Table 19 shows a comparison between the absorbed energy of the fabric for each experimental test case and its corresponding LS-DYNA simulation.

Table 19. Comparison of Absorbed Energy (Experimental Ballistic Tests vs FE Multilayer Simulations)

File Run	Fabric Layers	NASA Test						Simulation						% Difference
		Before Impact		After Impact		Absorbed Energy		Before Impact		After Impact		Absorbed Energy		
		Velocity (ft/sec)	Energy (J)	Velocity (ft/sec)	Energy (J)	(J)	%	Velocity (ft/sec)	Energy (J)	Velocity (ft/sec)	Energy (J)	(J)	(%)	
LG404	8	895.7	11,843	820.2	9,931	1,911	16.1	895.8	11,764	805.1	9,505	2,259	19.2	-3.1
LG405	24	899	11,975	495.4	3,637	6,150	69.6	899.2	11,852	560.2	4,613	7,239	61.1	8.5
LG409	8	889.1	11,604	807.1	9,562	1,506	17.6	889.2	11,590	795.4	9,276	2,314	20	-2.4
LG411	24	885.8	11,474	413.4	2,499	8,976	78.2	885.8	11,503	526.1	4,077	7,426	64.6	13.7
LG424	8	833.3	10,352	744.8	8,268	1,537	20.1	833.3	10,180	733.6	7,891	2,289	22.5	-2.4
LG427	24	915.4	12,373	607	5,440	5,113	56	915	12,273	647.8	6,159	6,114	49.8	6.2
LG429	16	915.4	12,307	718.5	7,583	3,484	38.4	915	12,273	806.7	9,536	2,737	22.3	16.1
LG432	16	895.7	11,925	649.6	6,273	5,652	47.4	895.8	11,764	679.6	6,778	4,986	42.4	5
LG609	8	913.7	12,110	825.4	9,883	2,228	18.4	914.3	12,169	881.5	11,316	853	7	11.4
LG610	8	888.1	11,440	809.7	9,510	1,931	16.9	888.4	11,492	802.7	9,388	2,104	18.3	-1.4
LG611	8	905.7	12,348	798.1	9,588	2,760	22.4	905.8	12,026	838.8	10,317	1,709	14.2	8.1
LG612	8	898.3	12,146	822.7	10,190	1,957	16.1	898.3	11,829	799.9	9,385	2,444	20.7	-4.6
LG618	8	866.4	10,889	558.9	4,531	6,358	58.4	866.8	10,937	0	0	10,937	100	-41.6
LG655	32	1131.7	19,281	830.6	10,386	8,895	46.1	1131.7	18,772	1020.7	15,273	3,499	18.6	27.5
LG656	32	967.3	14,086	469.2	3,315	10,771	76.5	967.5	13,721	447	3,184	10,537	76.8	-0.3
LG657	32	829.7	10,363	0	0	10,363	100	829.6	10,090	0	0	10,090	100	0
LG692	8	885.3	11,799	602.6	5,466	6,333	53.7	885	11,480	768.5	8,681	2,799	24.4	29.3
LG594	8	843.9	10,147	484.5	3,345	6,802	67	844.3	10,377	504.5	3,766	6,611	63.7	3.3
LG689	8	896.3	12,061	655.1	6,443	5,618	46.6	896.7	11,785	745.5	8,172	3,613	30.7	15.9
LG620	8	893.8	11,735	580.8	4,954	6,780	57.8	894.3	11,643	632.4	5,947	5,696	48.9	8.9

Table 20 shows the results of the statistical analysis using the data from table 19.

Table 20. Statistics for Absorbed Energy % Difference Between Multilayer Simulations and Experiments

	ASUumatV1.1		
	Phase I	Phase II	Overall
Number	8	12	20
Average (%)	5.2	4.7	4.9
Maximum (%)	16.1	29.3	29.3
Minimum (%)	-3.1	-41.6	-41.6
Standard Deviation (%)	7.4	18.2	14.6

ASUumatV1.1 showed a better performance (prediction) with Phase I models over Phase II models. It is believed this is mainly because in Phase I, the projectile hits were straight hits (zero roll, pitch, and yaw angles). In Phase II, the projectile-fabric interaction was much more complicated since the roll, pitch, and yaw angles were nonzero before and after the projectile made contact with the fabric. Nevertheless, apart from three tests (LG618, LG692, and LG655), the FE simulations showed very good correlation with experimental results.

2.4.5.3 The QA Check.

Different energy ratios are shown in table 21. Overall, it was observed that these ratios were well within the expected range, except for 2 of 20 test cases in which the hourglass energy was observed to be higher than 10% of the total energy. A detailed study of these test cases revealed that test cases LG618 and LG657 were special, because the projectile was contained in the simulations. In these test cases, high hourglass energy was observed when projectile velocity was near zero. It can be concluded that the energy ratios for multilayer FE models were satisfactory.

Table 21. The QA Check of Multilayer FE Models

Test Case	Fabric Layers	Minimum Energy Ratio	Maximum Energy Ratio	Minimum Sliding Energy Ratio	Maximum Sliding Energy Ratio	Maximum Kinetic Energy Ratio	Maximum Internal Energy Ratio	Hourglass Energy Ratio								
								Global	First FE Layer	Second FE Layer	Third FE Layer	Fourth FE Layer	Fifth FE Layer	Sixth FE Layer	Seventh FE Layer	Eighth FE Layer
LG404	8	0.9998	1	0	0.004	1	0.047	0.003	0.015	0.024	0	0	0	0	0	0
LG405	24	0.9987	1	-0.011	0.016	1	0.203	0.027	0.042	0.058	0.045	0.035	0.037	0.035	0	0
LG409	8	0.9995	1	0	0.006	1	0.053	0.004	0.021	0.013	0	0	0	0	0	0
LG411	24	0.9987	1.0001	-0.008	0.016	1	0.202	0.024	0.039	0.036	0.039	0.027	0.03	0.027	0	0
LG424	8	0.9995	1	0	0.006	1	0.061	0.005	0.02	0.018	0	0	0	0	0	0
LG427	24	0.9977	1	-0.006	0.012	1	0.149	0.016	0.045	0.041	0.024	0.022	0.023	0.024	0	0
LG429	16	0.9996	1	0	0.009	1	0.052	0.003	0.015	0.021	0.021	0.028	0	0	0	0
LG432	16	0.9989	1.0001	0	0.013	1	0.118	0.014	0.046	0.029	0.023	0.023	0	0	0	0
LG594	8	0.9997	1.0041	-0.001	0.031	1	0.172	0.037	0.038	0.043	0	0	0	0	0	0
LG609	8	0.9999	1	0	0	1	0.006	0	0.022	0.018	0	0	0	0	0	0
LG610	8	1	1	0	0.002	1	0.035	0.003	0.021	0.015	0	0	0	0	0	0
LG611	8	0.9995	1	0	0.004	1	0.032	0.002	0.028	0.033	0	0	0	0	0	0
LG612	8	0.9999	1.0001	0	0.004	1	0.042	0.002	0.018	0.015	0	0	0	0	0	0
LG618	8	1	1.0332	-0.013	0.057	1	0.521	0.079	0.459	0.173	0	0	0	0	0	0
LG620	8	0.9997	1.0021	0	0.026	1	0.115	0.024	0.033	0.022	0	0	0	0	0	0
LG655	32	0.9979	1	0	0.018	1	0.053	0.003	0.099	0.04	0.038	0.018	0.025	0.02	0.022	0.023
LG656	32	0.9996	1.0091	-0.062	0.034	1	0.264	0.032	0.081	0.072	0.106	0.043	0.063	0.068	0.073	0.078
LG657	32	0.9996	1.0144	-0.274	0.027	1	0.506	0.058	0.142	0.115	0.109	0.107	0.154	0.159	0.145	0.157
LG689	8	0.9991	1.0014	0	0.015	1	0.065	0.011	0.024	0.025	0	0	0	0	0	0
LG692	8	0.9995	1.0001	0	0.006	1	0.057	0.01	0.048	0.02	0	0	0	0	0	0

2.4.6 Regression Model.

To better understand the effect of various model parameters on the simulation results, a regression analysis was performed on the data obtained from single- and multilayer models [47]. A total of six predictor variables were considered, which included four quantitative variables: velocity of the projectile; number of fabric layers in the model; roll, pitch, and yaw angles for projectile orientation; and one categorical variable—type of projectile. The difference between the percentage energy absorbed in simulation and experiment, as shown in equation 21, was considered as the response variable. In general, the regression equation can be represented as

$$y_i = \beta_0 + \beta_1 x_{i1} + \beta_2 x_{i2} + ... + \beta_k x_{ik} + \varepsilon_i,\ i = 1, 2, ..., n \tag{21}$$

where y is response variable, x_i represents the regressors, and β represents regression coefficients. In equation 21, units of predictor variables are different, which makes direct comparison of regression coefficients difficult. To allow direct comparison of regression coefficients, the regression analysis was performed on scaled regressors and response variables that produce dimensionless regression coefficients (table 22).

Table 22. Comparison Between Experiments and FE Simulations for Single- and Multilayer Models

Model	Experiment Absorbed Energy (%)	Single-Layer Model Absorbed Energy (%)	D (%)	Multilayer Model Absorbed Energy (%)	D (%)
LG403	11.3	7.5	3.8	-	-
LG410	9.8	4.1	5.7	-	-
LG404	16.1	19.7	-3.6	21.5	-1.8
LG409	17.6	19.6	-2.0	19.0	-1.4
LG424	20.1	26.1	-6.0	20.5	-0.4
LG609	18.4	12.9	5.5	7.7	10.7
LG610	16.9	20.8	-3.9	17	-0.1
LG611	22.4	12.6	9.8	13.3	9.1
LG612	16.1	20.0	-3.9	19.2	-3.1
LG692	53.7	43.3	10.4	25.6	28.1
LG594	67.0	78.6	-11.6	53.9	13.1
LG689	46.6	38.8	7.8	31.1	15.5
LG620	57.8	42.9	14.9	52.7	5.1
LG429	38.4	45.9	-7.5	20.7	17.7
LG432	47.4	47.0	0.4	35.7	11.7
LG411	78.2	68.6	9.6	53.5	24.7
LG427	56.0	56.9	-0.9	57.7	-1.7

Table 22. Comparison Between Experiments and FE Simulations for Single- and Multilayer Models (Continued)

Model	Experiment Absorbed Energy (%)	Single-Layer Model Absorbed Energy (%)	D (%)	Multilayer Model Absorbed Energy (%)	D (%)
LG655	46.1	19.3	26.8	19.7	26.4
LG656	76.5	58	18.5	76.6	-0.1
LG657	100.0	100	0	100	0
Average			3.7		8.5
Minimum			-11.6		-3.1
Maximum			26.8		28.1
Standard deviation			9.5		10.5

In this analysis, unit normal scaling was used to obtain standardized regression coefficients. In this method, all regressors and response variables are scaled by first subtracting mean of the variable from each data point and dividing this quantity by standard deviation of the variable, as shown in equations 22 and 23.

$$z_{ij} = \frac{x_{ij} - \overline{x_j}}{s_j},\ i = 1,2,...,n\ \ j = 1,2,...,k \tag{22}$$

$$y_i^* = \frac{y_i - \overline{y}}{s_y},\ i = 1,2,...,n \tag{23}$$

where

$$s_j^2 = \frac{\sum_{i=1}^{n}\left(x_{ij} - \overline{x_j}\right)^2}{n-1} \tag{24}$$

is the sample variance of regressor x_j and

$$s_y = \frac{\sum_{i=1}^{n}\left(y_i - \overline{y}\right)^2}{n-1} \tag{25}$$

is the sample variance of the response.

This method of standardization provides scaled regressors and response variables that have sample mean equal to zero and sample variance equal to 1. Using these new variables, the regression model becomes

$$y_i^* = b_1 z_{i1} + b_2 z_{i2} + ... + b_k z_{ik} + \varepsilon_i,\ i = 1, 2, ..., n \tag{26}$$

Centering the regressor and response variables by subtracting $\overline{x_j}$ and $\overline{y}$ removes the intercept from the model. Variables used in the regression analysis are shown in table 23.

Table 23. List of Predictors and Response Variables Used in Regression Analysis

Variable Type	Term	Notation	Description
Predictor	Penetrator type	PT	0 - Thick penetrator (Old)
			1 - Thin penetrator (New)
Predictor	Roll	R	Projectile roll angle (degrees)
Predictor	Pitch	P	Projectile pitch angle (degrees)
Predictor	Yaw	Y	Projectile yaw angle (degrees)
Predictor	# Fabric layers	FL	Number of fabric layers
Predictor	Velocity	V	Penetrator velocity (ft/s)
Response	% Difference	D	Absorbed energy percent difference (see equation 20)

2.4.6.1 Single-Layer Model.

A scatter plot of response variable versus all predictor variables is shown in figure 80. The regression equation obtained for standardized variables in shown in equation 27.

$$\begin{aligned} D = &-0.195PT + 0.011R - 0.493P + 0.191Y - 0.044FL + 0.144V \\ &+ 0.524R^2 + 0.610FL^2 \end{aligned} \tag{27}$$

From the scatter plot and the regression equation, it is evident that there is a nonlinear relation between absorbed energy and number of fabric layers and roll angle. The absorbed energy difference is the largest in models with the largest number of fabric layers (LG655 and LG656). With all other model parameters being held constant, one would expect a single-layer shell model to perform increasingly worse with increasing shell thickness. The effect of velocity is somewhat difficult to gage due to the lack of data for varying velocities since most of the velocities are in the 800-950 ft/s range. The penetrator type and the yaw angle appear to have the least effect on the difference value. The R^2 of this regression equation is 82.3%.

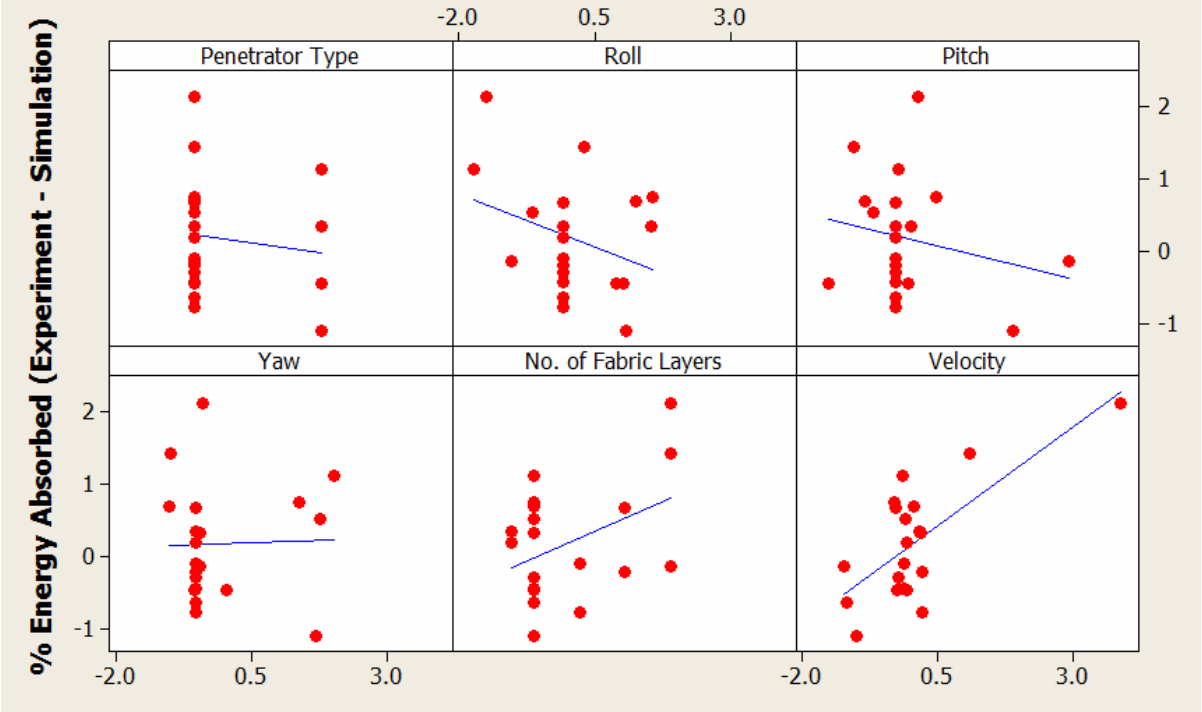

Figure 80. Scatter Plot for Single-Layer Model

2.4.6.2 Multilayer Model.

A scatter plot of response variable versus all predictor variables is shown in figure 81. The regression equation obtained for standardized variables is given in equation 28.

$$D = -0.466PT + 0.317R + 0.357P + 0.541Y + 3.76FL + 0.623V + 0.339R^2 - 3.80FL^2 \quad (28)$$

From the scatter plot and the regression equation, it is evident that there is a nonlinear relation between absorbed energy and number of fabric layers and roll angle. The response variable in this case is largely dependent on the number of fabric layers followed by velocity and projectile orientation. Once again, the effect of velocity is somewhat difficult to gage due to the lack of data for varying velocities. The R^2 of this regression equation is 70.5%, which is noticeably lower than the corresponding figure for the single-layer FE model. The scatter plots show that it is difficult to discern a pattern between the response and the predictor variables—this indicates that the difference in the absorbed energy is less influenced by the predictor variables. This may be due to the fact that interaction between the layers is being accounted for in this model.

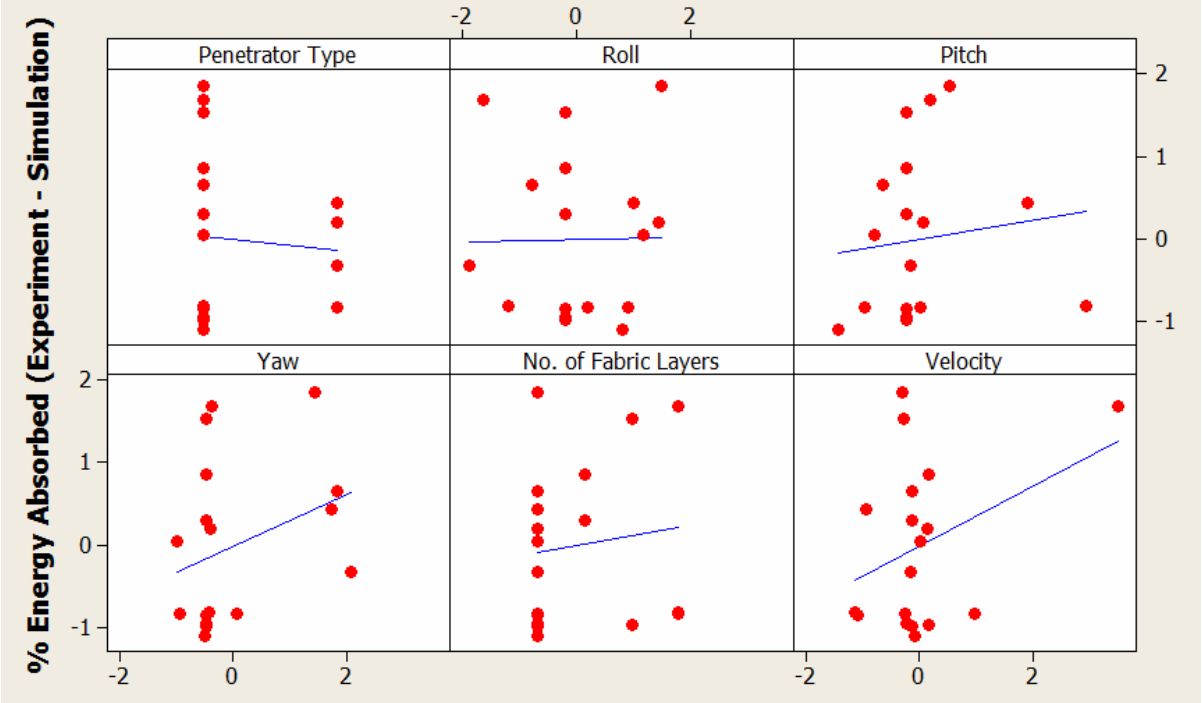

Figure 81. Scatter Plot for Multilayer Model

2.5 MICROMECHANICAL MODEL OF KEVLAR.

Continuing with the evolutionary development of the material model, in this section, a micromechanical model is discussed. This model is used to study the behavior of fabric swaths involving warp and fill yarns.

2.5.1 Introduction.

The two material models (ASUumatV1.0 and ASUumatV1.1) presented earlier were developed based on a continuum shell model. The continuum shell model can predict overall deformation and energy absorption by the fabric before failure. However, it lacks the resolution that is needed to explain or capture the failure pattern at the yarn level. A micromechanical model can overcome these drawbacks as it can predict the actual deformation and reorientation pattern of fabric yarns under different loading and boundary conditions. A micromechanical approach can also be used to estimate material properties that are difficult to compute by experimentation. This approach can be used to understand the behavior of Kevlar fabric under different conditions.

The development process starts with building a 3D model of Kevlar yarns based on actual measurements of geometry parameters (obtained via photomicrographs of sectioned fabric) and combining it with a material model, which is based on yarn level laboratory tests [41]. This implies that 3D FEs (hexahedron and tetrahedron) are used instead of shell element.

2.5.2 Geometric Model.

2.5.2.1 Unit Cell Development.

A Kevlar fabric model can be built by replicating the smallest unit known as a unit cell. The unit cell model of the Kevlar was developed using the geometric parameters computed from sectioned Kevlar. The geometric parameters associated with undeformed geometry were used to build initial or undeformed geometry. The fill and warp direction yarns were assumed to have an elliptical cross-section, which follows a sinusoidal path. The computed parameters associated with Kevlar geometry are shown in table 24.

Table 24. Geometry Parameters

	Transverse Cross-Section/ Elliptical Cross-Section		Longitudinal Cross-Section/ Sinusoidal Path	
	Semi-Major Axis a (in.)	Semi-Minor Axis b (in.)	Period (in.)	Amplitude (in.)
Warp yarn	0.02584	0.003345	0.117981	0.004316
Fill yarn	0.023059	0.003511	0.117415	0.003405

The parameters shown in table 24 were used to build a 3D model of a unit cell (figure 82). An elliptical curve representative of a yarn transverse cross-section was first modeled using semi-minor and semi-major axis dimensions (specified on the dark-shaded area). The elliptical model was then extruded (arrow shows direction of extrusion) along the sinusoidal path represented by amplitude and period values. As shown in table 24, the geometric dimensions of yarn are essentially direction-dependent. Unigraphics NX Geometric Modeler (UG NX) software was used to build the geometric modeling of the yarns.

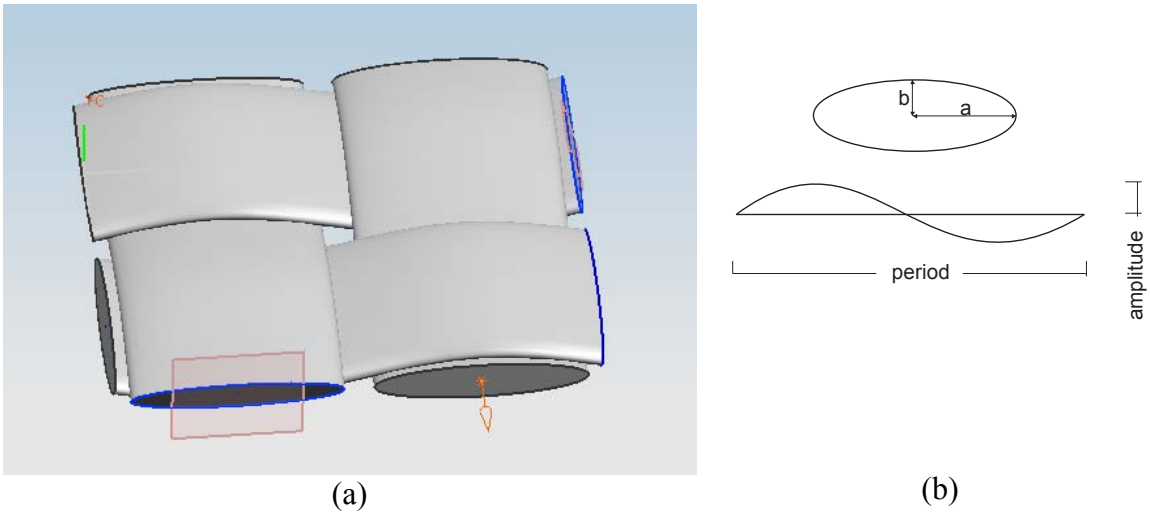

(a) (b)

Figure 82. (a) Unit Cell Model Made up of Two Warp and Two Fill Yarn Segments and (b) Definitions of Semi-Major, Semi-Minor, Period, and Amplitude

It is important to ensure that initial geometry does not have intersecting bodies or surfaces. Initial penetrating surfaces results in undue interfacial stresses and can lead to an unstable model during simulations. The unit cell model developed using the above methodology was checked for penetrations. Initial penetration was removed by modifying the cross-section and sinusoidal curve parameters. The modified geometric parameters are shown in table 25.

Table 25. Modified Geometry Parameters

	Transverse Cross-Section/ Elliptical Cross-Section		Longitudinal Cross-Section/ Sinusoidal Path	
	Semi-Major Axis a (in.)	Semi-Minor Axis b (in.)	Period (in.)	Amplitude (in.)
Warp Yarn	0.02580	0.00334	0.11798	0.00481
Fill Yarn	0.02304	0.00351	0.11742	0.00380

2.5.2.2 Swath Model Generation.

A swath model can be generated by replicating a unit cell (figure 82) in the warp and fill directions. The number of warp and fill direction unit cells can be computed by dividing the required length by the period of the unit cell in this direction. The swath model that was created is shown in figure 83. It is made up of eight unit cells—four unit cells long in the warp direction and two unit cells long in the fill direction.

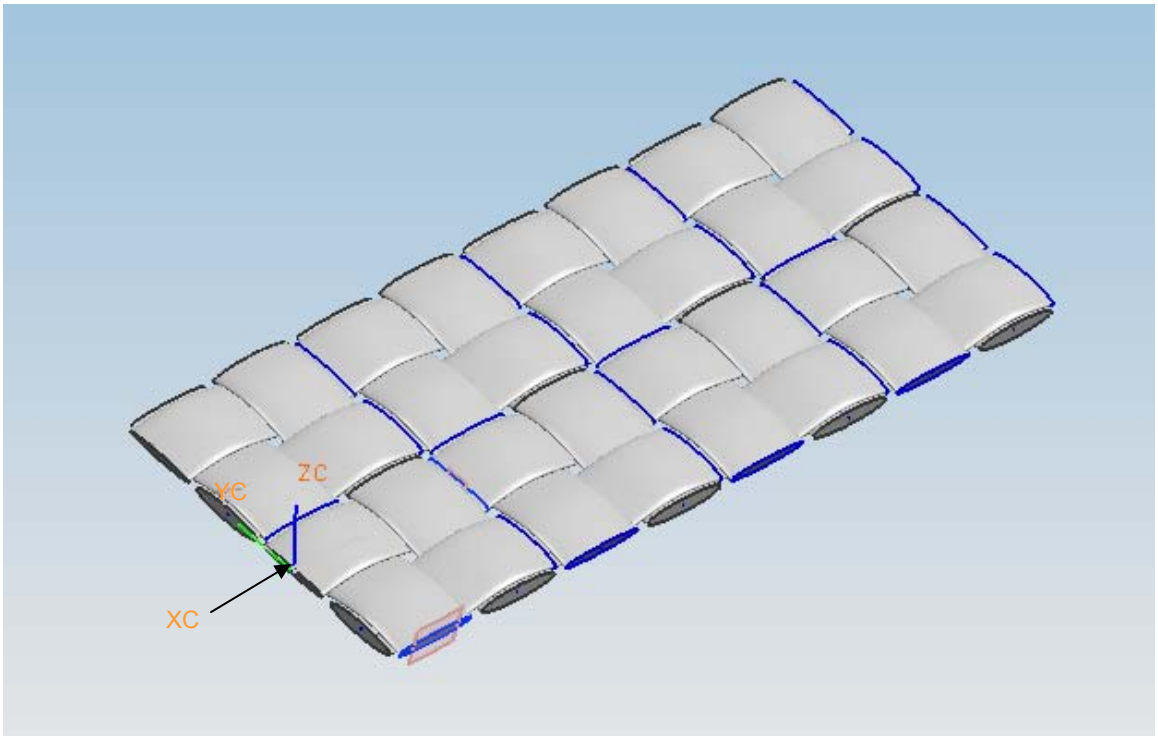

Figure 83. Swath Model Assembled From Unit Cells

2.5.3 Material Model Description.

2.5.3.1 Kevlar Yarn Constitutive Behavior.

The constitutive model that most accurately describes the yarn's behavior is orthotropic. The constitutive relation of Kevlar yarns can be represented as shown in equation 29. The inverse constitutive law, which relates stress increments in terms of strain increments, can be represented by equation 30.

$$\begin{bmatrix} \Delta\varepsilon_{11} \\ \Delta\varepsilon_{22} \\ \Delta\varepsilon_{33} \\ \Delta\varepsilon_{23} \\ \Delta\varepsilon_{31} \\ \Delta\varepsilon_{23} \end{bmatrix} = \begin{bmatrix} \frac{1}{E_1} & \frac{-\nu_{21}}{E_2} & \frac{-\nu_{31}}{E_3} & 0 & 0 & 0 \\ \frac{-\nu_{12}}{E_1} & \frac{1}{E_2} & \frac{-\nu_{32}}{E_3} & 0 & 0 & 0 \\ \frac{-\nu_{13}}{E_1} & \frac{-\nu_{23}}{E_2} & \frac{1}{E_3} & 0 & 0 & 0 \\ 0 & 0 & 0 & \frac{1}{2G_{23}} & 0 & 0 \\ 0 & 0 & 0 & 0 & \frac{1}{2G_{31}} & 0 \\ 0 & 0 & 0 & 0 & 0 & \frac{1}{2G_{12}} \end{bmatrix} \begin{bmatrix} \Delta\sigma_{11} \\ \Delta\sigma_{22} \\ \Delta\sigma_{33} \\ \Delta\sigma_{21} \\ \Delta\sigma_{31} \\ \Delta\sigma_{12} \end{bmatrix} \tag{29}$$

$$\begin{bmatrix} \Delta\sigma_{11} \\ \Delta\sigma_{22} \\ \Delta\sigma_{33} \\ \Delta\sigma_{23} \\ \Delta\sigma_{31} \\ \Delta\sigma_{12} \end{bmatrix} \begin{bmatrix} \frac{1-\nu_{23}\nu_{32}}{E_2E_3c} & \frac{\nu_{21}+\nu_{31}\nu_{23}}{E_2E_3c} & \frac{\nu_{31}+\nu_{21}\nu_{32}}{E_2E_3c} & 0 & 0 & 0 \\ \frac{\nu_{12}+\nu_{13}\nu_{32}}{E_3E_1c} & \frac{1-\nu_{13}\nu_{31}}{E_1E_3c} & \frac{\nu_{32}+\nu_{31}\nu_{12}}{E_3E_1c} & 0 & 0 & 0 \\ \frac{\nu_{13}+\nu_{12}\nu_{23}}{E_1E_2c} & \frac{\nu_{23}+\nu_{13}\nu_{21}}{E_1E_2c} & \frac{\nu_{23}+\nu_{12}\nu_{21}}{E_1E_2c} & 0 & 0 & 0 \\ 0 & 0 & 0 & 2G_{23} & 0 & 0 \\ 0 & 0 & 0 & 0 & 2G_{31} & 0 \\ 0 & 0 & 0 & 0 & 0 & 2G_{12} \end{bmatrix} \begin{bmatrix} \Delta\varepsilon_{11} \\ \Delta\varepsilon_{22} \\ \Delta\varepsilon_{33} \\ \Delta\varepsilon_{23} \\ \Delta\varepsilon_{31} \\ \Delta\varepsilon_{12} \end{bmatrix} \tag{30}$$

where

$$c = \frac{1-\nu_{12}\nu_{21}-\nu_{23}\nu_{32}-\nu_{31}\nu_{13}-2\nu_{12}\nu_{23}\nu_{31}}{E_1E_2E_3} \tag{31}$$

Material direction 11 refers to the main longitudinal direction of the yarn or direction perpendicular to material isotropy; directions 22 and 33 refer to the perpendicular longitudinal direction, i.e., these directions represent material isotropy. The values for E_{11} were computed

using single-yarn tensile tests while other material constants were based on literature values or assumptions. The determination of these material properties will be discussed in the following sections.

2.5.3.2 Determination of E_{11}.

To determine yarn's stress-strain behavior in the principal material direction, experimental tests were conducted at ASU. Additionally, strain rate effects on this behavior were based on published experimental results. From the single-yarn, quasi-static tension tests conducted at ASU, it was determined that the yarn had three distinct regions during loading: (1) an initial region of low stiffness resulting from the low stress required to straighten the yarns, (2) a region of high stiffness where low strain increases result in large stress increases (or elastic region), and (3) a region of negative stiffness where the stress decreases rapidly with an increase in strain (or post-peak or softening region). Stress-strain curves for single-yarn tests (warp yarns) are shown in figure 84. The stiffness, peak stress, and strain at peak stress are gage-length-dependent. The yarn test results, corresponding to the 17-in. gage length (G.L.) were used in the determination of stiffness values.

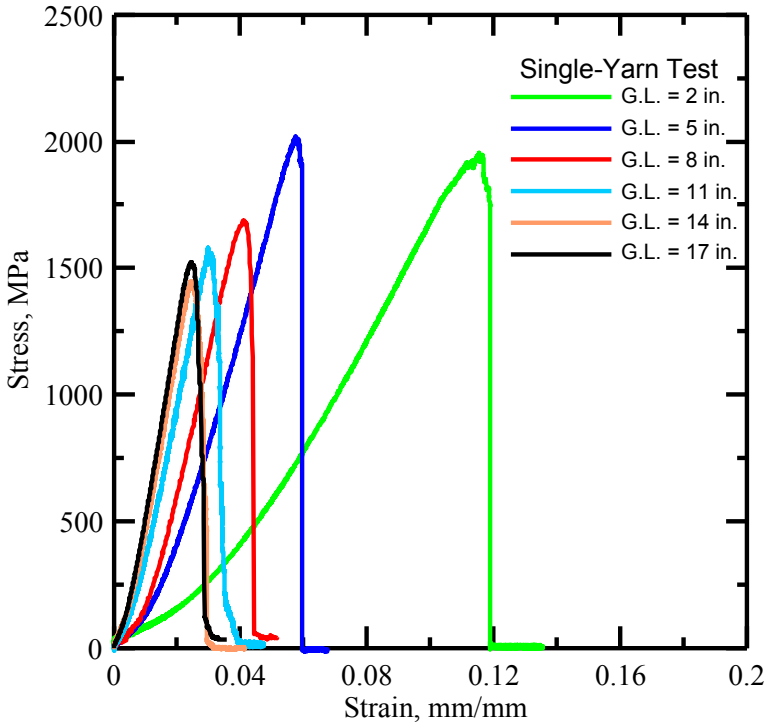

Figure 84. Stress vs Strain Curves of Single-Yarn Tensile Tests for Different G.L.s

2.5.3.2.1 Pre-Peak Behavior in Material Model.

Experimental test results show the behavior of the fabric to be nonlinear. It was observed that the initial nonlinear region was very small for specimens with a 17-in. G.L., which is caused by the initial straightening of the test fixture and some undulations present in the yarn sample. This initial crimp is ignored when computing the stiffness for a solid element representing yarn. The

modified stress-strain curves (after removing crimp) are shown in figure 85. As shown, the pre-peak response can be reasonably approximated by a linear function. A linear fitted curve used to represent material model is also shown along with the tension test results.

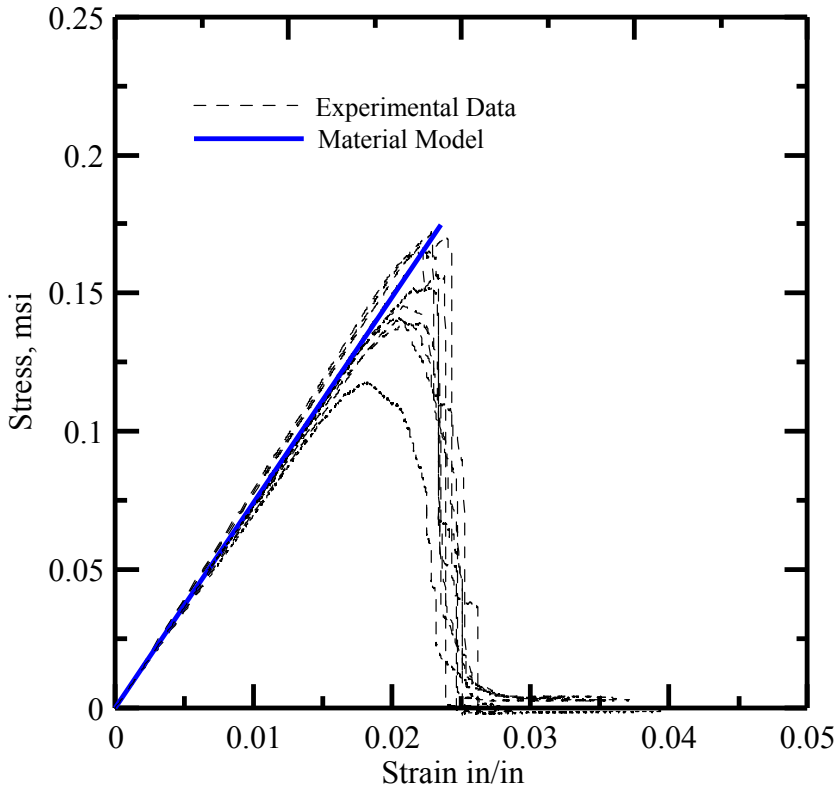

Figure 85. Kevlar Warp Yarn Experimental Stress-Strain Curves With Linear Approximation

The linear approximation was constructed as follows. First, the crimp region from the experimental curves was removed by extending the elastic region backward until it intersected the x axis and shifted the end to the origin. Next, the strain at peak stress and peak stress were chosen by identifying those values for each test and computing the average value. The final values used in the material model to describe the warp direction pre-peak behavior were strain to peak stress (ε_{11}^{max}) of 0.024 and an elastic stiffness (E_{11}) of 7.42(10^6) psi. Because long fill yarns were unavailable, tests were not performed, and the material constants were assumed to be the same as the warp yarns.

2.5.3.2.2 Post-Peak and Failure Behavior in Material Model.

During the test, it was observed that the yarn can experience strains larger than the last reported strain value from the test results. Testing was terminated when the load-carrying capacity of the yarn was very small. To simplify and simulate this in the material model, the post-peak region was approximated with a linear region followed by a nonlinear region up to fabric failure. The linear post-peak region stiffness was determined by fitting a linear curve to the experimental results. It was found that the linear region post-peak stiffness was approximately -2.5 times the elastic stiffness. Thus, the linear region stiffness (E_{11}^{soft}) was -18.55(10^6) psi. A level of strain

or stress had to be assumed for where the nonlinear post-peak region began. In the material model, it was assumed that if the stress was less than 5000 psi, then the stress-strain response was in the post-peak nonlinear region in that respective direction. The stress in the nonlinear region was assumed as follows.

$$\sigma_{11} = \sigma^* \left(1 - \left(\frac{\varepsilon_{11} - \varepsilon_{11}^*}{\varepsilon_{fail} - \varepsilon_{11}^*} \right)^{dfac} \right) \tag{32}$$

In the above equation, σ^* and ε^* are the stress and strain values at which the nonlinear region begins in each respective direction, ε_{fail} is the failure strain in each respective direction, and *dfac* is a factor that specifies the rate of decrease in stress. The values for ε^* were computed in the subroutine. The values for failure strain and the factor *dfac* was considered to be 0.2. Figure 86 shows the stress-strain response (used in the FE simulations) for the pre- and post-peak behavior.

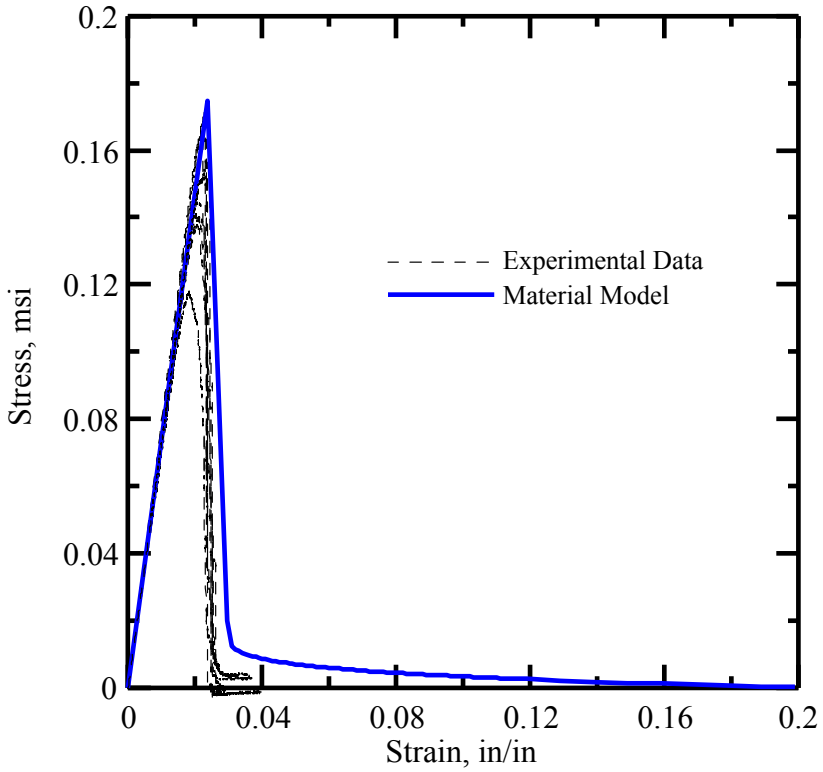

Figure 86. Kevlar 49 Yarn Uniaxial Stress-Strain Results With Approximation for Pre- and Post-Peak Behavior

2.5.3.2.3 Unloading/Reloading and Compression Behavior.

When the fabric is subjected to impact loads, it can load and unload many times throughout the impact event. Therefore, it is important to model cyclic behavior correctly. Cyclic tests were not performed at the yarn level, so the cyclic results obtained from swath tensile tests were used

to model unloading and reloading for yarns as well. Swath tensile test results showed that in the elastic region, the fabric unloads and reloads approximately along the same path but at a rate that is about 1.5 times the elastic stiffness. Therefore, in the material model, the unloading and reloading stiffness were expressed as a factor of 1.5 times the elastic stiffness. Thus, the unloading and reloading stiffness for the yarn (E_{11}^{unl}) was 14.8(10^6) psi. Kevlar 49 yarn has negligible compressive stiffness. However, to avoid numerical instabilities, a very small stiffness was assumed when the FE experiences compression. The compressive stiffness was taken as 0.5% of the elastic stiffness. Thus, the compressive stiffness of the yarn (E_{11}^{comp}) direction was assumed to be 1.6(10^4) psi.

2.5.3.3 Determination of Other Material Properties.

Material properties (with the exception of E_{11}) were approximated based on the Kevlar yarn behavior and data available in literature. Young's modulus was assumed to be 0.5% of E_{11} as the yarn has very low load-carrying capacity in the direction perpendicular to the main longitudinal direction. The shear modulus of the yarn was expected to be low. Cheng, et al. [35], conducted torsional experiments to compute shear modulus of single filament. They found that G_{13} is approximately 24.4 GPa and G_{12} is very small. In this research, the yarn level shear modulus G_{13} and G_{12} was assumed to be 3.48 msi and G_{23} was assumed to be 0.5% of E_{11}. There is no available literature for the Poisson's ratio of Kevlar yarn. In this research, Poisson's ratio was assumed to be zero.

2.5.4 Verification of Micromechanical Model.

2.5.4.1 Single-Yarn Simulations.

The material model developed for the solid element was used to perform single-yarn test simulations using LS-DYNA. The model of the single yarn was built for a 2-in. G.L. The geometrical model was based on the parameters computed during the experimental phase. Figure 87 shows a representative Kevlar yarn model. The mesh configurations used to analyze the model are shown in table 26.

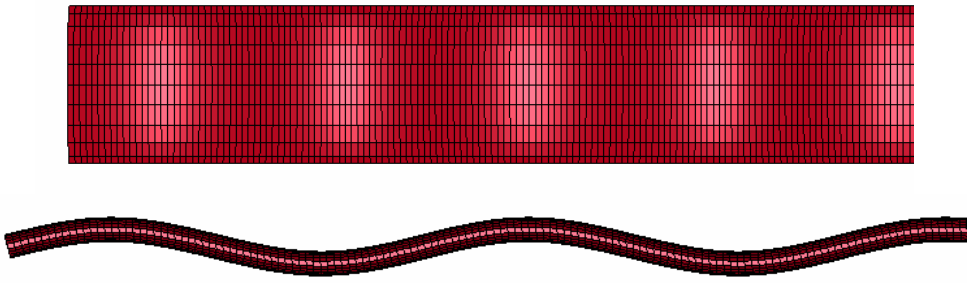

Figure 87. Single-Yarn Model

Table 26. Mesh Study—Single-Yarn Simulations

Mesh No.	Number of Elements		
	Along Length per Sine Curve	Along Width	Along Thickness
1	10	10	1
2	20	10	1
3	20	20	2
4	20	10	3
5	40	20	3
6	40	20	1
7	60	30	1
8	60	10	1

One end of the model was kept fixed and other end was given a velocity to simulate the displacement-controlled test. The stroke rate used in the actual test was such that the strain rate was 0.025 [min^{-1}]; however, if this small rate was used, the simulation would take a very long time, even for small models. To avoid this, a higher velocity was used for performing the runs. The time was further reduced by increasing the time step between cycles by employing mass scaling. Mass scaling is the technique by which the time step between cycles is reduced by artificially increasing the density of the material. It is important to note that although the actual test was at very low strain rates, the simulation was expected to see relatively higher strain rates. Therefore, to simulate static tests with low simulation time and good accuracy, it became necessary to make the model independent of strain rate. This was done by increasing the C and P values.

2.5.4.2 Swath Tensile Test Simulations.

The swath model was built by replicating the unit cell in the fill and warp directions. The simulation of the swath model was performed by applying a fixed boundary condition on one end and velocity on the free end of the fabric. To reduce overall simulation time, mass scaling was used. Table 27 shows different mass scaling used in the swath model, and figure 88 shows the stress-strain curves obtained.

Table 27. Mass Scaling Study—Swath Tensile Test Simulations

Test Case	Velocity (in/ms)	Density	Cycle Time	Simulation Time	Comments
1	0.005 (ramp function used)	-	5.00E-04	31 hr 18 min	Failure throughout the sample and not localized
2	0.5 (ramp function used)	-	5.00E-04	30 min	Unstable simulation
3	0.0005 (ramp function used)	-	5.00E-03	30 hr	Unstable simulation
4	0.001 (ramp function used)	x1E6	2.20E-03	15 hr 40 min	Shear type of failure
5	0.005 (sudden jump in velocity)	x1E6	2.20E-03	23 hr	Localized failure near the loading end
6	0.0005 (sudden jump in velocity)	x1E7	7.20E-03	12 hr	Failure near the fixed end

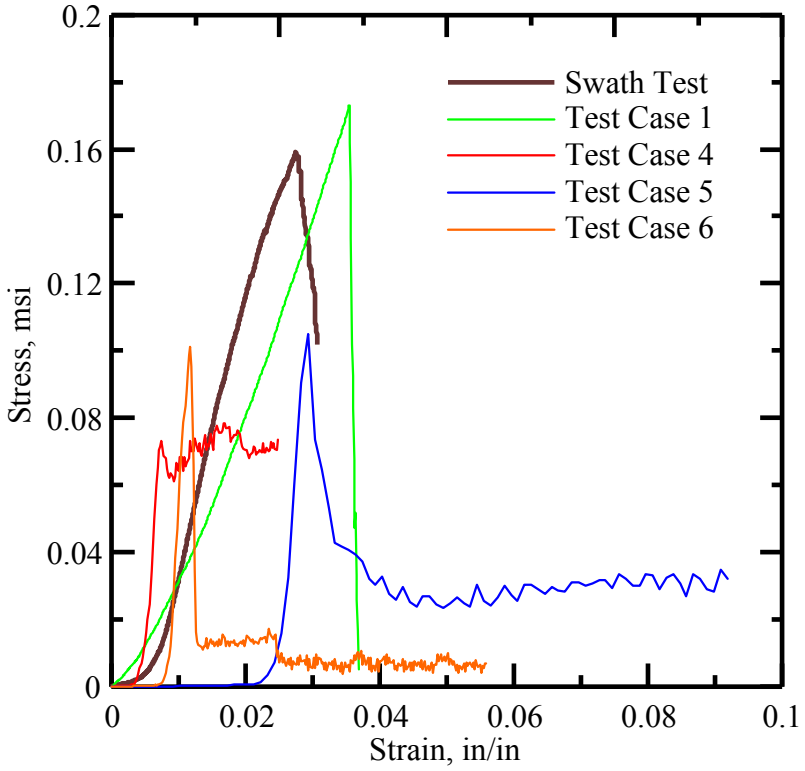

Figure 88. Single-Yarn Simulation Results

3. CONCLUSIONS.

The continuum model previously developed at Arizona State University (ASU) (ASUumatV1.0) was improved by modifying failure criteria (ASUumatV1.1). The material model was validated by comparing the finite element (FE) simulation results with experimental results. Two different modeling configurations were studied. In the first configuration, only one FE layer was used to represent the different number of fabric layers, while in the second methodology one FE layer was used to represent four fabric layers. The overall results matched the experimental tests, except test cases with low velocity and a fewer number of fabric layers.

A detailed study of the experimental data with regard to available videos of experiments conducted at the National Aeronautics and Space Administration Glenn Research Center (NASA-GRC) during Phase I indicated that there were discrepancies in reported projectile orientation for test cases LG424, LG427, LG432, LG434, and LG449. It was found that in Phase I (unlike Phase II) projectile orientations were not computed, and all the projectile hits were assumed to be direct hits.

The simulation results from the two continuum models (ASUumatV1.0 and ASUumatV1.1) showed that both models predicted relatively well; ASUumatV1.1 performed better than ASUumatV1.0 when only Phase II test cases were considered. The average error in energy prediction with ASUumatV1.0 was 7.0% with a standard deviation of 15.4%, while ASUumatV1.1 had an average error of 5.3% with a standard deviation of 11.7% for Phase II test cases. The multilayer models also performed well. The average difference between energy absorption reported during experiment and simulation was 4.9% with a standard deviation of 14.6% for Phase I and II test cases. The multilayer model is able to capture the frictional effect between different fabric layers and can be a helpful tool in predicting the optimum number of fabric layers required for a particular configuration.

To check the numerical instability in the model, a methodology was adopted to trace the variation of different energy values during the simulation. These checks ensured the numerical stability during the simulation.

A methodology to build a micromechanical model of Kevlar® fabric was developed. This methodology is general enough to be used for other fabric materials. The model development started with an approximation of the Kevlar weave geometry using simple geometric shapes like ellipse and sine curves. Optical microscopy was used to take images of sectioned fabric potted in epoxy. A MATLAB® program was developed that could be used to digitize these images and provide an estimate of parameters associated with geometric functions. An experimental procedure to perform single-yarn tensile tests was developed and experiments were performed with gage lengths varying from 2 to 17 inches. The Weibull analysis of this data clearly indicated the effect of gage lengths on the Kevlar yarn properties. Single-yarn tensile tests were used for the estimation of Young's modulus. Other material properties were approximated based on the material geometry, experience, and data available in literature. A constitutive model was developed in FORTRAN based on quasi-static tensile tests of Kevlar yarns, including nonlinearity in the material behavior, strain rate effect, and failure criteria. The developed constitutive model was implemented in the explicit FE code LS-DYNA as a user-defined

material definition. The developed material model was validated by comparing the FE simulation results against results from experimental quasi-static tests.

The developed micromechanical model of Kevlar can be used for virtual testing and can be very helpful in understanding the Kevlar behavior under different loading conditions. The capability of this model to capture yarn-to-yarn interaction makes it very useful in understanding the effect of friction between yarns on behavior of fabric. The simulation results of single-yarn tensile tests and swath tensile tests were verified within the experimental error and FE solid element shortcomings.

4. RECOMMENDATIONS.

While modest progress has been made in improving the predictive capabilities of the Kevlar material model via new experiments and changes to the constitutive model, further improvements are possible, as listed below.

- Picture Frame Shear Tests: The shear modulus behavior is based on results from picture frame shear tests. The shear resistance increases with an increase in shear strain. At low shear strains, the fabric has little resistance to shear deformation. The yarns rotate and the warp and fill directions are no longer orthogonal. At some point, there is a very rapid increase in the shear stress value. This is caused by the re-orientation and packing of the fabric yarns as the shear strain increases. Close examination of the fabric's deformation during the picture frame tests revealed that the fabric was wrinkling at the edges during the initial stages of loading, and it experienced buckling during the final stages of loading. Further testing and examination of the results are necessary to understand and improve the shear behavior predictive capability of the model.

- Biaxial Tests: It has been assumed in this study that the stress-strain relationships are decoupled so that any stress component is a function of only one strain component. In other words, the in-plane behavior of the fabric is not a function of the Poisson's effect. Limited fabric tests have shown that if the fabric is held in the fill direction and a load is applied in the warp direction, stresses develop in the fill direction. More thorough biaxial testing is necessary to gage the Poisson's effect to obtain rational continuum-equivalent values of Poisson's ratio covering the various behavioral zones in a fabric swatch: crimp, pre-peak, post-peak, and ultimately, failure.

- High Strain Rate Tests: Little information is available on the strain rate behavior of Kevlar 49. The strain rate behavior used in the current model is based on published data where strain rates up to 1500/s are considered. Results from FE analysis show that fabrics are subjected to strain rates as high as 20,000/s for very short durations, and 5,000-10,000/s can exist for much longer durations. More testing in both intermediate strain rate regimes (500-1,500/s) and high strain rate regimes (10,000-20,000/s) are necessary to understand how Kevlar fabrics behave under a high rate of loading.

- Ballistic Tests: Of all the ballistic tests considered in this report, in only one test was the projectile contained. Establishing the ballistic limit is necessary to understand how the projectile interacts with the fabric, how the various layers of fabric are damaged during

and after impact, and how much damage was done to the projectile, if any. Furthermore, only one metric was used in the evaluation process—the absorbed energy. By using strategically placed high-speed cameras and the right software, it is possible to also measure the amount of fabric deformation that occurs during the impact. Additional ballistic tests will provide new experimental data to see how well the developed material model can be used as a predictive tool.

5. REFERENCES.

1. Tabiei, A. and Yi, W., "Comparative Study of Predictive Methods for Woven Fabric Composite Elastic Properties," *Journal of Composites and Structures*, Vol. 58, 2002, pp. 149-64.

2. Scida, D., Aboura, Z., Benzeggagh, M.L., and Bocherens, E., "A Micromechanics Model for 3D Elasticity and Failure of Woven-Fibre Composite Materials," *Journal of Composite Science and Technology*, Vol. 59, 1999, pp. 505-17.

3. Peng, X.Q. and Cao, J., "Numerical Determination of Mechanical Elastic Constants of Textile Composites," *15th Annual Technical Conference of the American Society for Composites*, College Station, Texas, 2000.

4. Tabiei, A. and Ivanov, I., "Computational Micro-Mechanical Model of Flexible Woven Fabric for Finite Element Impact Simulation," *7th International LS-DYNA Users Conference*, 2002, pp. 8-15 to 8-40.

5. Roylance, D., Chammas, P., Ting, J., Chi, H., and Scott, B., "Numerical Modeling of Fabric Impact," *Proceedings of the National Meeting of the American Society of Mechanical Engineers (ASME)*, San Fransisco, California, 1995.

6. Xia, Y. and Wang, Y., "The Effects of Strain Rate on the Mechanical Behavior of Kevlar Fibre Bundles: An Experimental and Theoretical Study," *Composite Part A: Applied Science and Manufacturing*, Vol. 29A, 1998, pp. 1411-15.

7. Xia, Y. and Wang, Y., "Experimental and Theoretical Study on the Strain Rate and Temperature Dependence of Mechanical Behavior of Kevlar Fibre," *Composite Part A: Applied Science and Manufacturing*, Vol. 30, 1999, pp. 1251-57.

8. Barbero, E.J., et al., "Finite Element Modeling of Plain Weave Fabrics From Photomicrograph Measurements," *Journal of Composite Structures*, Vol. 73, No. 1, 2006, pp. 41-52.

9. Ishikawa, T. and Chou, T.W., "Stiffness and Strength Behavior of Woven Fabric Composites," *Journal of Composite Materials*, Vol. 17, 1983, pp. 3211-220.

10. Ishikawa, T. and Chou, T.W., "Elastic Behavior of Woven Hybrid Composites," *Journal of Composite Materials*, Vol. 16, 1982, pp. 2-19.

11. Ishikawa, T. and Chou, T.W., "One-Dimensional Micromechanical Analysis of Woven Fabric Composites," *AIAA Journal*, Vol. 21, No. 12, 1983, pp. 1714-21.

12. Ishikawa, T., Matsusima, M., Hayashi, Y., and Chou, T., "Experimental Confirmation of the Theory of Elastic Moduli of Fabric Composites," *Journal of Composite Materials*, Vol. 19, 1985, pp. 443-58.

13. Tabiei, A. and Jiang, Y., "Woven Fabric Composite Material Model With Material Nonlinearity for Nonlinear Finite Element Simulation," *Journal of Solids Structures*, Vol. 36, 1999, pp. 2757-71.

14. Tanov, R. and Tabiei, A., "Computationally Efficient Micro-Mechanical Woven Fabric Constitutive," *Journal of Models Applied Mechanics*, Vol. 68, No. 4, 2001, pp. 553-60.

15. Naik, N.K. and Ganesh, V.K., "Failure Behavior of Plain Weave Fabric Laminates Under On-Axis Uniaxial Tensile Loading: II. Analytical Predictions," *Journal of Composite Materials*, Vol. 30, No. 16, 1996, pp. 1779-1822.

16. Naik, N.K. and Ganesh, V.K., "Failure Behavior of Plain Weave Fabric Laminates Under On-Axis Uniaxial Tensile Loading: I. Laminate Geometry," *Journal of Composite Materials*, Vol. 30, No. 16, 1996, pp. 1748-78.

17. Vandeurzen, Ph., Ivens, J., and Verpoest, I., "A Three-Dimensional Micromechanical Analysis of Woven-Fabric Composites: I. Geometric Analysis," *Journal of Composite Science and Technology*, Vol. 56, 1996, pp. 1303-15.

18. Vandeurzen, Ph., Ivens, J., and Verpoest, I., "A Three-Dimensional Micromechanical Analysis of Woven-Fabric Composites: II. Elastic Analysis," *Journal of Composite Science and Technology*, Vol. 56, 1996, pp. 1317-27.

19. Barbero, E.J., Lonetti, P., and Sikkil, K.K., "Finite Element Continuum Damage Modeling of Plain Weave Reinforced Composites," *Composites Part B: Engineering*, Vol. 37, 2006, pp. 137-47.

20. Srirengan, K., Whitcomb, J., and Chapman, C., "Modal Technique for Three-Dimensional Global/Local Stress Analysis of Plain Weave Composites," *Journal of Composite Structures*, Vol. 39, 1997, pp. 145-56.

21. Kollegal, G.M. and Sridharan, S., "Strength Prediction of Plain Woven Fabrics," *Journal of Composite Materials*, Vol. 34, No. 3, 2000, pp. 240-57.

22. Kollegal, M., Chatterjee, S.N., and Flanagan, G., "Progressive Failure Analysis of Plain Weaves Using Damage Mechanics Based Constitutive Laws," *Journal of Damage Mechanics*, Vol. 10, 2001, pp. 301-23.

23. Barbero, E.J., Lonetti, P., and Sikkil, K.K., "Finite Element Continuum Damage Modeling of Plain Weave Reinforced Composites," *Composites Part B: Engineering*, Vol. 37, 2006, pp. 137-47.

24. Xue, P., Xiongqi, P., and Cao, J., "A Non-Orthogonal Constitutive Model for Characterizing Woven Composites," *Composites Part A: Applied Science and Manufacturing*, Vol. 34, 2003, pp. 183-93.

25. Gu, B., "Analytical Modeling for the Ballistic Perforation of Planar Plain-Woven Fabric Target by Projectile," *Composite Part B: Engineering*, Vol. 34, 2003, pp. 361-71.

26. Shim, V.P.W., Tan, V.B.C., and Tay, T.E., "Modeling Deformation and Damage Characteristics of Woven Fabric Under Small Projectile Impact," *International Journal of Impact Engineering*, Vol. 16, No. 4, 1995, pp. 585-605.

27. Simons, J., Erlich, D., and Shockey, D., "Explicit Finite Element Analysis Modeling of Multilayer Composite Fabric for Gas Turbine Engines Containment Systems, Part 3: Model Development and Simulation of Experiments," FAA report DOT/FAA/AR-04/40, P3, November 2004.

28. Simons, J., Erlich, D., and Shockey, D., "Explicit Finite Element Analysis Modeling of Multilayer Composite Fabric for Gas Turbine Engines Containment Systems, Phase II, Part 3: Material Model Development and Simulation of Experiments," FAA report DOT/FAA/AR-08/37,P3, February 2009.

29. Gomuc, R., "Explicit Finite Element Modeling of Multilayer Composite Fabric for Gas Turbine Engine Containment Systems, Part 4: Model Simulation for Ballistic Tests, Engine Fan Blade-Out and Generic Engine," FAA report DOT/FAA/AR-04/40,P4, November 2004.

30. Vintilescu, I.V., "Explicit Finite Element Analysis Modeling of Multilayer Composite Fabric for Gas Turbine Engines Containment Systems, Phase II, Part 4: Model Simulation for Ballistic Tests, Engine Fan Blade-Out, and Generic Engine," FAA report DOT/FAA/AR-08/37, P4, February 2009.

31. Lim, C.T., Shim, V.P.W., and Ng, Y.H., "Finite-Element Modeling of the Ballistic Impact of Fabric Armor," *International Journal of Impact Engineering*, Vol. 28, 2003, pp. 13-31.

32. Iannucci, L. and Willows, M.L., "An Energy Based Damage Mechanics Approach to Modeling Impact Onto Woven Composite Materials-Part I: Numerical Models," *Composites Part A: Applied Science and Manufacturing*, Vol. 37, No. 11, 2006, pp. 2041-56.

33. Johnson, A.F. and Simon, J., "Modeling Fabric Reinforced Composites Under Impact Loads," *EUROMECH 400: Impact and Damage Tolerance Modeling of Composite Materials and Structures*, Imperial College of Science Technology and Medicine, London, 1999.

34. Krishnan, K., "Using Virtual Testing for Topology Optimization," M.S. Thesis, Department of Civil and Environmental Engineering, Arizona State University, May 2007.

35. Cheng, M., Chen, W., and Weerasooriya, T., "Mechanical Properties of Kevlar KM2 Single Fiber," *Journal of Engineering Materials and Technology*, Vol. 127, No. 2, 2005, pp. 197-203.

36. Rodriquez, J., Shocron, I.S., Martinez, M.A., and Sanchez-Galvez, V., "High Strain Rate Properties of Aramid and Polyethylene Woven Fabric Composites," *Composite Part B: Engineering*, Vol. 27B, 1996, pp. 147-54.

37. Shim, V.P.W., Lim, C.T., and Foo, K.J., "Dynamic Mechanical Properties of Fabric Armour," *International Journal of Impact Engineering*, Vol. 25, 2001, pp. 1-15.

38. Söderberg, A. and Sellgren, U., "Modeling of Strain Hardening and Strain Rate Hardening of Dual Phase Steels in Finite Element Analysis of Energy-Absorbing Components," *National Agency for Finite Element Methods and Standards World Congress*, No. 69, May 2005.

39. Shockey, D.A., Erlich, D.C., and Simons, J.W., "Improved Barriers to Turbine Engine Fragments: Interim Report III," FAA report, DOT/FAA/AR-99/8, III, May 2001.

40. Sharda, J., "Experimental Methods and Numerical Simulation of Fabrics for Engine Containment Systems," M.S. Thesis, Department of Civil Engineering, Arizona State University, 2002.

41. Rajan, S.D., Mobasher, B., Sankaran, S., Naik, D., and Stahlecker, Z., "Explicit Finite Element Analysis Modeling of Multilayer Composite Fabric for Gas Turbine Engine Containment Systems, Phase II, Part 1: Fabric Material Tests and Modeling," FAA report, DOT/FAA/AR-08/37,P1, February 2009.

42. Stahlecker, Z., Mobasher, B., Rajan, S.D., and Pereira, J.M., "Development of Reliable Modeling Methodologies for Engine Fan Blade Out Containment Analysis, Part II: Finite Element Analysis," *International Journal of Impact Engineering*, Vol. 36, 2009, pp. 447-459.

43. Cowper, G.R. and Symonds, P.S., "Strain Hardening and Strain Rate Effect in the Impact Loading of Cantilever Beams," Brown University, Division of Applied Mathematics, September 1957.

44. Revilock, D.M. and Pereira, J.M., "Explicit Finite Element Analysis Modeling of Multilayer Composite Fabric for Gas Turbine Engine Containment Systems, Phase II, Part 2: Ballistic Impact Testing," FAA report DOT/FAA/AR-08/37,P2, February 2009.

45. Revilock, D.M. and Pereira, J.M., "Explicit Finite Element Analysis Modeling of Multilayer Composite Fabric for Gas Turbine Engines Containment Systems, Part 2: Ballistic Impact Testing," FAA report DOT/FAA/AR-04/40,P2, November 2004.

46. LS-DYNA, "Keyword User's Manual: Version 971," Livermore Software Technology Corp., Livermore, California, 2003.

47. Bansal, S., Mobasher, B., Rajan S.D., and Vintilescu, I., "Numerical Modeling of Engine Fan Blade-Out Events," *ASCE Journal of Aerospace Engineering*, Vol. 22, 2009, pp. 249-259.